



Passively modelocked surface-emitting semiconductor lasers

Ursula Keller^{a,*}, Anne C. Tropper^b

^a*ETH Zurich, Institute of Quantum Electronics, Physics Department, Wolfgang-Pauli-Street 16, 8093 Zurich, Switzerland*

^b*University of Southampton, School of Physics and Astronomy, Southampton, SO17 1BJ, UK*

Accepted 26 March 2006

Available online 18 May 2006

editor: G.I. Stegeman

Abstract

This paper will review and discuss pico- and femtosecond pulse generation from passively modelocked vertical-external-cavity surface-emitting semiconductor lasers (VECSELS). We shall discuss the physical principles of ultrashort pulse generation in these lasers, considering in turn the role played by the semiconductor quantum well gain structure, and the saturable absorber. The paper will analyze the fundamental performance limits of these devices, and review the results that have been demonstrated to date. Different types of semiconductor saturable absorber mirror (SESAM) design, and their characteristic dynamics, are described in detail; exploring the ultimate goal of moving to a wafer integration approach, in which the SESAM is integrated into the VECSEL structure with tremendous gain in capability. In particular, the contrast between VECSELS and diode-pumped solid-state lasers and edge-emitting diode lasers will be discussed. Optically pumped VECSELS have led to an improvement by more than two orders of magnitude to date in the average output power achievable from a passively modelocked ultrafast semiconductor laser.

© 2006 Published by Elsevier B.V.

PACS: 42.55.Px

Keywords: Passive modelocking; Semiconductor laser; Saturable absorber; Nonlinear propagation; Nonlinear semiconductor dynamics

Contents

1. Introduction	68
2. Semiconductor materials	71
2.1. InGaAs/GaAs/AlGaAs	72
2.2. GaInAsP/InP	72
2.3. GaInNAs	73
2.4. AlGaAsSb	74
3. VECSEL gain medium	75
3.1. Optically pumped VECSELS	75
3.2. Temperature dependent gain	77
3.3. Thermal Management of optically pumped VECSELS	78
3.4. Thermal management with heat spreader	81
3.5. Electrically pumped VECSELS	83

* Corresponding author.

E-mail address: keller@phys.ethz.ch (U. Keller).

4. Semiconductor saturable absorber	84
4.1. Semiconductor dynamics	84
4.2. Important macroscopic parameters and requirements for self-amplitude modulation (SAM)	85
4.3. SAM obtained with bandfilling and fast carrier trapping	86
4.4. SAM obtained with quantum-confined Stark effect	90
4.5. Quantum-dot saturable absorber	91
4.6. SESAM structure	92
4.7. Thermal management of SESAMs	94
5. Passive modelocking of VECSELS	95
5.1. Dynamic gain saturation	95
5.2. Pulse shaping mechanisms	96
6. Modelocking results	99
6.1. Overview	99
6.2. Modelocking results in the picosecond regime	100
6.2.1. Modelocked VECSELS up to 10 GHz	100
6.2.2. 1:1 Modelocking	105
6.2.3. Modelocked VECSELS at 50 GHz	107
6.3. Modelocking results in the femtosecond regime	109
6.4. Modelocking results with electrically pumped VECSELS	112
7. Conclusion and outlook	114
7.1. Final remarks	114
7.2. Wafer scale integration	114
Acknowledgment	115
References	116

1. Introduction

In the past few years, a novel type of laser has bridged the gap between semiconductor lasers and solid-state lasers. The vertical–external-cavity surface-emitting laser (VECSEL) [1,2] combines the best of both worlds: the semiconductor gain medium allows for flexible choice of emission wavelength via bandgap engineering and offers a wealth of possibilities from the semiconductor processing world. Almost arbitrary optical layer structures can be integrated vertically with the gain section; in particular multi-purpose mirrors, combining functions such as dispersion control, dual wavelength reflection for pump and laser wavelength, antireflection layers etc. One important advantage of optically pumped VECSELS is that they can convert fairly low-cost, low-beam-quality optical pump power from high-power diode laser bars into a near-diffraction-limited output beam with good efficiency in wavelength regions which are not covered by established solid-state laser gain materials. Lateral integration promises high-performance photonic integrated circuits in the near future. The combination of the mature optical pumping technology extensively used for diode-pumped solid-state lasers with efficient heat removal of solid-state thin-disk lasers resulted in performance of VECSELS that surpasses anything possible to date with conventional semiconductor lasers. Continuous-wave output powers of up to 30 W with an M^2 of 3 have been reported from such optically pumped VECSELS [3], and electrically pumped devices have reached 0.5 W single-mode output power [4].

Concerning high-performance passive modelocking, a domain where diode-pumped solid-state lasers using semiconductor saturable absorber mirrors (SESAMs) have been dominant for years [5–8], the VECSEL possesses the advantage of a large gain cross-section which suppresses Q -switching instabilities [9]. VECSELS are therefore ideally suited for high-repetition-rate modelocking in combination with high average output powers. After the first demonstration of a passively modelocked VECSEL in 2000 [10], pulse width and output power have improved continuously to 486-fs pulses at 10 GHz with 30 mW [11] and 4.7-ps pulses at 4 GHz with 2.1 W average output power [12]. The comparison of various high-repetition-rate sources in Fig. 1 shows that optically pumped VECSELS have already pulled even with solid-state lasers in the regime between 1 and 10 GHz.

Novel SESAMs based on quantum dot saturable absorbers (QD-SESAMs) were developed to move towards an even more ambitious goal: the integration of the absorber into the VECSEL gain structure [13]. In a first step passive modelocking with the same mode area in the gain and the absorber had to be demonstrated for the full wafer-scale integration. We refer to this as “1:1 modelocking” which was successfully demonstrated using these new QD-SESAMs and therefore the viability of the integrated-absorber VECSEL concept has been demonstrated [13]. This could pave the

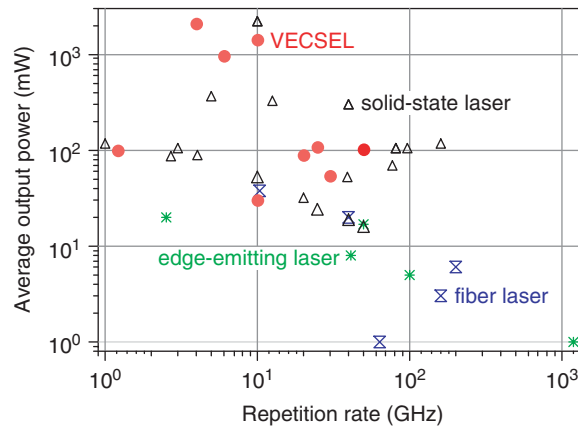


Fig. 1. Average power and pulse repetition rate achieved to date by high repetition rate sources.

way for the development of compact and rugged high-repetition-rate pulsed laser sources in the > 100 -mW power class which can be cheaply fabricated by wafer-scale mass production and therefore fill a gap in the performance spectrum of current laser technology. These novel QD-SESAMs also supported the scaling of pulse repetition rates to 50 GHz with 100 mW of average power [14].

The ultimate goal is to extend the excellent results with optically pumped VECSELs to electrical pumping. However, this is not a simple extension, even though very promising results have been achieved in the cw regime, with 500 mW average output power demonstrated in a near-diffraction-limited beam [4]. Initial modelocking results reported however only very moderate average output power well below 100 mW [15].

From an application point of view, telecom transmission systems at 10 Gb/s and higher mostly use return-to-zero (RZ) formats [16] and soliton dispersion management techniques [17], both of which rely on clean optical pulses. The much higher contrast ratio of directly pulsed lasers (compared to externally modulated continuous-wave sources) improves overall system signal-to-noise and allows further scaling to higher repetition rates through optical time-division multiplexing (OTDM). Apart from the transmitter side, there are also other important applications of pulsed lasers in the receivers of transmission systems, e.g. optical switching for demultiplexing and clock recovery [18]. Research in optical clocking and interconnects [19,20] quantum cryptography, high-speed electro-optic sampling [21,22], frequency metrology [23,24], or generation of polarized electron beams for particle accelerators [25] has proved the need and the applicability of clean and stable high repetition-rate optical pulses in a variety of different fields. Although the span of possible applications is very broad, the requirements on an ideal pulse source are similar in each field and can be summarized as follows: The emitted pulse train has to consist of femto- or picosecond optical pulses with high contrast ratio, high pulse energy and low timing jitter. Additionally, wavelength tunability or setability in the regime of interest should be feasible. The instrument itself needs to be affordable, reliable, compact and robust.

Multi-gigahertz pulse sources to date have almost always involved either an edge-emitting semiconductor laser [26], which is usually actively or hybrid modelocked, or a harmonically modelocked fiber ring laser [27]. Edge-emitting semiconductor lasers can appear to be attractive due to their very compact optical setup, but expensive electronics are required for active modelocking, the structures required for a semiconductor laser with this performance are complicated and difficult to produce, and their average power levels are relatively low. Additionally, there is little of the expected cost saving from semiconductor manufacturing, due to low yield/relatively low production volumes, and the dominant packaging/testing costs. Multi-gigahertz fiber lasers can also generate high-quality pulses, but they have very long and complex laser cavities, requiring sophisticated means to obtain stable “harmonic” modelocking—which consists of a large number of precisely equidistant pulses in the cavity. Additionally, individual pulses generated by harmonic modelocking do not necessarily exhibit a fixed phase relation. This excludes promising and important coding formats such as return-to-zero differential phase shift keying [28,29] which carry the data in the phase of the pulses, rather than in the amplitude.

Up to a few years ago, the repetition rate of passively modelocked solid-state lasers was limited to a few gigahertz. Q -switching instabilities impaired performance at the highest pulse repetition rates [9]. In recent years, the

Table 1
Passively modelocked diode-pumped solid-state lasers: high-repetition rate results (i.e. > 1 GHz)

Gain	ML	λ_0	τ_p	P_{av} (mW)	f_{rep} (GHz)	Ref.
Cr:LiSAF	SESAM	857 nm	146 fs	3	1	[46]
Cr:YAG	KLM	1.54 μm	115 fs	150	2.64	[47]
		1.52 μm	68 fs	138	2.33	[48]
		1.52 μm	200 fs	82	0.9, 1.8, 2.7	[37]
Nd:YLF	SESAM	1.52 μm	75 fs	280	1	[49]
		1.34 μm	21 ps	127	1.4	[43]
Nd:YVO ₄	SESAM	1.064 μm	8.3 ps	198	13	[31]
			6.8 ps	81	29	[50]
			4.8 ps	80	39, 49, 59	[51]
			2.7 ps	288	40	[52]
			2.7 ps	65	77	[32]
			2.7 ps	45	157	[33]
			13.7 ps	2.1	10	[34]
			7 ps	45	5	[44]
			7.3 ps	40	10	
			18.9 ps	3.46	0.37–3.4	[53]
Nd:GdVO ₄	SESAM	1.064 μm	12 ps	500	9.66	[54]
			4.4 ps	~60	2.5–2.7	[54]
			3.8 ps	12	10	[55]
Er:Yb:glass	SESAM	full C-band	1.9 ps	25	25	[41]
			4.3 ps	18	40	[56]
			1.7–1.9 ps	> 20	8.8–13.3	[57]
			2 ps	7.5	50	[42]
			3.2 ps	10	77	[237]

ML modelocking techniques. λ_0 : center lasing wavelength. τ_p : measured pulse duration. P_{av} : average output power. f_{rep} : pulse repetition rate.

consequent exploitation of the flexibility of semiconductor saturable absorber mirrors (SESAMs) [5,7,30] allowed the Keller group to develop passively modelocked lasers with multi-GHz pulse repetition rates, very good pulse quality, comparatively high output powers, and wavelength tunability in the areas of interest (for example the ITU-specified C-band from approximately 1525 to 1565 nm) (Table 1). Passive modelocking means that the pulses are achieved without using any expensive multi-gigahertz electronics. In addition, the pulses originate from fundamental modelocking. Thus, every output pulse is a copy of the same single pulse, which travels back and forth in the cavity. Therefore, pulse-to-pulse variations are minimized and the phase of the pulses is constant. For the first time, pulse repetition rates above 10 GHz from passively modelocked ion-doped solid-state lasers have been generated with Nd:YVO₄ lasers at a center wavelength around 1 μm [31]. This laser has a large gain cross section and therefore Q -switching instabilities are more strongly suppressed. Shortly afterwards the frontier was pushed up to 77 GHz [32] and 160 GHz [33] (Fig. 1). The average power has been optimized at a 10 GHz pulse repetition rate to as high as 2.1 W [34]. The peak power was sufficient for efficient nonlinear frequency conversion. For example, a synchronously pumped optical parametric oscillator (OPO) was demonstrated producing picosecond pulses broadly tunable around 1.55 μm with up to 350 mW average output power [34,35]. Such all-solid-state synch-pumped OPOs can reach the S-, C- and L-bands in telecommunications. With an additional Yb-doped fiber amplifier, the repetition rate was pushed up to 80 GHz [36]. In the telecom wavelength ranges (around 1.3 and 1.55 μm), where only few solid-state gain media are available, it was not initially possible to demonstrate multi-GHz pulse repetition rates [37,38]. However with improved SESAM designs [30], and a deeper understanding of the Q -switching instabilities [39,40], full C-band tuning [41] and pulse repetition rates up to 50 GHz [42] have been demonstrated with a diode-pumped Er:Yb:glass laser (Fig. 1). At 1.3 μm both Nd:YLF [43] and Nd:YVO₄ [44] have been passively modelocked at GHz repetition rates. In addition, the timing jitter of diode-pumped solid-state lasers is very close to the quantum noise limit [45]. Compared to the ultrafast solid-state lasers, VECSELs offer the prospect of even more compact high-power sources, in which the SESAM is integrated into the VECSEL gain chip, and the structure is pumped electrically. Both of these innovations, however, are yet to be demonstrated.

For comparison, it is also instructive to consider briefly the performance of pulsed edge-emitting semiconductor diode lasers, which can exhibit the highest pulse repetition rates of any optical source. The obvious advantages of compactness, efficiency of pumping, and ease of manufacture and integration make these sources primary candidates for applications such as optical time-domain multiplexing, microwave carrier generation and optical clock recovery. The efficiency of direct modulation of the diode current falls off exponentially with increasing frequency above the diode relaxation resonance, which lies typically in the range 1–10 GHz: thus the highest repetition frequencies are achieved using modelocking of monolithic diode lasers, with gain, saturable absorption and/or external modulation all built into a single chip. The various schemes developed to realise lasers of this type have been reviewed by Avrutin et al. [58]. Passive modelocking, with a reverse-biased saturable absorber section included in the monolithic cavity, is particularly well-adapted to the generation of ultrashort pulses at high repetition rate because it does not require electrical modulation, which imposes a bandwidth limitation on repetition rate, and also impresses phase structure on the pulses. The first demonstration of such a monolithic device was reported by Vasil'ev et al. [59], who reported a 100-GHz train of 2.5-ps pulses from an AlGaAs/GaAs injection laser, corresponding to fundamental modelocking of the 380- μm long cavity. Repetition frequencies higher than ~ 250 GHz have not been reported using fundamental modelocking; the short gain section imposes severe power limitations on the device, which also becomes challenging to fabricate. Higher frequencies are achieved by harmonic modelocking of either the colliding pulse [60] or the compound-cavity [61] type. Yanson et al. [62] have reported modelocking of 860-nm AlGaAs/GaAs double quantum well ridge waveguide laser diodes at pulse repetition frequencies up to 2.1 THz, corresponding to the 33rd harmonic of the round-trip frequency. The modelocking performance of these devices relied critically on accurate control of the sub-cavity length ratios, which were lithographically defined. The pulses were near sinusoidal, and the devices emitted up to 2.2 mW per facet in cw operation. For applications that require the shortest possible pulses it is generally more practical to compress chirped picosecond pulses externally than to generate femtosecond pulses directly from a modelocked diode source. Tamura et al. [63] were able to generate a 50-GHz train of 280-fs pulses at a wavelength of 1557 nm with average power more than 100 mW by combining a modelocked diode with an external all-fiber amplifier and pulse compressor; their modelocked edge-emitter had an average power of 17 mW. Scollo et al. [64] have reported the generation of 600 fs pulses directly from a 42-GHz modelocked diode, albeit accompanied by numerous satellite pulses; these authors make use of a novel saturable absorber design [65] with estimated sub-picosecond recovery time. A two-section quantum dot diode laser produced strongly chirped 2-ps pulses with 45 mW average power and 400-fs pulses with 25 mW at 21 GHz pulse repetition rates [66]. Modelocked edge-emitting diodes are thus immensely versatile in repetition frequency, from individual gain-switched pulses, through the microwave region of the spectrum and up to THz. Their power scalability, however, is limited, with about 10 mW appearing currently to be about the practical limit; and they typically emit self-phase-modulated pulses of picosecond duration that can be externally compressed to the femtosecond regime if the pulse has a suitable phase structure.

This paper will review and discuss pico- and femtosecond pulse generation from passively modelocked VECSELs both optically and electronically pumped. After surveying the different semiconductor material systems in Section 2, we continue with a brief description of the VECSEL gain medium in Section 3, followed by a review of the different semiconductor saturable absorber nonlinearities that can be integrated into a SESAM structure in Section 4. The basic physical principles of passive modelocking of VECSELs will be discussed in Section 5, and the results achieved to date in Section 6. We shall conclude with an outlook towards wafer scale integration in Section 7.

2. Semiconductor materials

Semiconductor materials offer a wide flexibility in choosing the laser emission wavelength, which can range from ~ 400 nm in the UV using GaN-based material, to ~ 2.5 μm in the mid-infrared using GaInAsSb-based materials. More standard high-performance semiconductor material systems which can be grown today cover the infrared wavelength range from 800 nm up to 1.5 μm . Semiconductor compounds used for these wavelengths are AlGaAs (800 to 870 nm), InGaAs (870 to about 1150 nm), GaInNAs (1.1 to 1.5 μm), or InGaAsP (1.5- μm range). A larger wavelength range for a given material composition may only be obtained at the expense of increased defect concentrations because of increased lattice mismatch to a given substrate material. This however can be optimized for saturable absorber applications (discussed in more details in Section 4).

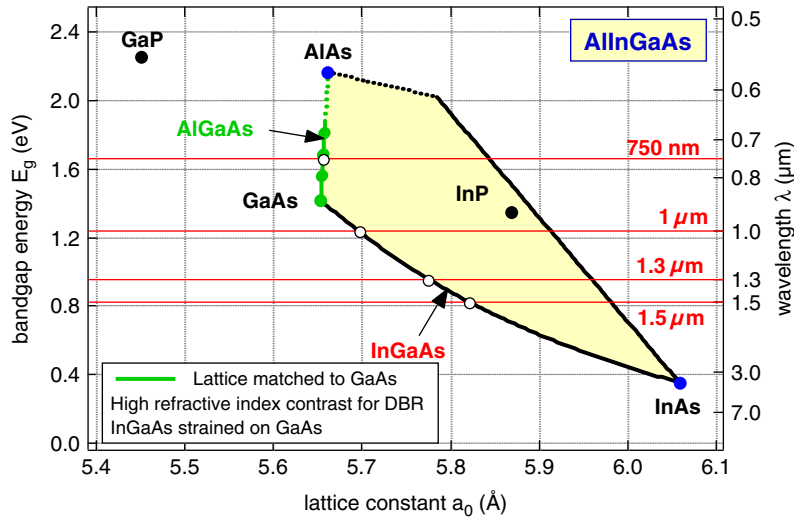


Fig. 2. Bandgap versus lattice constant for the GaAs–AlAs–InAs system.

2.1. InGaAs/GaAs/AlGaAs

The InGaAs/GaAs/AlGaAs semiconductor material system, with properties summarised in Fig. 2, offers the materials that are best suited to the 800 nm–1.1 μm wavelength range because of the near-perfect lattice match between GaAs and AlGaAs. With the inclusion of phosphorus, as Fig. 2 indicates, the bandgap opens up into the visible, allowing the fabrication of red diode lasers. A red VECSEL has recently been reported for the first time [67]. InGaAs layers can be grown on GaAs substrates with a small compressive strain, that enhances the quantum well gain, and shifts the bandgap to the 1- μm region. This system has been used successfully for diode lasers and SESAMs for many years. However, at an operation wavelength of $\sim 1 \mu\text{m}$, InGaAs saturable absorber layers that exceeded the critical thickness had surface striations that introduced too much scattering loss to be used inside a laser [68]. Low temperature MBE growth (see more details in Section 4.3) resulted in strain-relaxed structures, with surfaces that were optically flat, but with strongly increased defect densities. For SESAM applications this is actually advantageous, and has been exploited to optimize the fast dynamic response of the SESAM. For VECSEL gain structures, strain-compensating GaAsP layers are required for reliable high power operation. This strain compensated InGaAs/GaAsP on GaAs material system has been used for almost all the high power and modelocked VECSEL results reported to date (Table 2).

InGaAs saturable absorbers have been grown on AlAs/GaAs Bragg mirrors even at an operation wavelength of 1.3- μm [69,70] and 1.55- μm [41,42,55,56,71,72]. However, these highly strained layers with high indium content exceed the critical thickness, and show significant nonsaturable losses due to strain and defect formation. Optimized low-temperature MBE growth, however, allowed improved InGaAs SESAMs to support stable modelocking in diode-pumped solid-state lasers [41,42,55,56] and VECSELs [73].

2.2. GaInAsP/InP

SESAMs and VECSELs at 1.3 and 1.55 μm wavelengths that are based on the GaInAsP/InP material system (Fig. 3) suffer from low refractive index contrast and poor temperature characteristics. Due to the low refractive index contrast, a high number of InP/GaInAsP mirror pairs are required to form distributed Bragg reflectors (DBRs). This demands very precise control of the growth to achieve DBRs with uniform and accurate layer thickness. The presence of a large number of DBR layers also introduces a high resistance to electrically pumped devices and increases the effective cavity length resulting in slower dynamics. The reflectivity of a thinner DBR may be augmented using a layer of gold [73]. An alternative to lattice-matched DBRs is wafer fusion where high refractive index contrast GaAs/AlAs DBRs are fused to the GaInAsP active layers. The properties of the various material compositions that have been developed to make monolithic InP-based VCSELs are summarised in [74]. Optically pumped [75] and electrically pumped [76]

Table 2
Overview of cw optically pumped VECSEL (OP-VECSEL) performance

Gain	λ_0	λ_p (nm)	P_{max}	Ref.
10 InGa _N /Ga _N QWs	391 nm	335	—	[107]
20 InGaP/AlGaInP/GaAs QWs	668–678 nm	532	390 mW	[67]
15 GaAs/AlGaAs/GaAs QWs	830–860 nm	660	523 mW	[98]
15 GaAs/AlGaAs/GaAs QWs	850 nm	808	135 mW	[108]
14 InGaAs/GaAsP/GaAs QWs	1004 nm	808	690 mW	[1]
6 InGaAs/GaAsP/GaAs QWs	1030 nm	830	> 400 mW	[109]
15 AlGaAs/InGaAs/GaAsP QWs	980 nm	814	1.5 W	[110]
15 AlGaAs/InGaAs/GaAsP QWs	980 nm	810	> 2.5 W	[111]
5 InGaAs/GaAs QWs	950 nm	808	2.2 W	[99]
18 InGaAs/GaAsP QWs	984 nm	808	4.05 W	[112]
7 InGaAs/GaAsP QWs	960 nm	808	4.4 W	Fig. 22
InGaAs/GaAsP/AlGaAs QWs	989 nm	810	8 W	[100]
InGaAs QWs	980 nm	830	30 W	[3]
10 GaInNAs/GaAs QWs	1320 nm	810	612 mW	[79]
5 GaInNAs/GaAs QWs	1285 nm	808	200 mW	[81]
	1314 nm	808	160 mW	[81]
8 InGaAs/InGaAsP/InP QWs	1550 nm	975	80 μ W	[75]
6 InGaAsP/InGaAsP/InP QWs	1550 nm	975	4 mW	[113]
6 InGaAsP/InGaAsP/InP QWs	1550 nm	980	45 mW	[114]
20 InGaAsP/InGaAsP/InP QWs	1549 nm	1250	470 mW	[115]
20 InGaAsP/InGaAsP/InP QWs	1538–1545 nm	1250	780 mW	[116]
20 InGaAsP/InGaAsP/InP QWs	1555 nm	1250	680 mW	[117]
5 GaInAsSb/AlGaAsSb/GaSb QWs	2.1 μ m	830	—	[118]
5 GaInAsSb/AlGaAsSb/GaSb QWs	2.3 μ m	830	8.5 mW	[119]
5 GaInAsSb/AlGaAsSb/GaSb QWs	2.36 μ m	830	5 mW	[97]

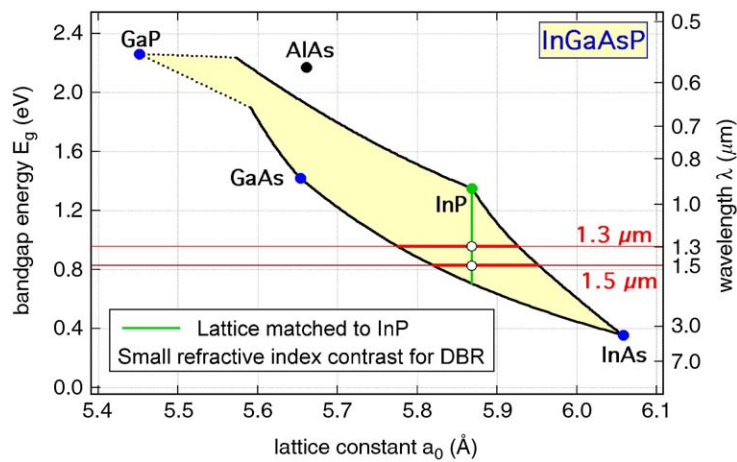


Fig. 3. Bandgap versus lattice constant for the InP–InAs–GaAs system.

VECSEL devices at 1.5 μ m were only recently reported with InGaAsP active layers and maximum output powers of a few mW. Such an optically pumped VECSEL has recently been modelocked for the first time [73].

2.3. GaInNAs

Recently, a family of GaAs-based nitride materials (Fig. 4) has attracted strong attention for laser devices in the telecommunication wavelength range between 1.3 and 1.55 μ m that can use high contrast GaAs/AlGaAs DBR mirrors [77,78]. Adding a few percent of nitrogen to InGaAs has two advantages: a redshift of the absorption wavelength and

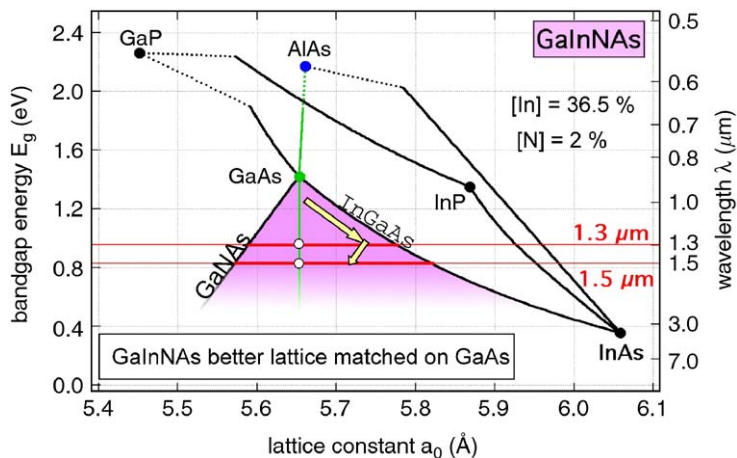


Fig. 4. Bandgap versus lattice constant for the GaInNAs system.

a reduction of the lattice mismatch to GaAs. The drawback is that the nitrogen incorporation decreases the crystalline quality, which is a big challenge for the fabrication of active devices. However, SESAMs are passive devices relying on fast defect-induced nonradiative carrier recombination to allow for short pulse generation.

Many groups have reported GaInNAs vertical cavity surface emitting lasers (VCSELs)—that is not with an external cavity—at 1.3 μm with output powers of more than 1 mW cw at room temperature. In 2004, the first group demonstrated the successful fabrication of a GaInNAs VECSEL at 1.3 μm with 0.6 W output power [79]. Later this year, they made a microchip laser out of it by bonding it to a diamond and obtained 128 mW maximum output power in cw mode [80]. Recently, an optically pumped GaInNAs VECSEL at around 1.3 μm has been passively modelocked with a GaInNAs SESAM [81]. So far, there is no electrical version of a GaInNAs VECSEL demonstrated yet.

GaInNAs material emitting around 1.5 μm is more challenging because of the higher number of nonradiative defects introduced by the increased nitrogen concentration to match the desired wavelength. So far, no VCSEL or VECSEL was demonstrated with this quaternary compound. However, to overcome this limitation, antimony was introduced to GaInNAs which allows for both an increase in the emitting wavelength at lower nitrogen concentrations and a better surface morphology of the QW. The first GaInNAsSb VCSEL was demonstrated by Wistey et al. [82] at 1.46 μm with 0.77 mW output power and a threshold current of 4600 A/cm². No VECSEL version has been demonstrated so far.

More recently GaInNAs SESAMs centered at 1.3 μm have been demonstrated for solid-state laser modelocking at high repetition rates. The first GaInNAs SESAM was reported to modelock a quasi-cw pumped Nd:YLF and Nd:YALO laser at 1.3 μm [83]. Self-starting stable passive cw modelocking of a solid-state laser with a GaInNAs SESAM was demonstrated more recently [84]. A detailed study of the absorber properties and the modelocking behavior revealed that GaInNAs SESAMs provide low saturation fluences and possess extremely low losses [84–86]. These SESAMs supported modelocking at repetition rates of 5 and 10 GHz [87].

In 2003, GaInNAs SESAMs at 1.5 μm were shown to modelock Er-doped fiber lasers [88]. Härkönen et al. [89] reported that fast recovery times of 30 ps can only be obtained by post-growth ion implantation. According to their experiments, modelocking of 1.5- μm solid-state lasers was not possible due to the high nonsaturable losses. Just recently for the first time successful modelocking of solid-state lasers at 1.54 μm using a better GaInNAs SESAM has been demonstrated [90].

2.4. AlGaAsSb

Another interesting long-wavelength semiconductor saturable absorber material is based on the element antimony. The quaternary alloy AlGaAsSb has a wide band gap tunability (1.55 to 0.54 μm) and intrinsically low modulation depth [91,92]. Similar to InGaAsP, AlGaAsSb is lattice-matched to InP, but its absorption edge is not as steep as that of InGaAsP [93]. Therefore, operating the absorber in the bandtail results in a sufficiently small modulation depth (i.e. usually below 0.5%) suitable for high repetition rate lasers. An Sb-based SESAM can be grown by MOVPE with

AlGaAsSb/InP DBRs [94]. Compared to InGaAsP, AlGaAsSb forms a high refractive index contrast with InP (0.4) allowing for a lower number of Bragg periods. The first antimonide SESAM self-started and modelocked a 61-MHz Er:Yb:glass laser [95]. More recently, this was extended to an Er:Yb:glass laser at 10 GHz, 1535 nm and with 4.7 ps pulse duration [96]. A single-frequency tunable Sb-based VCSEL has been demonstrated recently [97].

3. VECSEL gain medium

3.1. Optically pumped VECSELS

The layer structure of a generic VECSEL gain chip is shown schematically in Fig. 5, which depicts two commonly used geometries for an optically-pumped active mirror. In Fig 5(a) a Bragg mirror, of typically 25–30 periods, is grown next to the substrate. The active region consists of a few half-wavelengths thickness of a material which combines the functions of pump absorber, optical spacer, and quantum well barrier. Quantum wells are embedded in the active region, singly or in pairs, at $\lambda/2$ intervals so as to line up with the antinodes of the optical standing wave at the design wavelength. The layer structure terminates in a wide-bandgap window layer that keeps carriers away from the air surface, and controls the optical thickness of the active region, and thus also the effective gain spectrum of the structure. A thin (10-nm) aluminium-free capping layer protects the structure from oxidation. The gain chip depicted in Fig. 5(a) is capillary-bonded to a heat-spreading window, ideally a few-hundred micron thick platelet of silicon carbide or single-crystal diamond, which allows the heat generated in the excitation region to diffuse into a large volume [67,98]. In this geometry the substrate is left intact, and this also spreads heat away from the active region, but to a lesser extent because of the large thermal impedance of the intervening DBR. Thermal management of VECSEL gain chips will be discussed in detail in Sections 3.3–3.4.

The structure shown in Fig. 5(b) achieves low thermal impedance without resorting to an intracavity heat spreading window structure, although at the cost of more complex wafer processing. The elements are grown in reverse order relative to the structure of Fig. 5(a), with the window layer adjacent to the substrate, and the Bragg mirror uppermost. Once the Bragg mirror has been soldered to a heat sink, the substrate can be removed using a combination of mechanical polishing and jet etching, a process that has been described in detail by several authors [2,99]. This bottom-emitting device thus includes within the laser cavity the etched surface created by removal of the substrate. This processing scheme has been used to achieve the highest cw VECSEL output powers reported to date [3,100] and Fig. 22.

The principles underlying the design of semiconductor quantum wells for efficient edge- and surface-emitting lasers have been extensively reviewed, and we refer the reader to the excellent texts that are available e.g. [101–103]. Section 2 surveys the materials systems in which VECSEL gain structures and SESAMs have been realised to date.

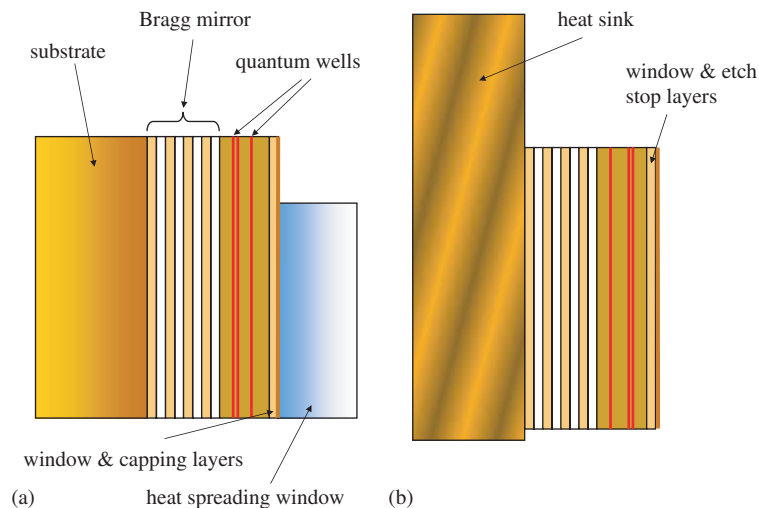


Fig. 5. Schematic VECSEL gain chip layer structures, for use: (a) with heatspreader; and (b) in a bottom-emitting geometry.

The intrinsic gain spectrum of a single quantum well close to transparency is about 20 nm broad, potentially offering a substantial bandwidth for the generation of ultrashort pulses. When embedded in a surface-emitting structure, however, the effective gain spectrum of the wells is proportional to, and strongly modulated by, the longitudinal confinement factor, Γ_z , which peaks at resonances of the subcavity formed between the Bragg mirror and the air surface, and rolls off as the field antinodes shift away from the quantum well positions at wavelengths either side of the design value [104]. The spectrum of Γ_z may be calculated from the relationship

$$\Gamma_z = \frac{\sum_q |E(z_q)|^2}{|E_0|^2}, \quad (3.1)$$

where the summation is over quantum wells, and $|E(z_q)|^2$ is the squared modulus of the E -field amplitude at the position of the q th well, normalised to the total field in the air layer, and calculated using standard multilayer matrix techniques. For ultrashort pulse generation it is therefore essential to design the layers so as to ensure that the spectrum of Γ_z is as smooth and broad as possible [105]. If the layer structure is designed to be near-antiresonant at the operating wavelength, it has been shown that the effective bandwidth of the gain chip can be larger than the intrinsic bandwidth of the quantum well [106].

An overview of cw OP-VECSEL performance at different wavelengths appears in Table 2, which shows the greatest power reported to date using the various semiconductor alloy systems described in Section 2. The values of P_{\max} listed in Table 2 were typically achieved with the VECSEL gain chip cooled below room temperature to $\sim 0^\circ\text{C}$. The shortest-wavelength VECSEL recorded so far is a violet GaN-on-sapphire microchip laser pumped with the frequency-tripled pulsed output from a Nd:YAG laser.

GaAs forms the substrate material for lattice-matched gain structures at 670 nm, 850 nm, 1 μm and 1.3 μm ; all of these can take advantage of high-reflectivity AlGaAs DBR mirrors, and output powers of ~ 0.4 W or higher have been demonstrated at all four wavelengths. The red GaAs system described by Hastie et al. [98] used a gain structure with 20 compressively strained $\text{In}_{0.54}\text{Ga}_{0.46}\text{P}$ quantum wells, grouped in pairs, between $(\text{Al}_{0.6}\text{Ga}_{0.4})_{0.51}\text{In}_{0.49}\text{P}$ barriers. No strain compensation was used. To avoid absorption losses at the laser wavelength in the AlGaAs/AlAs DBR mirror it was necessary to incorporate 45% Al in the high-index layers, and compensate for the loss in index contrast by using 40 repeats. With a birefringent filter in the cavity it was possible to tune the laser wavelength over a 10-nm range. This laser has recently been configured in a microchip geometry as a 3×1 array, emitting ~ 100 mW from each element [120].

There has been relatively little investigation of 850-nm GaAs/AlGaAs VECSELs, although for some applications these devices could offer an inexpensive substitute for a Ti:sapphire laser. Early reports of tunable single-frequency operation [121] and active modelocking [122] made use of this system. Barrier pumping of this system requires red pump diodes at 670 nm, which offer limited power, and are relatively expensive. An alternative approach is in-well pumping at 808 nm, investigated by Schmid et al. [108], who were able to demonstrate 135 mW of output power. This technique not only allows the use of powerful infrared pump diodes; it also greatly reduces the thermal load on the active region, with a pump quantum defect of only 76 meV, as compared to 392 meV. In-well pumping is therefore of interest for power scaling; however the relatively low absorption per well requires some form of pump multi-passing in order to operate efficiently. Schmid et al. measured a slope efficiency of 18.2% with respect to absorbed power for their in-well-pumped laser: their laser had no pump recycling, and the efficiency was only $\sim 1\%$ with respect to incident pump power. Pump recycling might be done externally, as in the high-power thin disc dielectric laser concept introduced by Giesen [123], or in an integrated way, by growing a resonant cavity for pump radiation around the active region. Such a device would be capable of high performance provided that tight tolerances on the layer growth were met.

With the benefit of high-gain compressively-strained InGaAs/GaAs quantum wells, and high-contrast GaAs/AlAs DBR mirrors, the 1- μm GaAs system has allowed extensive exploration of VECSEL potentialities ever since the ground-breaking work by Kuznetsov et al. [1]. As Table 2 shows, investigation of VECSEL power scaling properties has mainly concentrated on this system, as has work on passive modelocking, and on electrical pumping. The high powers recorded in Table 2, up to the record 30 W achieved by Chilla et al. [3], mostly depend on precise growth and thermal management by substrate removal as described in Section 3.3. An exception is the 2.5-W result of Hastie et al. [111], which uses a capillary-bonded SiC heat spreading window with no other processing of the wafer. The demonstration of 0.4-W from an unprocessed wafer by Garnache et al. [124], which used only 1.3 W of pump power,

was achieved even without the aid of a heat-spreading window through careful design of the spectral characteristic of the longitudinal confinement factor, with the active region forming an anti-resonant sub-cavity of the laser. The Bragg mirror in this (MBE)-grown device was designed to have significant reflectivity also at the pump wavelength; this pump recycling contributed to the high optical/optical slope efficiency of $> 40\%$. The 4-W device reported by Fan et al. [112] uses a gain chip designed so as to reduce thermal sensitivity; it incorporates a resonant sub-cavity, but with wells distributed in pairs in such a way as to flatten the longitudinal confinement spectrum.

The difficulty of fabricating highly reflecting DBR mirrors with low absorption and scattering loss in the InP-based material system has been touched on in Section 2. The earliest report of a 1.5- μm VECSEL used a 40-repeat InAlAs/AlGaInAs DBR, lattice-matched to InP, with an active region containing eight unstrained InGaAs/InGaAsP quantum wells. The 1.2- μm bandgap of the lattice matched barriers was designed for efficient absorption of the 975-nm pump radiation. The device was cooled partly by conduction through the DBR, and partly by heat spreading in the thick (2λ) InP window layer; nevertheless the thermal impedance was estimated theoretically and experimentally to be as high as 1500 KW^{-1} . Cw lasing was observed at substrate temperatures up to 7°C [75]. More recently, Symonds et al. reported a 45-mW 1.55- μm VECSEL, in which the use of a SiN/SiAu mirror reduced the thermal resistance to $\sim 87 \text{ KW}^{-1}$ [114]. Lindberg et al. have used the diamond heatspreader technique in conjunction with long wavelength pumping to achieve the highest powers reported to date from a 1.5- μm semiconductor laser. These authors use an active region containing five groups of four InGaAsP quantum wells strain-balanced by InGaAsP barriers with a band-gap wavelength of 1.32 μm . The devices are pumped into the barriers using a 1250-nm fiber Raman laser. A diamond heatspreader was used to bypass the thermal impedance of the 48-period InGaAsP/InP DBR, as discussed in Section 3.4: this group has reported a maximum output power of 780 mW at -30°C for an absorbed pump power of 5.5 W, with, however, a very broad spectral characteristic [116]. Using a thinner heatspreader, an output power of 680 mW was achieved with an improved spectral characteristic [117]. These authors have also taken advantage of the intracavity filtering effect of the heatspreader to demonstrate high power single frequency operation [125].

The development of GaSb-based lasers in the 2–2.5- μm region is of interest for gas spectroscopy and environmental monitoring, since in this water vapour absorption window some key species (CH_4 , CO_2 , HF ...) have strong absorption lines. The first reported VECSEL in this region used 5 compressively-strained 10-nm thick GaInAsSb type-I quantum wells separated by 30-nm thick AlGaAsSb barriers. In this structure, both electron and hole are strongly confined, with confinement potentials of around 290 and 160 meV respectively, contributing to relatively low temperature sensitivity of the gain region. The sample was, however, pumped in the barriers (1.05- μm bandgap) at the relatively short wavelength of 830 nm; thus the thermal load was high, and the VECSEL operated only in quasi-cw mode [118]. This design was later improved with the inclusion of an integrated heatspreader; a 2λ thick AlAsSb layer grown as a window over the active region. With this refinement, the device emitted 8.5 mW in cw operation at 288 K [119]. These authors also report a 5-mW single frequency device that was continuously tunable over a 50-GHz range [97].

3.2. Temperature dependent gain

Unlike a diode-pumped laser with an impurity-doped dielectric gain medium, a quantum well VECSEL suffers from strong temperature sensitivity of the gain medium. In an unsaturated 4-level dielectric laser gain medium the population inversion increase with pumping rate is near-linear, and neither the transition cross-section nor the upper level lifetime is likely to depend strongly on temperature. In a quantum well laser, the gain rises sub-linearly with carrier population; the carrier lifetime itself falls with increasing population; and the thermal load per absorbed pump photon rises with increasing pumping rate. As the active region is pumped harder and gets hotter, the intrinsic quantum well gain eventually diminishes, and thermal rollover occurs at the point where the effective gain of the structure can no longer match the cavity loss: the laser switches off. The rollover characteristic of the laser is further complicated by the temperature dependence of the longitudinal confinement factor that modifies the effective gain of the active region; Γ_z defined in Eq. (3.1). If, for example, the active region is so designed as to give a narrow peak in the effective gain spectrum, it is possible for thermal rollover to occur at very low pumping rates.

The intrinsic temperature dependence of the quantum well gain arises from three effects. The first is the shift to longer wavelength of the semiconductor band gap with rising temperature, at a typical rate of $\sim 0.3 \text{ nm } ^\circ\text{C}^{-1}$. The second is thermally excited escape of the carriers over the confining potentials, and into the barrier regions, to the detriment of the internal quantum efficiency. The third is the Fermi factor, f_{cv} , which corresponds to the “population inversion” at

photon energy $\hbar\omega$ for valence and conduction band carriers governed by Fermi–Dirac statistics. Thus

$$f_{cv} = f_c - f_v \quad (3.2)$$

where f_c and f_v are the Fermi–Dirac occupation numbers of the initial and final electron states, of energy E_c and E_v , respectively. Under quasi-equilibrium conditions in a pumped quantum well these occupation numbers are determined by the quasi-Fermi levels in conduction and valence band, E_{F_c} and E_{F_v} respectively:

$$f_{c,v} = \frac{1}{1 + \exp(E_{c,v} - E_{F_{c,F_v}})/k_B T}. \quad (3.3)$$

The quasi-Fermi levels thus make the connection between temperature, carrier population and gain; in a parabolic band approximation, assuming that only a single state is bound in the well, we may write

$$E_{F_{c,F_v}} = k_B T \ln \left[\exp \left(\frac{N_{e,h} \pi \hbar^2}{m_{e,h} k_B T} \right) - 1 \right], \quad (3.4)$$

where N_e , N_h are the carrier densities per unit area of electrons and holes in the well respectively. Unless care is taken in the design of the active region to ensure an even distribution of carriers between the wells, the quasi-Fermi-level may vary significantly between the top and bottom wells of an optically-pumped structure, impairing the overall gain and the efficiency of the device.

Traditionally, edge-emitting diode laser devices are assumed to have a threshold current that depends exponentially on temperature in proportion to $\exp(T/T_0)$, where the characteristic temperature T_0 is a figure of merit that represents empirically the overall sensitivity of the device to the mechanisms outlined above. In practice, the dependence is generally faster than exponential, and T_0 is itself a function of T . In principle, an optically-pumped VECSEL, containing only insulating semiconductor layers, with correspondingly little free-carrier absorption, should exhibit a high T_0 compared with an electrically-pumped device. Tropper et al. report measurements of a ‘characteristic temperature’ for the internal quantum efficiency of an InGaAs/GaAsP/GaAs VECSEL gain structure. At an incident pump power of ~ 100 mW, and a heat sink temperature of 10°C , the quantum efficiency was indeed temperature-insensitive, with a relatively high T_0 of ~ 250 K. With increasing pump power, however, the T_0 value rapidly dropped to relatively low values around 100 K or less [104]. The progress in VECSEL power-scaling surveyed in the previous section has therefore been critically dependent on thermal management schemes that remove heat effectively from the active region, and these are the subject of the two following sections. In addition to these intrinsic mechanisms for temperature-sensitivity, there is in a surface-emitting laser the effect related to the temperature-dependent refractive index of the active region layers that has been mentioned previously. With increasing temperature, the spectral profile of the longitudinal confinement factor tunes to longer wavelengths at a rate of ~ 0.1 nm/ $^\circ\text{C}$. At a sub-cavity resonance, where the wells satisfy the resonant periodic gain condition, and lie precisely under field antinodes, Γ_z takes the value 4. If the spectrum of Γ_z is sharply peaked around this optimum condition, for example in the case of a long active region with many wells, a small temperature excursion can shift the structure into the wing of the resonance, with reduction of the effective gain by a large factor. A drop in the cavity photon number then allows the carrier concentration to rise, adding to the thermal load in the structure via effects such as Auger recombination. This is well-known as the central design problem for electrically-pumped VCSELs. An optically-pumped VECSEL can avoid a stringent condition for the alignment of a narrow peak in Γ_z at the operating point if it uses a relatively short active region, designed to operate around an antiresonance. This is, however, challenging to achieve with the large number of quantum wells needed for high power operation.

3.3. Thermal Management of optically pumped VECSELs

The VECSEL is a member of a class of laser concepts which employ thin-disk-type gain media [123]. This enables efficient heat removal from the pumped region on a large area, because the heat only needs to pass through a very thin semiconductor region of high-thermal-impedance before reaching the heat sink [99]. This reduced thickness of the semiconductor material leads to a nearly one-dimensional heat flow into the heat sink and makes the device power-scalable: for example, the output power can be doubled by applying twice the pump power to twice the mode area without raising the temperature of the gain structure. However, there comes a point at which this power scalability

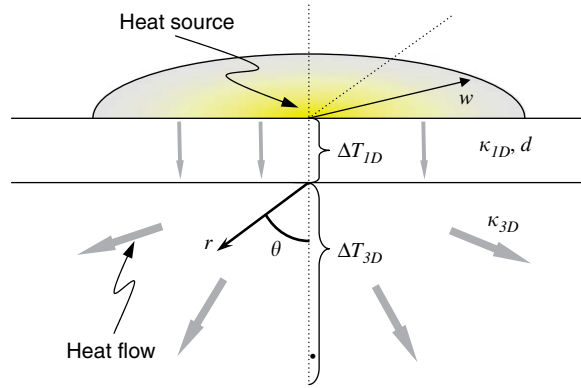


Fig. 6. Schematic of the parameters used in the analytical heat model. The parameters are described in the text.

breaks down, namely when the major part of the thermal impedance results from the heat sink (where the heat flow is not one-dimensional) and no longer from the semiconductor device (Fig. 6).

The temperature rise in the VECSEL gain structure can be modeled using analytical formulas which one obtains by solving the heat equation using a few simplifications [99]. In Fig. 6 we show a schematic of the parameters we use in this model. We assume a thin semiconductor layer (gain structure with Bragg mirror) of thickness d with relatively low thermal conductivity κ_{1D} . This layer is in intimate contact with a heat sink of larger thermal conductivity κ_{3D} . The heat source with total power P_{heat} is assumed to have a Gaussian lateral distribution with the pump beam radius w_p ($1/e^2$ -decay of the intensity) and a negligible thickness. The main idea is to separate the problem into two regions of idealized heat flow: first a thin region of one-dimensional (1D) heat flow in the high-thermal-impedance materials of the semiconductor structure and the solder layer, and after this a three-dimensional (3D) heat flow into an infinite half-space of heat spreader material, with the heatsink reference temperature at infinity.

With the pump beam radius w_p much larger than the layer thickness d , the heat flow into the heat sink is one-dimensional. The temperature drop over the 1D heat flow region in the center of the spot is:

$$\Delta T_{1D} = 2 \frac{P_{\text{heat}} d}{\pi w_p^2 \kappa_{1D}}. \quad (3.5)$$

The heat sink is kept at a constant temperature at its lower boundary. However, for mathematical convenience we expand its size to infinity. This assumption might seem surprising but it proves to be a good approximation (errors $< 10\%$) for a heat sink thicker than $3w_p$ (determined numerically). This is because most of the thermal impedance originates from the vicinity of the heat source, where the heat passes through the smallest cross-section. The further heat flow can be calculated when mirroring the half space of the heat sink to achieve infinite boundary conditions. We use a spherical coordinate system with the heat source centered in the origin

$$\rho(r, \theta, \phi) = 2 \frac{P_{\text{heat}}}{\pi w_p^2} \exp\left(-2 \frac{r^2}{w_p^2}\right) \left(\frac{\delta(\theta - \pi/2)}{r}\right), \quad (3.6)$$

where δ is the delta function and the factor $1/r$ accounts for a heat source with constant thickness in lateral direction. The temperature elevation in the center of the heat source compared to environment can be calculated by evaluating the Green's Function Solution Equation for the steady state

$$\Delta T_{3D} = 2 \frac{1}{4\pi\kappa_{3D}} \int_V \frac{1}{r} \rho dV = \frac{P_{\text{heat}}}{\sqrt{2\pi} w_p \kappa_{3D}}. \quad (3.7)$$

The factor of 2 takes into account that the heat flow is only into half space.

Note that ΔT_{1D} depends only on the heating intensity (in contrast to the heating power) while ΔT_{3D} increases with a larger pump spot but constant intensity. In order to distinguish two regimes, we define the parameter ξ as the ratio of

Table 3

A list of thermal conductivities at room temperature of materials relevant to the heatsinking of VECSEL gain structures

Material	Thermal conductivity κ /(W/(K m))
GaAs	45
AlAs	91
Al _{0,5} Ga _{0,5} As	11
Cu	400
CVD diamond	1000–1800
Composite diamond (Cobalt matrix)	600
Copper-Tungsten W-10 (CTE-matched to GaAs)	180
Al ₂ O ₃	44
SiC	490
In	82
Ti	22
Pt	71
Au	315

The numbers were taken from various sources and the values for semiconductors and composite materials were found to differ by up to 20%.

the temperature drops in the semiconductor and the heat sink:

$$\zeta \equiv \frac{\Delta T_{3D}}{\Delta T_{1D}} = \sqrt{\frac{\pi}{8}} \frac{\kappa_{1D}}{\kappa_{3D}} \frac{w_p}{d}. \quad (3.8)$$

For small pump spots, we have $\zeta \ll 1$, which means that the temperature rise is mainly caused by the one-dimensional heat flow in the semiconductor. The condition for power scaling is fulfilled, and increasing the spot size proportional to the pump power leaves temperature, slope efficiency and threshold intensity approximately unchanged. When we can provide enough pump power to keep the pump intensity constant, the achievable output power scales linearly with the spot area.

When $\zeta > 1$, the thermal impedance is dominated by the three-dimensional heat flow in the heat sink. When the pump spot size is increased while maintaining the pump intensity, the temperature is raised. That does not mean necessarily that it is no longer possible to increase the output power by making the device larger (e.g. with a material system that shows good performance even at high temperatures). However, the detrimental effects of the increased temperature on the threshold intensity and slope efficiency will eventually limit the performance of a larger device.

We can define a critical radius w_{crit} where $\zeta = 1$, so that a further increase of the pump spot size will make the thermal impedance of the heat sink surpass the one of the semiconductor structure:

$$w_{\text{crit}} = \sqrt{\frac{8}{\pi}} \frac{\kappa_{3D} d}{\kappa_{1D}}. \quad (3.9)$$

Aiming for a good performance in terms of both efficiency and maximum output power, we will choose the pump radius to be about equal to w_{crit} . In most cases, the thickness of the structure and the thermal conductivity of the semiconductor material do not allow much optimization. However, using a heat sink with a high thermal conductivity allows to increase the critical radius. Since the critical radius depends linearly on the thermal conductivity, we find a quadratic dependence of the maximum output power on this thermal conductivity. For example, a copper heat sink with ≈ 10 times higher thermal conductivity than GaAs should allow to extract 100 times more power than a gain structure on a thick GaAs substrate.

To examine the limits of validity of the analytical model, we simulated a device with a commercially available finite element software (Solidis from ISE AG, Switzerland). For the heat sink we take a cube of 5 mm size cooled from the bottom (when the semiconductor layer is on top). The simulation is run with a 4.5- μm thick Bragg mirror, a 1- μm thick active region and a 1.5- μm thick anti-reflective structure. Heat sink and semiconductor are joined with a 1- μm thick solder junction. For the thermal conductivity we use the values given in Table 3: 44 W/(K m) for GaAs, 1000 W/(K m) for Diamond, 400 W/(K m) for copper and 30 W/(K m) for the solder. For the gain structure, a superlattice of AlAs, Al_{0,2}Ga_{0,8}As and GaAs, we take the value of Al_{0,2}Ga_{0,8}As with 15 W/(K m).

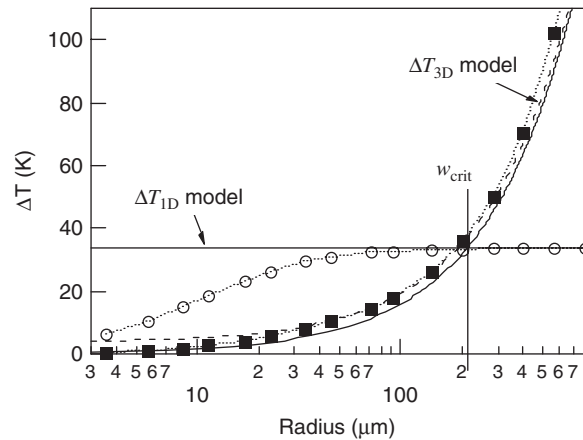


Fig. 7. Comparison with the analytical model with numerical simulations. The heating intensity is kept constant at 10.2 kW/cm^2 while the radius of the pump spot is increased. Results from the numerical simulation are plotted for the temperature drop over the thin semiconductor layer ΔT_{1D} (circles) and over the heat sink ΔT_{3D} (squares). The analytical solution are shown with solid lines only. The critical radius is marked at the crossing point of the two lines. The dashed line also considers a 1-D heat flow in the solder junction.

To compare the simulation with the analytical model we plot the temperature drops over the semiconductor and over the heat sink versus the pump beam radius Fig. 7. The heating intensity is kept constant at 10.2 kW/cm^2 . The model for a one-dimensional heat flow in the semiconductor is accurate to 10% for pump radii $> 40 \mu\text{m}$. For smaller spot sizes, the cooling is more efficient because the heat spread in lateral direction has a significant contribution already in the semiconductor layer. The model for the three-dimensional heat flow in the heat sink is accurate to 10% for spot sizes $< 600 \mu\text{m}$. For larger spots, the analytical model results in slightly lower temperatures because in the numerical model the heat flow is restricted by the sides of the heat sink. If we assume cooling from both the bottom and the sides of the copper heat sink in the numerical model, we get slightly lower temperatures than for the analytical model. For radii larger than the critical radius w_{crit} , the main contribution to the temperature elevation is caused by the heat sink. Power scaling by simply increasing the pump spot will then no longer work because the linear dependence of the temperature drop in the heat sink on the radius will eventually impair the efficiency of the laser. The critical radius is $213 \mu\text{m}$, for the configuration with $5 \mu\text{m}$ semiconductor material and a copper heat sink.

With further numerical tests we come to the following conclusions: The actual shape of the heat sink has little influence on the result; e.g., a copper cube of 1000 times the volume results in a temperature increase of only $\approx 2\%$ for a beam diameter of $400 \mu\text{m}$. Cooling the heat-sink from all sides rather than only from the bottom gives changes in the same range of a few percent. In contrast, by optically contacting a sapphire window to the front of the device for further heat removal, the temperature drop in the semiconductor structure can be reduced by $\approx 50\%$.

Fig. 8 shows simulation results for devices on a heat sink made of either diamond, copper, or a $330\text{-}\mu\text{m}$ thick GaAs wafer on copper. The dotted lines are the temperature drops in the laser structure. As expected they are independent of the heat sink below, and the three lines are superimposed. The solid lines with markers indicate the temperature drops in the heat sink. The critical radii obtained by this simulation are $24 \mu\text{m}$ for the device remaining on the substrate, $185 \mu\text{m}$ with a copper heat sink and $435 \mu\text{m}$ using a diamond heat spreader.

3.4. Thermal management with heat spreader

The use of a heat spreading window in intimate thermal contact with the active region surface to cool a VECSEL gain chip was explained briefly in Section 3.1 and Fig. 5(b). This thermal management technique was first introduced by Alford et al. [110], who demonstrated 1 W of cw 980-nm power launched into single-mode optical fiber from an InGaAs quantum well gain structure cooled by a 2-mm thick uncoated sapphire plate. The heatspreader has since been shown to be a versatile and effective tool, allowing cw output powers of $\sim 0.5 \text{ W}$ or more to be demonstrated in 4 different wavelength ranges. A $360\text{-}\mu\text{m}$ thick polycrystalline SiC heatspreader was used to demonstrate 0.5 W at 850 nm [98], and $> 2.5 \text{ W}$ at 980 nm [111]; the thermal conductivity of SiC is larger than that of sapphire

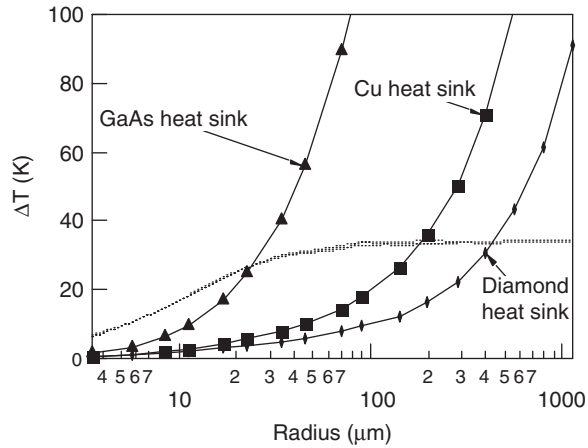


Fig. 8. Temperature plot for a constant pump intensity versus pump spot radius. The temperature differences are calculated over the semiconductor Bragg mirror (dotted line) and over the different heat sinks (solid lines with markers). The better the heat sink, the larger is the critical pump radius.

by more than an order of magnitude (see Table 3). The 980-nm device took a particularly compact microchip form, with the cavity output coupler coated directly onto the heatspreader surface. A 270- μm thick single crystal natural diamond was used to demonstrate $> 0.6\text{ W}$ at 1.32 μm [79] and 0.4 W at 660 nm [67]. High power laser operation at 1550 nm has been demonstrated using various heatspreader geometries, including 525- μm -thick Si [126], 50- μm -thick synthetic diamond [115], and 1.6-mm-thick synthetic diamond [116] with which a 780-mW output power was achieved.

Analysis of the 3-dimensional heat flow in a heatspreader-cooled gain structure is a complex problem. Heat is typically extracted from the disc-shaped heatspreader in an annular region around the circumference; the gain chip is also cooled from the lower surface. The gain chip is composed of a large number of layers, and its thermal conductivity is correspondingly anisotropic. The laser designer needs to know how the thermal impedance of the gain chip is affected by the thickness of the heatspreader, which in turn affects the laser cavity, and also how the impedance depends on the thermal conductivity of the heatspreader material. Single-crystal optical diamond offers a thermal conductivity up to ~ 40 times greater than that of sapphire—at a price. An investigation of these issues using numerical finite-element modelling has been reported by Kemp et al. [127]. These authors made the model more tractable by using a simplified layer structure, and assuming an axially symmetric temperature distribution. Their calculations showed that whereas with a sapphire heatspreader (0.44 W/(mm K)) heat flow out of the active region was distributed roughly equally between the heatspreader and the DBR, with a diamond heatspreader (2 W/(mm K)) heat flow close to the pumped volume was almost entirely into the diamond. Using diamond, the thickness of the heatspreader could be reduced to as little as 50 μm before the thermal impedance of the device began to increase significantly, and the performance was not greatly affected by the value of the inner radius of the annulus over which the heatspreader was cooled. The model predicted that a 10-W 800-nm Gaussian pump beam focused to a spot of radius 50 μm on the surface of an InGaAs/GaAs gain chip containing 14 quantum wells would produce a maximum temperature excursion of 55 $^{\circ}\text{C}$ in the presence of a 250- μm thick diamond heatspreader. Without the heatspreader, the temperature excursion was predicted to be $8\times$ as great. The model predictions were also found to be consistent with the laser data reported in [110]. The heatspreader thus allows the cooling heat flow to bypass the thick and thermally resistant DBR, with immense gain in power handling. The technique of liquid capillary bonding used to contact the gain structure to the heatspreader is relatively straightforward, and avoids extensive wafer processing [128].

A disadvantage of this thermal management technique is that the heatspreader acts as an intracavity etalon, disturbing the laser emission, which typically exhibits a broad and multiply-peaked spectrum corresponding to the etalon modes. Lindberg et al. [115] took advantage of this effect to demonstrate high power 1550-nm single frequency operation of an InGaAsP VECSEL, where a thin (50- μm) uncoated diamond heatspreader provided of itself sufficient spectral selectivity to enforce single longitudinal mode operation.

Table 4
Electrically-pumped lasers

Gain	λ_0 (nm)	d (μm)	θ ($^\circ$ half angle)	P (W)	Ref
InGaAs/GaAs	998	70	–	0.113	[129]
InGaAs/GaAs	980	400	< 10	1.4	[130]
InGaAs/GaAs	980	150	$M^2 < 10$	1	[4] ^a —NECSEL
InGaAs/GaAs	980	150	$M^2 \sim 1.05\text{--}1.1$	0.5	[4] ^a
InGaAs/GaAs	489	150	–	0.042	[133] ^a —intracavity SHG
InGaAs/GaAs	987.6	430	< 20	1.52	[131]
InGaAs/GaAs	980	21	$M^2 < 1.08$	0.0078	[134] ^a
InGaAs/GaAs	981.5	600	15	1.95	[132]
InGaAs/GaAs	970	28	$M^2 = 1.22$	0.040	[135]
InGaAsP/InP	1541	20	–	0.5 mW	[76] ^a

λ_0 : center lasing wavelength. d : aperture diameter. θ : beam divergence. P : cw power.

^aDenotes a VECSEL.

3.5. Electrically pumped VECSELS

Table 4 provides an overview of some milestone results in the development of cw electrically pumped surface-emitting semiconductor lasers. Micro-electromechanical devices are not considered here; with short plane-plane cavities they are not adapted to power scaling and spatial mode control. Peters et al. [129] were the first authors to show that large aperture VCSELs could be scaled up in power to the 100-mW level, using a bottom-emitting mesa-etched design on a diamond heatsink, with AlGaAs carrier confinement regions to limit current leakage. Miller et al. [130] demonstrated 1.4 W from a hexagonal array of 19 selectively oxidised emitters, with centre-to-centre spacing of 100- μm . Yan et al. [131] were able to achieve 1.52 W output from a single large-aperture emitter at room temperature; recently this group was able to demonstrate nearly 2 W from a single emitter with a 600- μm diameter, using an extra Au layer to suppress side-lobes in the beam [132]. The feasibility of operating surface emitting diode lasers above the 1-W level has thus been demonstrated; however the short cavity of the monolithic VCSEL results in a rather divergent multimode beam. For example, the Miller device [130] appears to exhibit a beam divergence about 2 orders of magnitude above the diffraction limit.

The first electrically-pumped VECSEL, operating at the 1-W level, with beam quality control provided by an extended cavity, was reported by researchers at Novalux [4]. This ‘NECSEL’ device uses a three-mirror linear coupled cavity design. The InGaAs quantum well active region is bounded by a highly-reflecting p-doped DBR and an n-doped DBR, in the manner of a conventional bottom-emitting VCSEL. The reflectivity of the n-DBR, however, is in the range 70–80%, so that a further mirror is needed to complete the cavity; this might be a dielectric coating on the plane lower surface of the transparent substrate, or, for TEM₀₀ mode operation with a large aperture, an external spherical mirror. These authors report 420 mW coupled into single mode optical fiber from a ~ 500 mW NECSEL with a 150- μm aperture, and ~ 1 W in a low-order multimode beam with $M^2 < 10$. A particular advantage of the NECSEL is its narrow spectral linewidth: whereas conventional short-cavity VCSELs typically emit over a bandwidth of ~ 1 nm, the high-finesse sub-cavity around the active region of the NECSEL restricts its spectral width to < 0.01 nm. This strong intracavity spectral filtering is ideally suited to efficient intracavity second harmonic generation (SHG) [133]. The sub-cavity resonance also gives rise to a distinctive light—current characteristic with a high threshold, sharply peaked at an I -value determined by the cold offset between the gain peak and the sub-cavity resonance.

An alternative approach to the design of electrically-pumped VECSELS uses a spherical micromirror fabricated on a glass substrate to complete the external cavity. Keeler et al. [135] describe a device in which a 3-quantum-well active region is flip-chip bonded to an AlN heatsink. As in the NECSEL, the upper n-DBR is partially-reflecting; light exits the active region through the n-GaAs substrate, which is thinned to 70 μm and anti-reflection coated. An air gap separates the gain structure from the microlens array, which is molded in optical epoxy resin on a glass substrate. The 28- μm aperture device emitted up to 10 mW in cw operation with $M^2 = 1.22$. Wiemer et al. [134] report a similar device in which, however, the microlens array is bonded to the active element.

4. Semiconductor saturable absorber

4.1. Semiconductor dynamics

Semiconductors are well suited absorber materials for ultrashort pulse generation. In contrast to saturable absorber mechanisms based on the Kerr effect, ultrafast semiconductor nonlinearities can be optimized independently from the laser cavity design [6,136]. In addition, ultrafast semiconductor spectroscopy techniques [137] provide the basis for many improvements of ultrashort pulse generation with semiconductor saturable absorbers.

In ultrafast semiconductor dynamics, it is often convenient to distinguish between excitonic excitations, i.e., Coulomb-bound electron–hole pairs at the band edge [138], and unbound electron–hole pairs in the continuum of the spectrum. Laser pulses with a temporal width well below 100 fs have a spectral bandwidth which is much larger than the spectral width of the exciton resonance and the exciton binding energy in most semiconductors. In addition, low-temperature (LT) MBE growth will smear out the excitonic absorption features. Therefore, saturable absorber applications with either sub-100-fs pulses or with special materials such as LT materials mostly involve continuum excitations. For this reason, we shall focus on ultrafast continuum nonlinearities and dynamics. Exciton dynamics will be discussed only for the special case of a saturable absorber based on the quantum confined Stark effect. For a comprehensive, in-depth review of ultrafast semiconductor spectroscopy the interested reader is referred to Ref. [137].

The semiconductor electronic structure gives rise to strong interaction among optical excitations on ultrafast time scales and very complex dynamics. Despite the complexity of the dynamics, different time regimes can be distinguished in the evolution of optical excitations in semiconductors. These different time regimes are schematically illustrated in Fig. 9, which shows the energy dispersion diagram of a 2-band bulk semiconductor which is typical for a III–V semiconductor material. Optical excitation with an ultrafast laser pulse prepares the semiconductor in the coherent regime (time regime I in Fig. 9). In this regime, a well-defined phase relation exists between the optical excitations and the electric field of the laser pulse and among the optical excitations themselves. The coherence among the excitations in the semiconductor gives rise to a macroscopic polarization (dipole moment density). Since the macroscopic polarization enters as a source term in Maxwell's equations, it leads to an electric field which is experimentally accessible. The magnitude and decay of the polarization provide information on the properties of the semiconductor in the coherent regime. The irreversible decay of the polarization is due to scattering processes (i.e. electron–electron and electron–phonon scattering) and is usually described by the so-called dephasing or transversal relaxation time. For a mathematical definition of this time constant the reader is referred to [137,139,140].

After the loss of coherence, ultrafast spectroscopy of semiconductors is solely concerned with the dynamics of the population, i.e., electron and hole distributions. In this incoherent regime, the time regimes II–IV Fig. 9 can be distinguished, as follows. The initial electron and hole distributions are non-thermal in most cases, i.e., they cannot be described by Fermi-Dirac statistics with a well-defined temperature [141,142]. Scattering among charge carriers is mainly responsible for the redistribution of energy within the carrier distributions and for the formation of

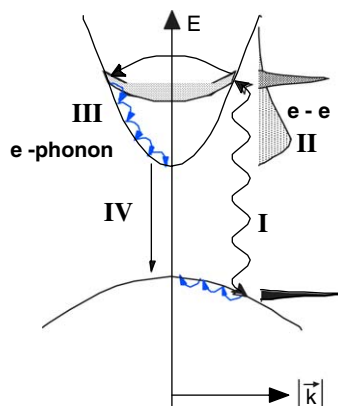


Fig. 9. Schematic dispersion diagram of a 2-band bulk semiconductor showing the time regimes I–IV after optical excitation, see text for more details. e–e: electron–electron scattering. e–phonon: electron–phonon scattering.

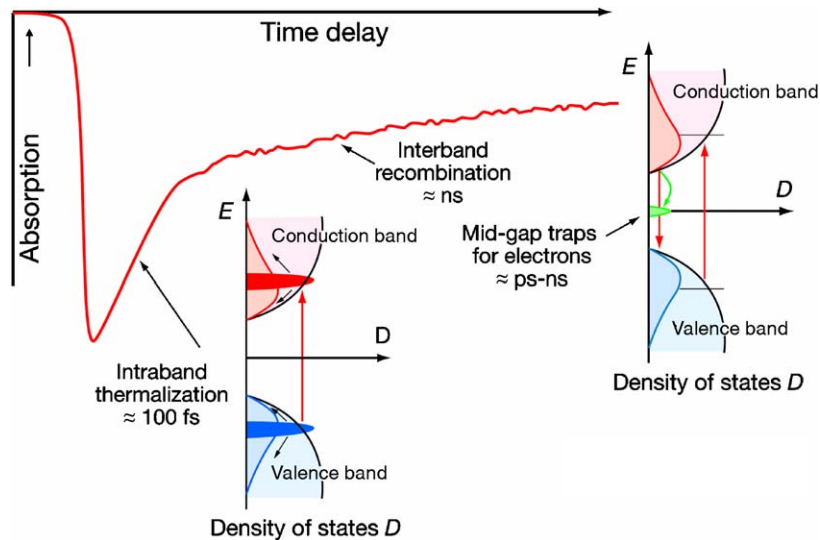


Fig. 10. Typical self-amplitude modulation (SAM) observed in a semiconductor saturable absorber.

thermal distributions. This thermalization is shown as time regime II in Fig. 9, for the example of a thermalizing electron distribution where thermalization occurs through scattering among the electrons. For excitation of the continuum, thermalization usually occurs on a time scale of 100 fs under most experimental conditions. The exact thermalization time strongly depends on the carrier density, the excess photon energy with respect to the band edge and the type of carrier [137,141–143].

In general, the carriers have a temperature different from the lattice temperature after thermalization has been completed. In Fig. 9 it is assumed that the carriers have a higher temperature than the lattice. For this case, Fig. 9 schematically shows the cooling of carriers by the emission of phonons, i.e., energy transfer to the lattice. Cooling defines the time regime III. Typical time constants are in the picosecond and tens of picosecond range.

Finally, the optically excited semiconductor returns to thermodynamic equilibrium by the recombination of electron–hole pairs. Recombination is shown as time regime IV in Fig. 9. In a perfect semiconductor crystal, recombination proceeds via the emission of photons or Auger processes at high carrier densities. These recombination processes in a good quality semiconductor (i.e. with a low level of defect states) take place on time scales of hundreds of picoseconds and longer. These slow recombination processes as well as the relatively slow carrier cooling will not be discussed in more detail in this paper. An excellent review can be found in [137].

Another ultrafast process is encountered if large densities of deep level traps are incorporated in a semiconductor. Trapping of carriers into deep levels can proceed on sub-picosecond time scales (not shown in Fig. 9). Since carrier trapping is important in many saturable absorber applications, it is discussed in more details below.

We note that the different time regimes temporally overlap. For example, a scattering process may destroy the coherence and contribute to thermalization. Nevertheless, it is very useful to distinguish between the different time regimes because they are a convenient means for the description of the complex semiconductor dynamics. The schematic picture of the different time regimes also demonstrates that two or more time constants are usually required to describe the temporal response of a semiconductor absorber. For example, we recall that thermalization typically takes place on the 100-fs time scale while carrier trapping proceeds on times scales from a few hundreds of femtoseconds to tens of picoseconds. This results in the measured self-amplitude modulation (SAM) of a semiconductor saturable absorber as shown in Fig. 10.

4.2. Important macroscopic parameters and requirements for self-amplitude modulation (SAM)

We typically integrate the semiconductor saturable absorber into a mirror structure, which results in a device whose reflectivity increases as the incident optical intensity increases. This general class of devices is called semiconductor

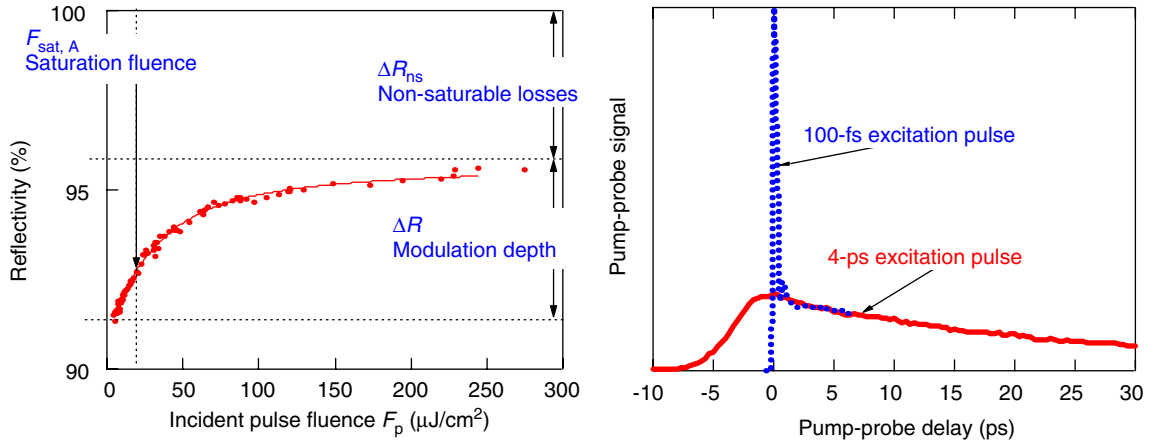


Fig. 11. Nonlinear Reflectivity as function of the incident pulse fluence F_p . The measurement was made with a SESAM supporting 34-fs pulses in a Ti:sapphire laser [199]. The measurements are fitted with common travelling wave rate equations in the slow absorber approximation which normally give a very good fit and determine the saturation fluence $F_{\text{sat,A}}$, modulation depth ΔR and nonsaturable losses ΔR_{ns} of the absorber.

saturable absorber mirrors (SESAMs) [5,7,136]. SESAMs are well-established for passive modelocking or Q -switching of many kinds of solid-state lasers [6,8,136]. In addition, semiconductor saturable absorber materials are required for the ultimate goal to fully integrate the SESAM into the VECSEL structure for wafer-scale fabrication [13]. Since both linear and nonlinear optical properties of SESAMs can be engineered over a wide range, the device performance can be readily optimized for a wide variety of laser designs and operating regimes. The main device parameters (Fig. 11) such as center operation wavelength λ_0 , modulation depth ΔR , saturation fluence $F_{\text{sat,A}}$, nonsaturable losses ΔR_{ns} and absorber recovery time τ_A can be custom designed in a wide range for either stable cw modelocking [9], or pure Q -switching [144], or a combination of both [136]. These device parameters can be measured with high accuracy [145].

One important parameter of a SESAM device is its saturation fluence, which has typical values in the range of several tens to hundreds of $\mu\text{J}/\text{cm}^2$. Lower saturation fluence is particularly relevant for fundamentally modelocked solid-state lasers and VECSELs with an ultra-high pulse repetition rate (i.e. $\gg 1$ GHz). It becomes harder to saturate the SESAM device in such a laser, as the intra-cavity pulse energy becomes increasingly lower, requiring sometimes laser mode sizes on the SESAM device on the order of only a few microns (i.e. close to the diffraction limit). In addition, lower saturation fluence will reduce thermal limitations as discussed in Section 4.7 in more details. Semiconductor saturable absorbers are ideally suited because of the large absorber cross section (in the range of 10^{-14} cm^2) and correspondingly small saturation fluence (in the range of 10 $\mu\text{J}/\text{cm}^2$). The saturation fluence can be further reduced with different materials (i.e. GaInNAs absorbers can show decreased saturation fluence [84,90,146]) and quantization levels (i.e. quantum dots [13,147]) (see Sections 3–5). In addition, the SESAM structure can be described as a multilayer design which determines the exact position of the saturable absorber layers with respect to the standing wave pattern of the incident light. The peak of the field intensity at the absorber layer then determines the saturation fluence [7,30,136] (see Section 4.6).

4.3. SAM obtained with bandfilling and fast carrier trapping

A semiconductor can absorb light if the photon energy is sufficient to excite carriers from the valence band to the conduction band. Under conditions of strong excitation, the absorption is saturated because possible initial states of the pump transition are depleted while the final states are partially occupied. Within typically 60–300 fs after the excitation, the carriers in each band thermalize, and this already leads to a partial recovery of the absorption. On a longer time scale—typically between a few ps and a few ns depending on defect engineering—they will be removed by recombination and trapping. Both processes can be used for modelocking of lasers (Fig. 10).

Processes that remove electrons and holes from the bands of a semiconductor, lead to a decay of the nonlinear transmission or reflectivity changes resulting from the interband transitions. Semiconductor saturable absorber

applications in ultrashort pulse generation often require picosecond or sub-picosecond absorber recovery times [148]. The simplest way to obtain such short absorber recovery times would be to remove the optically excited carriers from the bands a few hundreds of femtoseconds to a few tens of picosecond after they have been created. Ultrafast depletion of the semiconductor band states is also important in all-optical switching devices [149,150] and optoelectronics [151]. However, intrinsic recombination processes are usually too slow to deplete the band states of a semiconductor on picosecond or sub-picosecond time scales. One therefore generates defect states in the band gap which give rise to fast carrier trapping to deplete the bands. The trapping time is determined by the density and the type of the traps. Higher trap densities give rise to faster trapping.

Standard methods for the controlled incorporation of defect and trap states are ion implantation [152] and low-temperature (LT) molecular beam epitaxy [153]. More uncontrolled incorporation of defects occurs close to surfaces. In ion-implanted semiconductors, the trap density and the type of defect are determined by the implantation dose. The growth temperature controls the defect density in LT semiconductors where larger defect densities are incorporated at lower temperatures [154]. Semiconductor saturable absorbers can be produced either with molecular beam epitaxy (MBE) or with metal-organic chemical vapor deposition (MOVPE). MBE gives us the additional flexibility to grow semiconductors at lower temperatures, down to $\approx 200^\circ\text{C}$, while MOVPE usually requires growth temperatures of $\approx 600^\circ\text{C}$ to break up the incident molecules on the wafer surface during the growth. Lower growth temperatures lead to microscopic structural defects which act as traps for excited carriers and thus reduce the recovery time, which is beneficial for use in ultrafast lasers.

GaAs is the best understood LT grown III–V semiconductor. Low-temperature growth of GaAs is performed at temperatures of $200\text{--}400^\circ\text{C}$, as compared to about 600°C in standard MBE. During LT growth of GaAs, excess arsenic is incorporated in the form of arsenic antisites (As on Ga lattice site: As_{Ga}) at densities as large as 10^{20} cm^{-3} [154,155]. In undoped LT GaAs, more than 90% of the antisites are neutral while the rest are singly ionized due to presence of Ga vacancies (V_{Ga}) which are the native acceptors in the material (see Fig. 12(a)) [154,156]. The ionized arsenic antisites have been identified as electron traps [157]. Annealing at higher temperatures (typically 600°C and higher) converts the arsenic antisite point defects into arsenic clusters, so-called As precipitates (see Fig. 12(b)) [158]. A detailed review of the properties of LT GaAs can be found in [159,160].

The carrier trapping times in as-grown LT GaAs can be in the sub-picosecond regime and show the expected decrease with decreasing growth temperature [161,162]. Sub-picosecond recovery times of nonlinear transmission or reflectivity changes are also found in annealed LT GaAs, indicating that arsenic precipitates efficiently deplete the band states [163,164]. For more details about carrier trapping in LT semiconductors the reader is referred to [165–172].

Picosecond and sub-picosecond carrier trapping times have also been found in semiconductors implanted with various ion species [173–178]. A decrease of the trapping time with increasing ion dose was observed at lower doses [173,174,177]. At higher ion doses, the trapping time can increase with the dose [178]. The correlation of trapping times with structural properties of ion implanted semiconductors has given more insight into this unexpected dose dependence of the trapping time [179]. This work indicates that not only the defect density but also the type of defect depends on the ion dose [179]. Both the density and the type of defect affect carrier trapping, leading to longer trapping times if less effective traps are generated at higher ion doses [179].

Besides an ultrafast carrier trapping and absorber recovery time, other important saturable absorber parameters are the modulation depth and the nonsaturable losses which remain even at the highest pump energy fluences. Optimized materials combine an ultrafast recovery time with high modulation and small nonsaturable losses. This material optimization issue has been addressed in the following publications [164,168,178,180]. In these studies, the nonlinearity of continuum transitions was investigated in different modifications of GaAs. The preparation of the semiconductor layers ensured that the modulation depth and the nonsaturable losses were determined by nonlinear absorption changes.

It has been shown that standard as-grown LT GaAs with an ultrafast carrier trapping time suffers from a small absorption modulation and high nonsaturable absorption losses [164,180]. Note that large nonsaturable absorption decreases the modulation depth and causes large nonsaturable losses when the semiconductor absorber is integrated within a mirror structure. The high nonsaturable absorption mainly results from the strong defect absorption from the neutral As antisites to the conduction band ($\text{As}_{\text{Ga}}^0\text{-CB}$ transition in Fig. 12(a)) whose saturation fluence has been shown to be extremely high (i.e. $1.7\text{ mJ}/\text{cm}^2$) [180]. Therefore, as-grown undoped LT GaAs with femtosecond recovery times and high As_{Ga}^0 density suffers from high nonsaturable absorption losses. The goals of material optimization are to (i) reduce the nonsaturable absorption by the reduction of the density of neutral As antisites and (ii) to maintain a fast trapping and absorber recovery time.

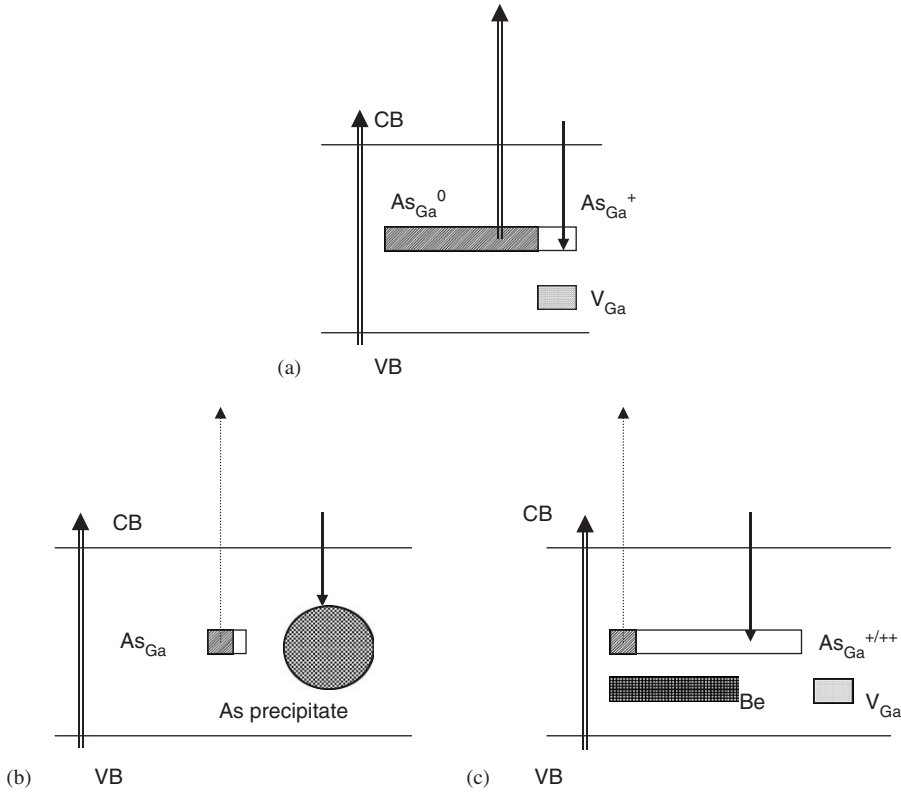


Fig. 12. Electronic structure of undoped as-grown (a), undoped annealed (b), and Beryllium doped as-grown LT GaAs. The double arrows mark strong optical absorption transitions. Weak optical absorption transitions are indicated by dotted arrows. Trapping processes are shown by arrows which point downwards.

The Keller group has demonstrated two different ways to reach these goals. Annealing of LT GaAs strongly reduces the density of neutral As antisites and the nonsaturable absorption [180]. The simultaneous reduction of the density of useful ionized As antisite electron traps does not substantially increase the absorber recovery time due to the presence of the As precipitates. Fig. 13 shows the absorption modulation and the nonsaturable absorption versus the recovery time for undoped as-grown and annealed LT-GaAs. Here we use the following notation:

$$R_{\text{lin}} = e^{-2\alpha_{\text{lin}}d} \quad \text{and} \quad R_{\text{ns}} = e^{-2\alpha_{\text{ns}}d}, \quad (4.1)$$

where d is the thickness of the LT GaAs absorber integrated in a SESAM, R_{lin} is the low fluence reflectivity and R_{ns} the fully saturated reflectivity of the SESAM (not taking into account inverse saturable absorber effects [181]). Therefore we obtain

$$\Delta\alpha = \alpha_{\text{lin}} - \alpha_{\text{ns}}, \quad \Delta R_{\text{ns}} = 1 - R_{\text{ns}} \quad \text{and} \quad \Delta R = R_{\text{ns}} - R_{\text{lin}}. \quad (4.2)$$

With decreasing growth temperature, the recovery time decreases in as-grown LT-GaAs due to the increasing density of ionized As_{Ga}^+ , which act as electron traps. However, sub-picosecond recovery times in undoped as-grown LT-GaAs are only obtained at the expense of a small absorption modulation $\Delta\alpha$ and large nonsaturable absorption α_{ns} . For a given recovery time, annealed LT-GaAs has a much larger $\Delta\alpha$ and a much smaller α_{ns} . This is because annealing results only in a slight increase of the recovery time for $T_{\text{g}} \leq 280^\circ\text{C}$ and even yields a faster response at higher growth temperatures, but largely increases $\Delta\alpha$ and decreases α_{ns} . Since annealing reduces the density of As_{Ga}^+ electron traps, a fast recovery time is maintained by the As precipitates formed upon annealing.

Fig. 14 provides insight into the microscopic origin of the weak optical nonlinearity in undoped as-grown LT-GaAs with a fast recovery time. It is found that the linear above-bandgap absorption strongly increases with increasing defect

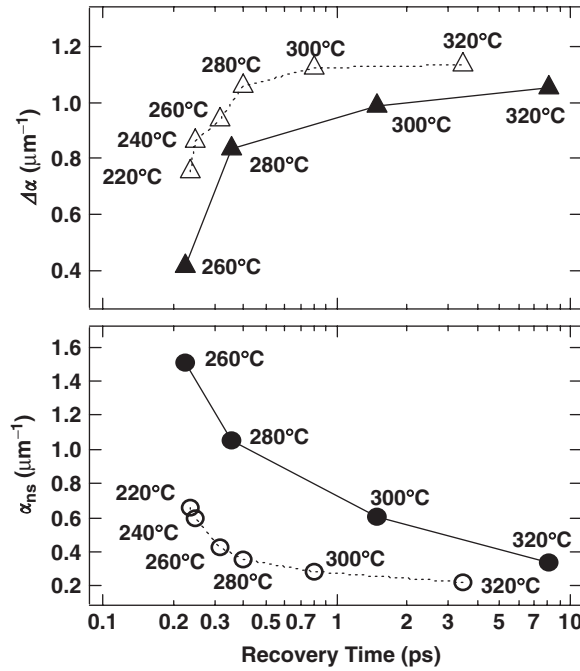


Fig. 13. Absorption modulation $\Delta\alpha$ (Δ , \blacktriangle) and nonsaturable absorption α_{ns} (\circ , \bullet) vs. recovery times for undoped as-grown (filled symbols) and undoped annealed (open symbols) LT-GaAs. Labels: growth temperatures. The recovery times have been determined at a carrier density of about $5 \times 10^{18} \text{ cm}^{-3}$.

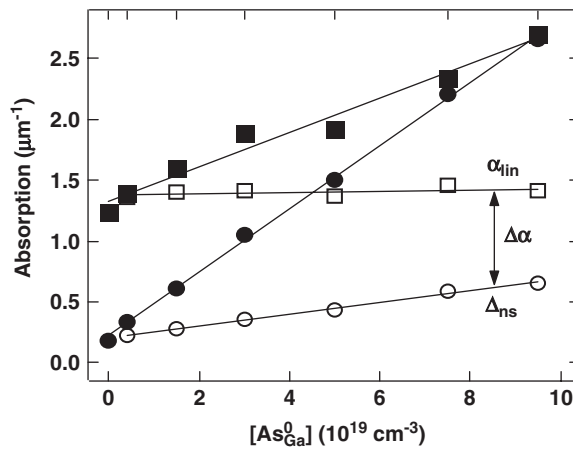


Fig. 14. Linear absorption α_{lin} (\square , \blacksquare) and nonsaturable absorption α_{ns} (\circ , \bullet) for undoped as-grown LT-GaAs samples (filled symbols) and their annealed counterparts (open symbols) vs. the neutral As antisite density in the as-grown LT-GaAs samples. The upper horizontal axis shows the growth temperature. The absorption modulation $\Delta\alpha = \alpha_{lin} - \alpha_{ns}$ is indicated by the arrow.

density in as-grown LT-GaAs. We recall that, in undoped as-grown LT-GaAs, more than 90% of the As_{Ga} are neutral while the rest is ionized [154]. For below-bandgap energies, the As_{Ga}^0 -CB transition has a much higher absorption cross section than the transition from the valence band (VB) to the ionized As_{Ga}^+ [182] and the second optical ionization of As_{Ga}^+ [183]. Consequently, we attribute the excess linear absorption in undoped as-grown GaAs to the As_{Ga}^0 -CB transition. We refer to the As_{Ga}^0 -CB absorption as α_T , given by $\alpha_T = \alpha_{lin} - \alpha_{lin}(\text{HT})$, where $\alpha_{lin}(\text{HT})$ is the linear absorption in

high-temperature undoped GaAs and “T” in α_T stands for “trap”. Our quantitative data allows for the determination of the absorption cross section σ of this transition at 830 nm. One obtains $\sigma = 1.4 \times 10^{-16} \text{ cm}^2$ from $\alpha_T = \sigma \cdot [\text{As}_{\text{Ga}}^0]$ and the linear fit to the data in Fig. 14. From σ , the saturation fluence $F_{\text{sat}} = \hbar\omega/\sigma$ of the As_{Ga}^0 -CB transition can be quantitatively determined: $F_{\text{sat}} = 1.7 \text{ mJ/cm}^2$. At this fluence, the absorption of the As_{Ga}^0 -CB transitions significantly decreases. In contrast, the saturation fluence of the interband transition in GaAs is typically below $50 \mu\text{J/cm}^2$. The comparison shows that α_T is hardly decreased by fluences which almost fully saturate the interband transition. Therefore, the As_{Ga}^0 -CB absorption α_T fully contributes to the nonsaturable absorption α_{ns} . Surprisingly, Fig. 14 shows that the absorption modulation $\Delta\alpha = \alpha_{\text{lin}} - \alpha_{\text{ns}}$ decreases with increasing As_{Ga}^0 density. This decrease cannot be due to the nonsaturable trap absorption α_T since α_T equally contributes to both α_{lin} and α_{ns} . We conclude that there must be another mechanism which gives rise to additional nonsaturable absorption γ_{ns} . The mechanism responsible for the additional absorption γ_{ns} is not yet fully understood. A possible reason for γ_{ns} is free-carrier absorption due to carriers high in the CB. These carriers can be generated by the As_{Ga}^0 -CB transition in as-grown undoped LT-GaAs. The total nonsaturable absorption can be written as $\alpha_{\text{ns}} = \alpha_T + \gamma_{\text{ns}}$. A quantitative analysis of the data in Fig. 14 shows that γ_{ns} makes up about 40% of the total nonsaturable absorption α_{ns} in as-grown undoped LT GaAs. Thus the nonsaturable As_{Ga}^0 -CB absorption α_T contributes the major fraction to α_{ns} . With respect to ultrafast all-optical switching applications, we note that the large nonsaturable As_{Ga}^0 -CB absorption α_T in as-grown undoped LT-GaAs increases the nonsaturable losses in reflectivity ΔR_{ns} and limits the reflectivity modulation ΔR . Moreover, ΔR can be strongly reduced by γ_{ns} which contributes to the nonsaturable absorption and reduces the absorption modulation. This analysis shows that LT-GaAs can be optimized for ultrafast all-optical switching applications if the density of neutral As_{Ga}^0 is reduced while an ultrafast recovery time is maintained. This goal cannot be reached in as-grown undoped LT-GaAs since the incorporation of a large density of ionized As_{Ga}^+ trap states results in the incorporation of even larger densities of neutral As_{Ga}^0 [154] which deteriorate the optical nonlinearity.

An alternative method for the optimization of LT-GaAs for ultrafast all-optical switching applications takes advantage of Be doping. Doping with Be acceptors reduces the density of neutral As antisites [184] and increases the density of ionized As_{Ga} [18]. The latter effect ensures ultrafast recovery times [6,18]. Annealed LT GaAs and Be-doped LT GaAs combine ultrafast recovery times with high modulation depth and small nonsaturable losses. These materials are well suited for saturable absorber devices in laser physics and for all-optical switching applications.

Studies of the modulation depth ΔR , the nonsaturable losses ΔR_{ns} , and the recovery time τ_A in ion implanted GaAs have shown that ΔR decreases and ΔR_{ns} increases with decreasing recovery time and higher defect concentration [178]. Nevertheless, if the ion species, ion dose, and annealing conditions are properly chosen, combinations of ΔR , ΔR_{ns} , and τ_A can be obtained which are appropriate for saturable absorber applications. Ion implanted GaAs is an alternative to annealed or Be doped LT GaAs as a material for saturable absorber devices [178].

4.4. SAM obtained with quantum-confined Stark effect

A quantum well absorber with intrinsically fast self-modulation can be realised using the non-linear response of a semiconductor excited in the spectral transparency region at an energy less than that of the exciton resonance. It is well known from atomic physics that virtual emission and reabsorption of non-resonant photons leads to a light-induced shift of the atomic energy levels. This light shift, or optical Stark shift, was first observed in a solid system by Mysyrowicz et al. [185] using pump and probe spectroscopy of GaAs/AlGaAs multiquantum well structures at low temperature. These authors reported a blue-shift of the heavy-hole and light-hole exciton resonances induced by irradiation with a sub-picosecond pulse tuned to the transparency region of the wells. No carriers are injected; the excitonic shift arises from the coupling of the exciton to virtual biexciton states, and persists only for the duration of the non-resonant pump pulse. The quantum well therefore exhibits fast saturable absorption on the low energy wing of the exciton resonance, with enhanced transmission that recovers on the timescale of the pulse duration.

The effect is shown schematically in Fig. 15, in which the absorption spectrum of an exciton resonance is sketched for a quantum well with no excitation, and then Stark-shifted in the presence of an intense non-resonant pulse. The difference between the two curves shows the spectrum of the modulation, with a band of bleached absorption over the low energy wing of the resonance. Von Lehman et al. [186] characterised this effect using picosecond pump-and-probe measurements with the pump frequency detuned to the low-energy side of the exciton resonance by 31 meV. Under these conditions, a negligibly small population of excitons is injected into the quantum well by the pump pulse, and the effects of phase space filling and Coulomb screening are correspondingly small. The differential transmission

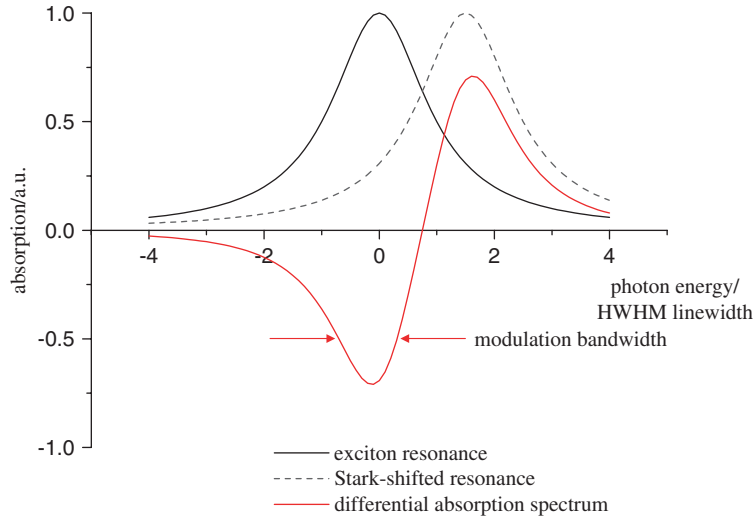


Fig. 15. Self-absorption modulation by the optical Stark effect: exciton absorption resonance, optical Stark-shifted resonance in the presence of an intense pulse (dashed line), and differential absorption spectrum (red line).

spectrum, $\Delta T/T$, of the exciton resonances measured at zero pump-probe delay exhibited a derivative lineshape of the form shown schematically in Fig. 15. The blue shift inferred from the lineshape, $\Delta\omega_{\text{Stark}}$, was shown to vary linearly with pump laser intensity, and inversely with pump detuning ΔE .

Theoretical analysis of the optical Stark effect is presented by Haug and Koch in various regimes [187]. For picosecond pulses, the envelope variation of the pulse is slow compared to the coherence lifetime of the excitons, and it is appropriate to make an adiabatic approximation. In this quasi-stationary regime the energy shift is shown to be given by

$$\Delta_{\text{Stark}} = v \left(\frac{2|\mu E_P|^2}{\hbar(\omega_X - \omega_P)} \right). \quad (4.3)$$

The factor in brackets has the form of the optical Stark shift for a two-level atom, with μ equal to the dipole moment of the transition, E_P the pump field amplitude, and $(\omega_X - \omega_P)$ the frequency detuning of the pump pulse. The dimensionless enhancement factor v , that describes the effect of electron–hole correlations, can be evaluated analytically for small detuning. Haug and Koch [187] show that for a 2D system with small detuning, the enhancement factor is 2.29 for the exciton resonance, and 4 for the continuum states in the band. Thus the band edge is more strongly blue-shifted than the exciton, which becomes more strongly bound in the presence of the Stark field. Numerical evaluation shows that this remains true for all values of detuning.

To exploit the optical Stark effect as a fast self-absorption-modulation mechanism, it is necessary to work at small detuning within the low energy wing of the exciton resonance, where the modulation depth is greatest. This has the advantage that at small detuning the shift is larger; however there is simultaneously resonant excitation of the quantum well, creating a population of real carriers. The optical Stark effect has occasionally been proposed as a mechanism to explain aspects of SESAM modelocking behaviour [188]. In Section 6.3 we describe a SESAM based on the optical Stark effect with which stable sub-500-fs pulses have been generated from a modelocked VECSEL (Fig. 16).

4.5. Quantum-dot saturable absorber

The SESAM heating problem which became apparent in picosecond modelocking experiments as described in Section 6.2.1 was the main power-limiting factor when going to higher repetition rates beyond 10 GHz with modelocked VECSELs using quantum well SESAMs (QW-SESAMs). Novel SESAM designs with lower saturation fluences were required to move to higher pulse repetition rates. Novel absorber materials with increased absorption cross sections are one alternative to reduce the saturation fluence. Quantum dots are promising candidates for this [13,147], and in the 1.3–1.5 μm wavelength regime GaInNAs absorbers can show decreased saturation fluence [84,146,90].

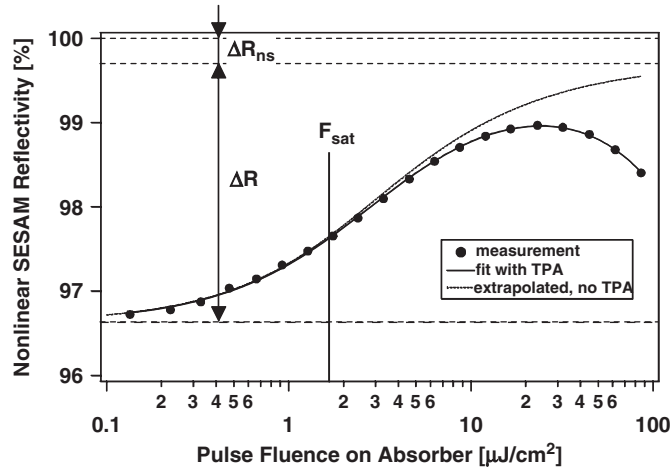


Fig. 16. Saturation-fluence measurement and fitted curves for the quantum-dot SESAM (QD-SESAM) used in the mode-locking experiments.

An early demonstration of the potential of quantum dot SESAMs (QD-SESAMs) for VECSEL modelocking was reported by Garnache et al. [124]. The absorbing structure contained 14 layers of self-assembled InAs/GaAs quantum dots (QD's) grown by MOVPE on top of an AlAs/GaAs DBR. The density of dots in each layer was $\sim 5 \times 10^{10} \text{ cm}^{-2}$, resulting in an overall saturable loss of $\sim 1\%$. The dots were grown at a high temperature, and exhibited a 100-nm broad photoluminescence spectrum centred at $\sim 1020 \text{ nm}$, with a decay times in the region of 1 ns [189]. The modelocked laser cavity was therefore designed with a pulse repetition frequency of 328 MHz to allow sufficient time for carrier recombination on each round trip. Stable modelocking was observed at a center wavelength of 1030.5 nm, in a region of strong cavity group delay dispersion: the sech^2 profile pulses were thus strongly chirped, with duration 13.2 ps, and spectral bandwidth 0.45 nm, corresponding to a time-bandwidth product that was 5.4 times Fourier-limited. An average power output of 16 mW was measured, corresponding to a pulse energy of 50 pJ.

The QD-SESAM used to passively modelock VECSELs at 10–50 GHz pulse repetition rates in the picosecond pulse width regime was designed to operate for a lasing wavelength of 955 nm and was optimized such that only one layer of quantum dots was necessary for stable modelocking. It contained a 30-pair AlAs/GaAs DBR and a single absorber layer embedded in GaAs and placed in an antinode of the standing wave pattern. In order to obtain a low $F_{\text{sat},a}$, self-assembled InAs quantum dots were used in the absorber layer. Due to their three-dimensional carrier confinement, the density of states is ideally compressed into a delta-function, which in turn results in a strongly reduced saturation fluence compared to quantum wells [190]. The structure was grown by MBE at 580 °C with the exception of the QDs, which were grown at a temperature of 300 °C, to introduce crystal defects acting as recombination centers thereby enabling fast absorber recovery times. The QDs are formed by delivering 1.8 monolayers of InAs to the sample, yielding a photoluminescence (PL) peak wavelength and FWHM of 958 nm and 36 nm, respectively. The saturation fluence measurement of the QD SESAM is shown in Fig. 16. The measurement was done with 290-fs pulses, therefore the curve shows a roll-over at high fluences due to two-photon absorption (TPA) [40,145]. The extrapolated fit curve without TPA is also plotted because it gives a better impression of the absorber behavior in the picosecond-pulsewidth domain for operation in the laser. The fit yields a low $F_{\text{sat},A}$ of only $1.7 \mu\text{J}/\text{cm}^2$. The modulation depth ΔR is 3.1% and the nonsaturable losses ΔR_{ns} are 0.3%.

4.6. SESAM structure

Besides the optimization with regards to semiconductor materials, we can further control the SAM parameters using different SESAM structure design. The SESAM is a multi-layer system which can be optimized depending on where exactly the saturable absorber material is placed inside this multi-layer system [7,191]. This can be used to further reduce the saturation fluence of the device [30] (Fig. 17).

From a historical point of view of Fig. 18 a semiconductor saturable absorber was used initially inside a nonlinear coupled cavity, in a technique termed resonant passive modelocking (RPM) (Fig. 18a) [192–194]. At that time it

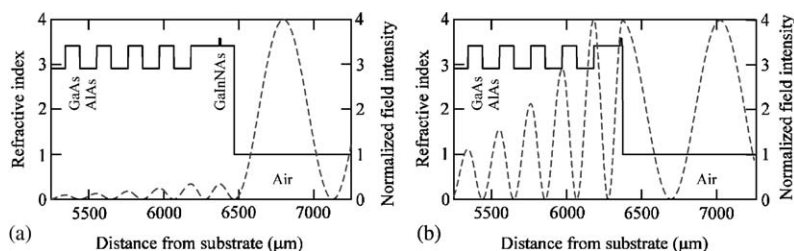


Fig. 17. Refractive index structure (solid) and calculated standing wave intensity pattern for $\lambda = 1314$ nm (dashed) close to the surface of the device for a “classical” SESAM device (a) and a SESAM device with a lower saturation fluence (b) as discussed in more details in Ref. [30].

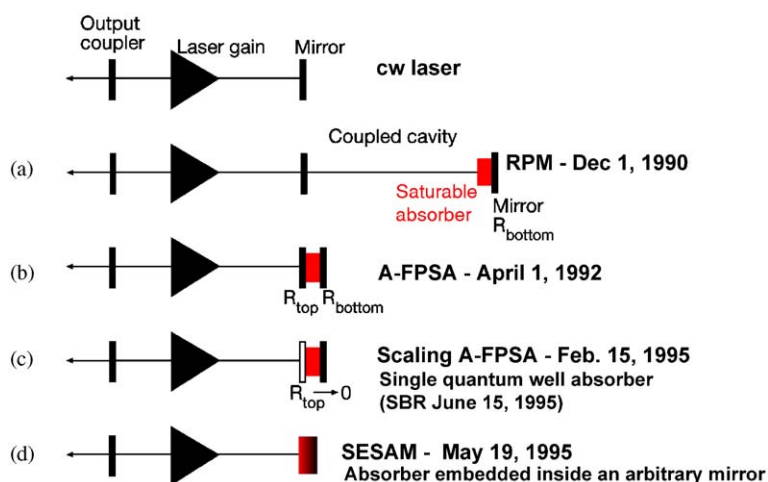


Fig. 18. Historical evolution of different SESAM designs: (a) initially the semiconductor saturable absorber was used inside a nonlinear coupled cavity, termed resonant passive modelocking (RPM) [192]; (b) first intracavity saturable absorber to passively modelock diode-pumped solid-state lasers without Q -switching instabilities: antiresonant Fabry–Perot saturable absorber (A-FPSA) [5]; (c) scaling of the A-FPSA resulted in a single quantum well saturable absorber integrated into a Bragg mirror [199]—later also referred to as saturable Bragg reflector (SBR) [200]; and (d) general concept of semiconductor saturable absorber mirror (SESAM) without any restrictions on the mirror design [7,191].

was believed that a semiconductor saturable absorber introduced too much loss to be used inside the laser cavity. In addition, it was still assumed that continuous-wave diode-pumped solid-state lasers could not in practice be passively modelocked with an intracavity saturable absorber [195]. This view was reinforced by experimental results all the way back to the first demonstration of a passively modelocked and Q -switched Nd:glass laser in 1966 [196]. More than 25 years later, the first intracavity saturable absorber that was successfully used to passively modelock a diode-pumped solid-state laser without Q -switching instabilities was the anti-resonant Fabry–Perot saturable absorber (A-FPSA) (Fig. 18b). The device consisted of a Fabry–Perot cavity filled with a saturable absorber, with its thickness adjusted for anti-resonance, so that the intensity in the cavity was substantially lower than the incident intensity [5,68,197]. The A-FPSA mirror is based on absorber layers sandwiched between the bottom AlAs/AlGaAs semiconductor and the top $\text{SiO}_2/\text{TiO}_2$ dielectric Bragg mirror. The top reflector of the A-FPSA provides an adjustable parameter that determines the intensity entering the semiconductor saturable absorber and therefore the saturation fluence of the saturable absorber device. Thus, this design allowed for a large variation of absorber parameters by simply changing absorber thickness and top reflectors [197,198]. This resulted in an even simpler SESAM design with a single quantum well absorber layer integrated into a Bragg mirror (Fig. 18c) [199], which was later also referred to as saturable Bragg reflector (SBR) [200].

In the 10-femtosecond regime with Ti:sapphire lasers, we have typically replaced the lower semiconductor Bragg mirror with a metal mirror to support the required large reflection bandwidth [201,202]. However, more recently an ultrabroadband monolithically grown fluoride semiconductor saturable absorber mirror was demonstrated that covers

nearly the entire gain spectrum of the Ti:sapphire laser. Using this SESAM inside a Ti:sapphire laser resulted in 9.5-fs pulses [203]. The reflection bandwidth was achieved with a AlGaAs/CaF₂ semiconductor Bragg mirror [204]. More recently a broadband SESAM was fabricated by increasing the reflection bandwidth of an AlGaAs/AlAs or InGaAlP/AlAs Bragg mirror using wet oxidation of AlAs which creates low-index Al_xO_y layers [205].

In a general sense we can reduce the design problem of a SESAM to the analysis of multilayered interference filters for a given desired nonlinear reflectivity response for both the amplitude and phase (Fig. 18d). More recently, novel design structures have allowed to substantial reduction of the saturation fluence of SESAMs into the 1 μJ/cm² regime [30]. The new terms “low-field-enhancement resonant-like SESAM device” (LOFERS) [206] and “enhanced SESAM device (E-SESAM)” [207] were introduced.

So far the SESAM has mostly been used as an end mirror of a standing-wave cavity. Very compact cavity designs have been achieved, for example, in passively *Q*-switched microchip lasers [208,144,72] and passively modelocked miniature lasers [50,32] where a short laser crystal defines a simple monolithic cavity. The SESAM attached directly to the laser crystal then formed one end-mirror of this laser cavity. As the laser cannot be pumped through the SESAM, the laser output needs to be separated from the collinear pump by a dichroic mirror. These examples suggest that there is need for a device that combines the nonlinear properties of the SESAM with an output coupler. This has been demonstrated before for a passively modelocked fiber laser [209] and for solid-state lasers [210].

4.7. Thermal management of SESAMs

The heating of the SESAM becomes a critical issue at higher repetition rates [13]. For a given average power level the energy per pulse decreases for increasing repetition rates, making it necessary to focus the cavity mode more tightly on the SESAM to maintain the constant level of saturation required to sustain modelocking. The same average absorbed power therefore causes a higher temperature rise at higher repetition rates because it is deposited on smaller spots.

In what follows we give an explanation of why a lower saturation fluence SESAM will reduce the heating problem of SESAMs. In addition, the low saturation fluence SESAM will support a simpler cavity design that is not operated close to the limit of stability (see Section 6.2.2). We consider a SESAM with saturation fluence $F_{\text{sat,a}}$, modulation depth ΔR and nonsaturable losses ΔR_{ns} . It is used to modelock a laser with a given average intracavity power P_{int} at a repetition rate f_{rep} , which means that the energy per pulse is $E_p = P_{\text{int}}/f_{\text{rep}}$. For stable modelocking we must also ensure that the SESAM is operated at a given saturation parameter $S > 1$ which is defined as

$$S \equiv \frac{E_p}{E_{\text{sat,a}}} = \frac{P_{\text{int}}}{F_{\text{sat,a}} A_a f_{\text{rep}}} = \frac{P_{\text{int}}}{F_{\text{sat,a}} \pi w_a^2 f_{\text{rep}}}, \quad (4.4)$$

where w_a is the $1/e^2$ radius of the Gaussian intensity distribution of the laser mode on the SESAM. We assume that a heating power P_{heat} with an associated transverse intensity distribution identical to that of the intensity of the laser mode is absorbed in a thin region near the surface of the SESAM (in the absorber and possibly also in the adjacent spacers and the mirror due to nonsaturable losses) and that it is then dissipated into an infinite half-space of substrate material with a thermal conductivity κ . This is a valid approximation for substrates thicker than $3w_a$ [99], and in this context we are dealing with laser mode radii w_a of 30 μm or less and substrate thicknesses of 300 μm or more. Under these conditions, the temperature rise ΔT in the center of the spot with reference to the ambient or heat-sink temperature is [211]:

$$\Delta T = \frac{P_{\text{heat}}}{\sqrt{2\pi} w_a \kappa}. \quad (4.5)$$

For the approximation of weak absorption (a few percent, as is typically the case in the absorbers discussed here) as well as slow absorbers (recovery time of absorber much longer than the pulse duration), it can be shown that the absorbed average power in the SESAM is [211]

$$P_{\text{heat}} = P_{\text{int}} \left(\Delta R_{\text{ns}} + \frac{\Delta R}{S} [1 - e^{-S}] \right). \quad (4.6)$$

The first term in the brackets on the right side simply accounts for the power dissipated in the nonsaturable losses, while the second term results from the absorbed pulse energy per round-trip which is necessary for bleaching the absorber. Solving Eq. (4.4) for w_a and inserting this into Eq. (4.5) and together with Eq. (4.6) yields

$$\Delta T = \frac{1}{\sqrt{2\kappa}} \sqrt{P_{\text{int}} f_{\text{rep}} F_{\text{sat,a}} S} \left(\Delta R_{\text{ns}} + \frac{\Delta R}{S} [1 - e^{-S}] \right) \propto \sqrt{f_{\text{rep}}}. \quad (4.7)$$

This is an approximation of the temperature rise in the SESAM which in reality will show small heating transients occurring at the pulse repetition rate. Simplified analytical solutions of the heat equation show that these transients superimposed on the time-average given by Eq. (4.7) are on the order of only a few Kelvins at the operating conditions relevant to this context, so the approximation is valid. The essential implication of Eq. (4.7) is that, for a given power level and given SESAM parameters, the temperature rise increases with the square root of the repetition rate.

In high-power modelocking experiments at repetition rates between 1 and 10 GHz we have observed that the maximum output power was often limited by SESAM damage (see Section 6.2.1). When calculating the SESAM temperature rise in these cases with Eq. (4.7) we obtain values of around 80 K. This is not a temperature rise at which semiconductors typically exhibit damage [212], and the reasons for this relatively low failure-temperature are not yet fully understood. One possible explanation is that this value represents a kind of threshold temperature rise at which SESAM properties degrade to a point where a thermal runaway situation could set in. This is supported by the fact that three important quantities in equation Eq. (4.7) change in a detrimental way for increasing temperatures: the thermal conductivity κ of the $\text{Al}_x\text{Ga}_{1-x}\text{As}$ material system decreases and also the bandgap energy of the absorber decreases, increasing ΔR and $F_{\text{sat,a}}$ (because the carriers are excited higher into the band). These effects can create a positive-feedback mechanism for the heating, and the temperature at which the SESAM is actually damaged could then be much higher.

From Eq. (4.7) we can now also roughly estimate the maximum power that we can obtain at higher repetition rates from VECSELS with SESAMs in cavities operated at the stability limit. With our current VECSEL devices and QW-SESAMs, the maximum power that could be extracted at 4 GHz was 2.1 W [12]. Keeping the product $P_{\text{int}} f_{\text{rep}}$ constant and assuming that we use the same output coupling, the maximum power that we can obtain with this SESAM at 40 GHz would therefore be around 200 mW.

Even for high-quality SESAMs with minimized nonsaturable losses, equation Eq. (4.7) shows that the possibilities of further reducing the heating are limited. Reducing ΔR and S to the lowest values that still ensure stable modelocking or reducing the intracavity power P_{int} by using more output coupling only offers small margins for improvement. A more significant performance gain can be expected from reducing the thermal impedance of the SESAM by substrate removal and soldering to a heat spreader material with higher thermal conductivity, thereby increasing the effective value of κ .

The real high-leverage quantity in equation Eq. (4.7), however, is the saturation fluence $F_{\text{sat,a}}$. Employing absorber materials with substantially lower $F_{\text{sat,a}}$ will effectively counteract both problems that have been outlined above. Not only does the lower $F_{\text{sat,a}}$ directly reduce the temperature rise and therefore permit an increase of the power level by the same factor, it also allows much larger mode radii w_a for the same pulse energy while maintaining the desired saturation parameter S of the SESAM, as can be seen from Eq. (4.7). This eliminates the problem of having to operate the cavity close to its stability limit and therefore makes it possible to design stable and rugged resonators suitable for real-world applications. By making use of low- $F_{\text{sat,a}}$ SESAMs, the conventional external-absorber cavities can therefore be expected to be down-scalable all the way to the practical limits of mechanical miniaturization while maintaining reasonably high average output powers.

5. Passive modelocking of VECSELS

5.1. Dynamic gain saturation

Passive modelocking mechanisms are well-explained by three fundamental models: fast saturable absorber modelocking [213,214] (Fig. 19(a)), slow saturable absorber modelocking without dynamic gain saturation in the picosecond [148] and femtosecond regime which is described by soliton modelocking [215,216] (Fig. 19(b)) and slow saturable absorber modelocking with dynamic gain saturation [217,218] (Fig. 19(c)). Dynamic saturation of the gain is only assumed in Fig. 19(c) where the gain experiences a fast, pulse-induced saturation that then recovers between consecutive

pulses. For ion-doped solid-state lasers no significant dynamic gain saturation is taking place due to the small gain cross-section of the laser which is typically more than $100,000\times$ smaller than for semiconductor lasers. The gain is only saturated to a constant value by the average intracavity intensity. This is not the case for semiconductor lasers where significant dynamic gain saturation takes place, and recovers between consecutive pulses. In this case an ultrashort net-gain window can be formed by the combined saturation of absorber and gain for which the absorber has to saturate and recover faster than the gain, while the recovery time of the saturable absorber can be much longer than the pulse duration (Fig. 19(c)).

In dynamic gain saturation modelocking as shown in Fig. 19(c) the absorber must saturate more strongly than the gain. The saturation energies $E_{\text{sat,g}}$ and $E_{\text{sat,a}}$ of gain and absorber must therefore fulfil the following inequality:

$$\frac{E_{\text{sat,a}}}{E_{\text{sat,g}}} = \frac{F_{\text{sat,a}}A_a}{F_{\text{sat,g}}A_g} \ll 1 \quad (5.1)$$

where $F_{\text{sat,g}}$, $F_{\text{sat,a}}$ and A_g , A_a are the saturation fluences and mode areas of gain and absorber. Due to the fact that $F_{\text{sat,g}}$ and $F_{\text{sat,a}}$ are of the same order of magnitude, since both gain and absorber are usually based on quantum wells of the same material system, the mode area ratio A_g/A_a must be adjusted to a value typically between 10 and 30 for stable modelocking [13]. This is a limitation for higher pulse repetition rates but can be overcome with novel low saturation fluence SESAMs. For example, a low saturation fluence quantum-dot SESAM (QD-SESAM) relaxes the mode size requirements. This allows modelocking in a simple, low-divergence cavity with identical mode areas on VECSEL gain and SESAM (i.e. 1:1 modelocking) [13]. Extremely compact cavities can be obtained with which a record repetition rate of 50 GHz in 3.1-ps pulses with 100 mW average output power has been demonstrated [14].

In addition, the lower saturation fluence of the SESAM directly reduces the temperature rise and therefore permits an increase of the power level by the same factor it also allows much larger mode radii w_a on the SESAM for the same pulse energy while maintaining the desired saturation level of the SESAM [13] (Section 4.7). This eliminates the problem of having to operate the cavity close to its stability limit and therefore makes it possible to design stable and rugged resonators suitable for real-world applications. By making use of low- $F_{\text{sat,a}}$ SESAMs, the conventional external-absorber cavities can therefore be expected to be down-scalable all the way to the practical limits of mechanical miniaturization and wafer scale integration while maintaining reasonably high average output powers.

5.2. Pulse shaping mechanisms

Using simplified models for the gain and absorption dynamics, numerical simulations [219] gave a basic understanding how parameters like group delay dispersion (GDD) or gain and absorber characteristics influence the pulse shaping

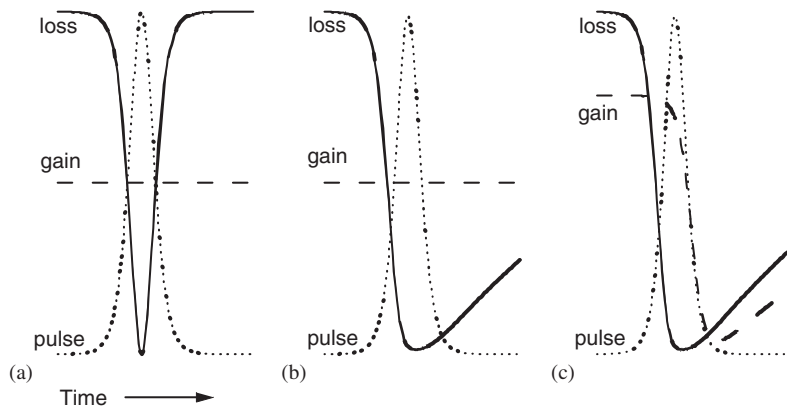


Fig. 19. Three simplified passive modelocking mechanisms: (a) a fast saturable absorber opens a short time window of positive net gain; (b) a slow saturable absorber opens a long time window of positive net gain; and (c) a slow saturable absorber in conjunction with dynamic gain saturation opens a short time window of positive net gain.

stability and the pulse duration. These simulations predicted that the laser does not necessarily have to operate at the gain maximum and that positive intracavity GDD is required for the generation of short and nearly transform-limited pulses of a few picoseconds or even sub-picosecond duration.

The pulse envelope is represented by two arrays of complex amplitudes $A(t)$ and $A(f)$, corresponding to the time and frequency domain. The complex amplitude $A(t)$ is normalized so that the instantaneous power is

$$P(t) = |A(t)|^2 \quad (5.2)$$

and the instantaneous electric field of the pulse is

$$E(t) = \text{Re}\{A(t)e^{i\omega_0 t}\}, \quad (5.3)$$

ω_0 is the center frequency of the optical spectrum of the pulse. However, this instantaneous E -field is never actually used in the calculations since all pulse-shaping effects relevant in this context take place on time scales which are much longer than the fast oscillations of the optical center frequency of the pulse. This is commonly referred to as the slowly-varying-envelope approximation and the pulse is therefore adequately described by its complex envelope $A(t)$ in all calculations discussed in the following.

The model is one-dimensional in the sense that it does not take into account the transverse distributions of gain, absorption, or refractive index in the cavity. The cavity model contains lumped optical elements which describe the effects of gain (saturable), absorption (saturable and unsaturable) and GDD. The effect of an optical element is described by an operator and is applied to the pulse either in the time or frequency domain, whichever is more suitable. After operating on the pulse in one domain, the other domain is made consistent via a Fourier Transform algorithm.

The gain is assumed to have a Gaussian spectral shape, which is simply implemented as a wavelength-dependent loss element (filter) which operates on the pulse in the frequency domain. The dynamic saturation of the gain is treated in the time domain using the differential equation [220]

$$\frac{dg}{dt} = -\frac{g - g_0}{\tau_g} - \frac{gP}{E_{\text{sat},g}}, \quad (5.4)$$

where $g(t)$ is a wavelength-independent power gain, $P(t)$ the instantaneous intracavity pulse power, g_0 the small-signal gain, $E_{\text{sat},g}$ the gain saturation energy, and τ_g the gain recovery time. The nonlinear phase change associated with the gain saturation due to the Kramers–Kronig relations is calculated in the time domain using the phenomenological linewidth enhancement factor α_g [221]:

$$\Delta\varphi(t) = -\frac{\alpha_g}{2}g(t). \quad (5.5)$$

The dynamic saturation of absorption and its associated nonlinear phase change is modeled in the same way, using a different set of parameters for saturation energy $E_{\text{sat},a}$, recovery time τ_a and linewidth enhancement factor α_a . The effect of GDD is calculated in the frequency domain in a straightforward manner by modifying the spectral phase of the pulse. The GDD is assumed to be constant (not wavelength-dependent).

$$\Delta\varphi = 2GDD\pi^2(f - f_0)^2. \quad (5.6)$$

The simulation program starts out with an arbitrary pulse shape and propagates the pulse for many cavity round-trips until a steady-state solution is found.

The model results in steady-state solutions which can be divided into two quite distinct categories. With positive GDD in the cavity, one obtains short and nearly transform-limited pulses which are slightly up-chirped. These are referred to as quasi-soliton pulses for reasons described below. With negative GDD in the cavity, steady-state solutions can also be found but one obtains long and strongly down-chirped pulses with large time-bandwidth products.

The pulse formation mechanism for the case of the short quasi-soliton pulses in the domain of positive GDD can be understood by looking at the temporal phase change of the complex pulse amplitude (Fig. 20). The fast saturation of the SESAM and the slightly delayed saturation of the gain produce a total phase change that bears a slight resemblance to the temporal pulse shape. This is similar to what happens in soliton-modelocked lasers where the nonlinear Kerr

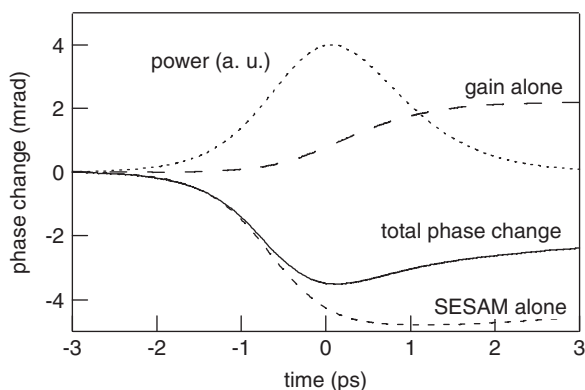


Fig. 20. The total nonlinear phase change (solid line) generated by a quasi-soliton pulse (pulse power indicated by dotted line) due to the dynamic saturation of gain and absorption. The nonlinear phase changes of gain and absorption alone are shown by the dashed lines.

effect produces a phase change which is directly proportional to the instantaneous optical pulse intensity. The nonlinear phase change can be compensated by the phase change from negative GDD. We can understand this more simply in the time domain: the nonlinear phase change from the Kerr medium produces new frequency components at times slightly before and after the pulse maximum. These new wave packets with center frequencies above and below the center frequency of the optical pulse spectrum can be temporally shifted to coincide with the pulse maximum by passing the pulse through an optical element which exhibits GDD of the proper sign and magnitude. In this way short pulses can form by spectral broadening and pulse compression on every round trip until an equilibrium is reached in combination with the spectral narrowing due to limited gain bandwidth. This results a steady-state solution where the pulse shape reproduces itself on every cavity-round trip due to the cumulated effect of all cavity elements.

The nonlinear phase change resulting from passage through a Kerr medium has the opposite sign of the total nonlinear phase change resulting from the saturation of gain and absorber in modelocked VECSELs. Therefore, if negative GDD compensates the nonlinear phase change in soliton modelocking using the Kerr effect, then one could expect that positive GDD could compensate the nonlinear phase shift in modelocked VECSELs. It was indeed possible to observe this in the simulations, and therefore the mechanism discovered in this way was named “quasi-soliton-modelocking”. The quasi-soliton pulses do not have an ideal symmetrical sech^2 shape, but their time-bandwidth products reach values down to around 0.375, which is not far from the value of 0.315 for transform-limited solitons. In addition, the chirp which is often present in pulses leads to a drift of the optical spectrum away from the gain maximum because the absorber always absorbs the leading edge of the pulse. In an up-chirped pulse, this predominantly attenuates the low-frequency parts of the spectrum and leads to a slight blue shift, whereas in a down-chirped pulse the high-frequency components are attenuated more strongly and therefore the result is a slight red shift.

The seemingly clear predictions of the model concerning the very distinct pulse characteristics in the two regimes of positive and negative GDD were unfortunately not reproduced in experiments in the simple manner that one might expect. Wavelength tuning experiments were done using Fabry–Perot etalons where the optical spectrum of the laser was forced into regions of positive or negative GDD [12]. A strong wavelength dependence of the pulse duration and modelocking stability was indeed observed, but the variation of the pulse characteristics was more complicated than the simple dependence on the intracavity GDD as predicted by the model. This indicates that the simplifications of the model are too strong to give a fully comprehensive explanation of the modelocking mechanism in VECSELs. However, the simulations did bring out important effects such as the nonlinear phase changes due to the dynamic saturation of gain and absorption as well as the spectral shifts resulting from chirped pulses which are quite unique to this kind of passively modelocked laser and which were not obvious from the start. The results of the simulations stimulated new experimental ideas and they yielded an understanding of the leading-order effects of absorption, gain and GDD which has proven valuable in the cavity design and optimization of passively modelocked VECSELs.

6. Modelocking results

6.1. Overview

A quick overview of the results achieved to date in passive modelocking of optically-pumped VECSELs is provided by the data of Table 5. It is notable that lasers with, for the most part, rather similar gain structures have been investigated in such widely-varying dynamical regimes; with pulse durations from tens of ps to less than 500 fs; repetition rates from a few hundred MHz to 50 GHz, average powers from the few-mW to the few-W regime, and pulse energies ranging from few-pJ to hundreds of pJ. The relationship between cavity design, gain and absorber saturation and pulse formation will be considered in more detail in the following sections. For now, we note that most modelocking studies to date have involved InGaAs/GaAs lasers and SESAMs at wavelengths near 1 μm . An early report of 100 ps pulse generation from an 850-nm GaAs/AlGaAs VECSEL used active modelocking with an intracavity acousto-optic modulator, and thus lies outside our present subject [122]. Casel et al. [222] report simultaneous modelocking and intracavity frequency doubling of an InGaAs VECSEL; an intracavity etalon constrained the laser wavelength to stay within the second-harmonic acceptance bandwidth of the nonlinear crystal, and also stabilised the modelocking.

A modelocked 1.5- μm InGaAsP VECSEL was reported for the first time by Hoogland et al. [73]. A recent report by Lindberg et al. [125] describes the generation of near-transform-limited 3.2-ps 1.5- μm pulses from such a VECSEL, using a 50- μm thick single crystal diamond heatspreader to overcome the poor thermal characteristics of InP-based material and achieve an average power of 120 mW. An antireflection coating on the diamond surface prevented disruption of the modelocking by etalon effects.

A modelocked 1.3- μm InGaAs VECSEL has been passively modelocked by Rutz et al. [81] for the first time. An InGaAs SESAM [84,86] has been used.

Wilcox et al. [223] have recently reported the first measurement of timing jitter in a SESAM-modelocked VECSEL. The laser emitted a train of 2.3-ps 1043-nm pulses from a cavity that was length-stabilised by locking the fundamental ~ 897 MHz pulse repetition frequency to an external radiofrequency oscillator. This preliminary characterisation established an upper limit for the timing jitter of 160 fs over the bandwidth 1 kHz to 15 MHz.

Table 5
Optically pumped VECSELs: passively modelocked using different SESAMs

Gain	λ_0	τ_p	P_{av}	f_{rep}	Ref.
<i>InGaAs-based</i>					
12 InGaAs/GaAs QWs	1030 nm	22 ps	20 mW	4.4 GHz	[10]
9 InGaAs/GaAs QWs	950 nm	3.2 ps	213 mW	2 GHz	[224]
6 InGaAs/GaAsP QWs	1030 nm	13.2 ps	16 mW	328 MHz	[124]
	1039 nm	6.8 ps	64 mW	328 MHz	[124]
	1040 nm	477 fs	100 mW	1.21 GHz	[225]
	1040 nm	486 fs	30 mW	10 GHz	[11]
6 InGaAs/GaAs QWs	1034 nm	486 fs	30 mW	10 GHz	[11]
5 InGaAs/GaAs QWs	950 nm	15 ps	950 mW	6 GHz	[99]
		3.9 ps	530 mW		[99]
		9.7 ps	55 mW	21 GHz	[13]
7 InGaAs/GaAsP QWs	980 nm	9.7 ps	55 mW	21 GHz	[13]
	960 nm	4.7 ps	25 mW	30 GHz	[13]
	957 nm	4.7 ps	2.1 W	4 GHz	[12]
	960 nm	6.1 ps	1.4 W	10 GHz	[226]
	960 nm	3 ps	100 mW	50 GHz	[227]
13 InGaAs/AlGaAsP + intracavity LBO	975 nm	3.8 ps	83 mW	1.88 GHz	[222]
	489 nm	3.9 ps	6 mW	1.88 GHz	[222]
<i>InGaAsP-based</i>					
7 InGaAsP QWs	1.5 μm	6.5 ps	14 mW	1.34 GHz	[73]
20 InGaAsP/InGaAsP QWs	1.554 μm	3.2 ps	120 mW	2.97 GHz	[125]
<i>InGaAs-based</i>					
5 GaInAs/GaAs QWs	1.308 μm	18.7 ps	57 mW	6 GHz	[81]

λ_0 : center lasing wavelength. τ_p : measured pulse duration. P_{av} : average output power. f_{rep} : pulse repetition rate.

6.2. Modelocking results in the picosecond regime

6.2.1. Modelocked VECSELS up to 10 GHz

Initial work on passively modelocked VECSELS was done in this regime using quantum-well SESAMs (QW-SESAMs). Pulse durations obtained spanned a wide range from nearly transform-limited pulses of a few picoseconds duration up to strongly chirped pulses with durations of tens of picoseconds [99]. The characteristics of the pulses depended strongly on a variety of operating conditions like the power level and the temperature. The output power of modelocked VECSELS was improved from the mW regime to > 2 W using a strain-compensated gain structure [12]. Initially, however, the pulses from the new gain structure were always strongly chirped, and no regime of pump-power level or temperature was found where transform-limited pulses could be obtained. Numerical simulations which were performed predicted that, with proper GDD management in the laser, the chirp can be reduced considerably and short and nearly transform-limited pulses can be generated [219] (Section 5.2). Under the restrictions of the assumptions and simplifications made in the model underlying the numerical simulations, one non-obvious conclusion was that positive group-delay dispersion (GDD) is desirable for the generation of transform-limited pulses. Since the gain structures presumably have negative GDD at their wavelength of maximum gain around 960 nm, it was attempted to detune their wavelength of operation using an intracavity Fabry–Perot etalon to a wavelength where their GDD is positive. This proved to be a fruitful approach which led to the demonstration of nearly transform-limited pulses at record-high average output power levels from the very same gain structures that produced only very strongly chirped pulses in “free-running” (as opposed to etalon-tuned) modelocked operation.

We first describe the VECSELS and QW-SESAMs used in these experiments which resulted in strongly chirped pulses (no etalon in the cavity) with an output power of 1.9 W at a repetition rate of 1.5 GHz. Improved pulse quality obtained by etalon-tuning resulted in pulses with drastically reduced chirp and an average output power of 2.1 W at 4 GHz. In addition, at 10 GHz nearly transform-limited pulses were demonstrated at an average output power of 1.4 W.

The VECSEL structure is grown by MOVPE and contains a total of six different III–V semiconductor compounds: GaAs, AlAs, $\text{Al}_{0.2}\text{Ga}_{0.8}\text{As}$, $\text{Al}_{0.85}\text{Ga}_{0.15}\text{As}$, $\text{In}_{0.13}\text{Ga}_{0.87}\text{As}$, and $\text{GaAs}_{0.94}\text{P}_{0.06}$. For the bottom mirror and antireflective section, $\text{Al}_{0.2}\text{Ga}_{0.8}\text{As}$ and AlAs are used, because these materials are transparent for the pump wavelength and also form a barrier for the carriers excited in the active region. In Fig. 21 the AlAs/ $\text{Al}_{0.2}\text{Ga}_{0.8}\text{As}$ bottom mirror is a 36-pair DBR with a superlattice of six periods containing 6 DBR pairs each. The active region consists of GaAs spacer layers, seven compressively-strained $\text{In}_{0.13}\text{Ga}_{0.87}\text{As}$ QWs and tensile-strained $\text{GaAs}_{0.94}\text{P}_{0.06}$ strain-compensating layers (Fig. 21). The strain-compensating layers also absorb at the pump wavelength of 808 nm. The $\text{In}_{0.13}\text{Ga}_{0.87}\text{As}$ quantum wells are each placed in separate antinodes of the standing-wave pattern. The strain-compensation layers can be either positioned in the center of the spacer sections (Fig. 21(a)) or directly adjacent to the QWs (Fig. 21(b)). These VECSELS lase at wavelengths around 950–960 nm and have performed well in high-power modelocking experiments at repetition rates between 1 and 10 GHz. The structure shown in Fig. 21(b) has shown greater power conversion efficiency in cw experiments, which could be due to the better carrier confinement in the QWs because the strain-compensating layers are directly adjacent to the QWs. However, it has not been possible to modelock this structure at repetition rates above 10 GHz. The structure is grown in reverse order, starting with three etch-stop layers ($\text{Al}_{0.85}\text{Ga}_{0.15}\text{As}$, GaAs, AlAs), used for the substrate removal process, followed by the antireflective section, the active region, and finally the bottom mirror (Fig. 21(c)). The active region is grown at a lower temperature of 660 °C than the rest of the structure (720 °C). The reason for the different temperatures is that the quality of the $\text{In}_{0.13}\text{Ga}_{0.87}\text{As}$ is improved at 660 °C, whilst the growth rate of AlAs is too small at lower temperatures.

The threshold pump intensity of the VECSEL structure shown in Fig. 21(a) in a V-cavity using 2.5% output coupling is approximately 3.5 kW/cm^2 . From slope measurements with variable output coupling, the saturation intensity I_{sat} was determined to be approximately $1.2 \times 10^9 \text{ W/m}^2$ using a simple idealized 4-level gain model. The cw lasing properties of the VECSEL were investigated in a simple straight cavity setup. The output coupler with 1.5% transmission and a radius of curvature (ROC) of 200 mm was placed in a distance of 153 mm from the gain chip. The slope and M^2 measurements are shown in Fig. 22. The slope was recorded at a heat sink temperature of -5 °C. After the threshold power of 1.93 W the output power increases with a slope efficiency of 33.7%. A rollover can be observed starting at about 15 W pump power and 4 W output power. At an output power of 4.4 W the beam quality of the VECSEL is still very good as shown in the beam quality measurement with values $M^2 < 1.15$ in both directions.

In the 1–10 GHz regime two different quantum well SESAMs (QW-SESAMs) have been used for passive mode-locking: One is grown by MBE and the other by MOVPE.

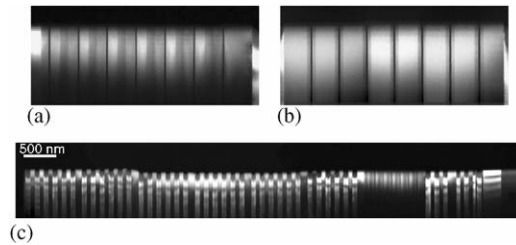


Fig. 21. TEM micrographs of grown structures: (a) active region with strain-compensation layers placed in the center of the GaAs spacers; (b) active region with the strain-compensation layers directly adjacent to the QWs on either side; and (c) a complete gain structure grown upside-down. The substrate is visible on the right. The thick layer immediately next to the substrate is the $\text{Al}_{0.85}\text{Ga}_{0.15}\text{As}$ etch-stop. The 8-nm thick QWs are actually visible as the thin dark lines in (a) and (b).

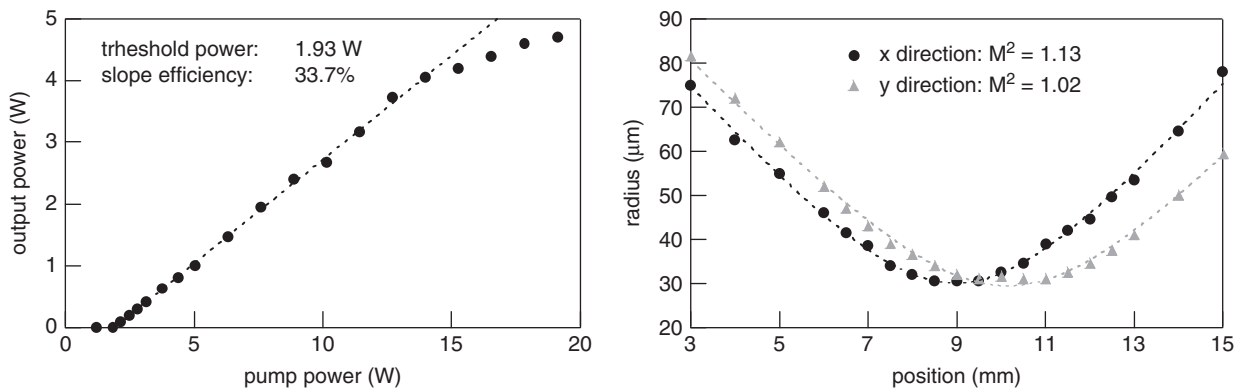


Fig. 22. CW characteristics of the VECSEL structure shown in Fig. 21(a). Left: slope measurement. Right: beam quality measurement at an output power of 4.4 W.

The MBE QW-SESAM is a low-finesse SESAM containing a single low-temperature MBE-grown (350°C), 8.5-nm thick InGaAs QW. The absorber shows an excitonic dip at 959 nm. The saturation fluence $F_{\text{sat,a}}$ is about $20 \mu\text{J}/\text{cm}^2$ at 960 nm. The modulation depth ΔR is 1% on the short-wavelength side of the exciton and $> 2\%$ at the exciton peak. Pump-probe measurements at 960 nm with 200-fs pulses and a spectrum of 10 nm width at a repetition rate of 80 MHz were performed. The SESAM is quite fast with a recovery time of less than 10 ps for a low pump fluence of $50 \mu\text{J}/\text{cm}^2$ and 26 ps at a high fluence of $500 \mu\text{J}/\text{cm}^2$. Therefore this SESAM almost fully recovers for repetition rates as high as 10 GHz.

The MOVPE QW-SESAM is grown at normal growth temperatures (typical values are around 700°C , depending on the material). The bandgap of the 5-nm thick QW is at a wavelength $> 985 \text{ nm}$, outside the stopband of the DBR. Due to the VECSEL emission wavelength of around 960 nm the absorber operated $> 25 \text{ nm}$ over the bandgap. Therefore the saturation fluence is quite large with $F_{\text{sat,a}} > 200 \mu\text{J}/\text{cm}^2$ because more carriers have to be excited to saturate the SESAM. The carrier recovery time is 27 ps (measured at a pulse fluence of $500 \mu\text{J}/\text{cm}^2$) due to surface defect traps, which is comparable to that of low-temperature MBE-grown SESAMs.

The cavity initially used for modelocking was Z-shaped (Fig. 23), optimized for operation at 1.5 GHz using the VECSEL gain structure shown in Fig. 21(a). The two end mirrors were the MBE QW-SESAM and an output coupler with 2.5% transmission and 100 mm ROC. The gain structure (Fig. 21(a)) and a curved mirror with a transmission of 0.35% (ROC = 38 mm) formed the two cavity folding mirrors. This configuration gave the flexibility to adjust the mode sizes on the VECSEL and SESAM independently by choosing proper arm lengths. The total output coupling of the laser was 3.2% ($2.5\% + 2 \times 0.35\%$) due to the fact that the second folding mirror was not highly reflecting. The laser is pumped with 18 W of pump power at 808 nm from a fiber-coupled diode array with a fiber core

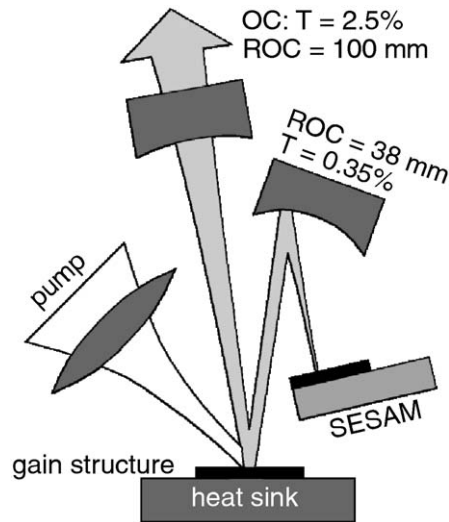


Fig. 23. The double-folded “Z”-cavity which was used for the high-power modelocking experiments at 1.5 GHz. These cavities can be designed for allowing an almost independent adjustment of the mode radius on the gain and on the absorber by varying the arm lengths. An output coupler with 0.35% transmission was used as a folding mirror because no high-reflector was available.

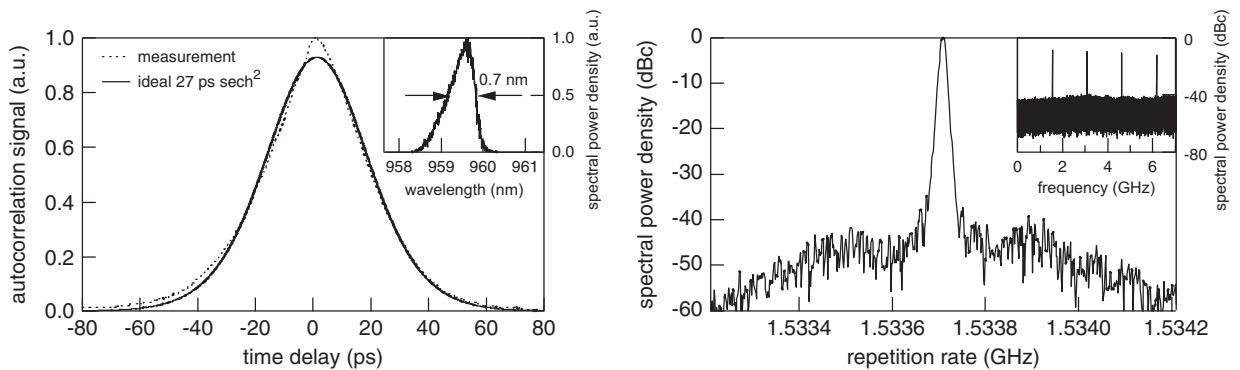


Fig. 24. Modelocking results of laser cavity shown in Fig. 23: strongly chirped pulses with 1.87 W average output power at a repetition rate of 1.5 GHz. Results obtained using the VECSEL gain structure (Fig. 21(b)) and the MBE QW-SESAM. Left: autocorrelation of the 27-ps pulses and the optical spectrum with a FWHM of 0.7 nm (inset). Right: RF spectrum of a fast-photodiode signal, taken at a 1-MHz span and 30-kHz resolution bandwidth. The inset shows the RF spectrum on a 7-GHz span.

diameter of 800 μm . The pump angle was 45°. The pump beam is focused on a spot of radii 175 $\mu\text{m} \times 155 \mu\text{m}$. About 15% of the pump power is reflected from the gain structure. The pump reflection consists of two contributions: the residual reflectivity from the top coating and the fraction which is not absorbed in the active region. The modelocking results are shown in Fig. 24 with strongly chirped pulses of about 20 times the transform limit. The RF measurement shows a pedestal of noise sidebands, but they are suppressed by more than 35 dBc. The large-span measurement over 7 GHz demonstrates that higher-order spatial modes, which would lead to additional beat frequencies, are strongly suppressed.

The use of an intracavity Fabry–Perot etalon led to a drastic improvement of the pulse quality of our modelocked VECSELs. Either a 20- or a 50- μm thick uncoated fused-silica etalon was used. Such ultra-thin etalons have large free spectral ranges of 15.9 and 6.4 nm (for 20 and 50 μm thickness, respectively). Due to their low finesse of 0.6 (only Fresnel-reflection at the fused-silica/air interface), they had a very broad passband and did not cause detrimental

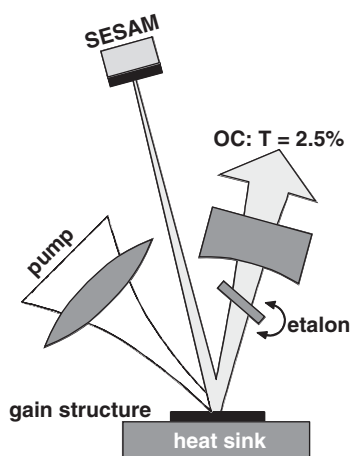


Fig. 25. The “V”-type cavity which was used for the modelocking experiments at 4 and 10 GHz.

spectral narrowing for picosecond pulses with spectral widths of about 0.5 nm. Nevertheless, the filtering effect was strong enough to restrict the center wavelength of the spectrum to a desired region by angle-tuning (changing the etalon angle to values other than normal incidence). Because the resulting center wavelength was not constrained to lie in the exact center of the etalon passband, the etalon could introduce significant amounts of GDD into the laser (up to several 100 fs^2). The experiments with etalon-tuned modelocked VECSELs were performed at slightly higher repetition rates of 4 and 10 GHz because some modelocking instabilities associated with high intracavity pulse energy had been observed in previous experiments at repetition rates around 1.5 GHz. (Note that this repetition rate was imposed by the design limitations of the Z-shaped cavities). A high pulse energy on the gain structure causes strong gain saturation, which has repeatedly been observed to lead to pulse break-up in modelocked VECSELs (this can easily be seen by monitoring the autocorrelation trace on the oscilloscope because multiple-pulse breakup produces characteristic multiple-peak autocorrelation patterns). This effect can be understood as follows: the gain is less strongly saturated by splitting up the circulating energy into several pulses and therefore these multiple pulses will experience higher round-trip gain than a single pulse. Therefore the situation where two or more pulses circulate in the cavity becomes the preferred mode of operation above a certain power level. The VECSEL gain structure which was used for the etalon-tuned modelocking experiments at 4 and 10 GHz was shown in Fig. 21(b). This gain structure performed slightly better.

The etalon is placed in the arm of the output coupler (Fig. 25). In this way one can simultaneously achieve a good coverage of the pump spot with $175 \mu\text{m}$ radius and also form a tightly focused spot on the SESAM ($\approx 50 \mu\text{m}$ at 4 GHz and $\approx 30 \mu\text{m}$ at 10 GHz). In addition, the pump light still needs to be able to pass unobstructed next to the output coupler. For both repetition rates, the output coupler had a transmission of 2.5%. At 4 GHz the ROC was 38 mm and at 10 GHz 15 mm.

For modelocking at 4 GHz the MBE QW-SESAM and an uncoated fused-silica etalon of $20 \mu\text{m}$ thickness was used to tune the wavelength. The heat sink temperature during the experiment was 1.7°C , and the laser was pumped with 18.9 W at 808 nm under a pump angle of 55° . The cavity-folding half-angle was 15° (angle of incidence of the laser onto the gain chip). Up to 2.08 W were obtained in 4.7-ps pulses, corresponding to a peak power of 98 W. The autocorrelation trace and the sech^2 -fit are shown in Fig. 26. The optical spectrum shows a bulge on the long wavelength side and a time-bandwidth product using the FWHM of this spectrum would not be very meaningful. Instead, it was calculated numerically that this optical spectrum, in the case of a flat spectral phase, would potentially allow transform-limited pulses of 2.3 ps duration. The RF measurements show clean modelocking without higher-order transverse modes. The output power which could be extracted from this modelocked VECSEL was limited by SESAM damage rather than multiple-pulse breakup instabilities, which were a problem at repetition rates around 1.5 GHz. For higher output powers than 2.1 W the SESAM was damaged before multi-pulse operation of the VECSEL could be observed.

The cavity conditions for modelocking at 10 GHz are similar to those of the 4 GHz result, except that the output coupler had a ROC of 15 mm and the other MOVPE QW-SESAM was used. The spot radius on the SESAM was about

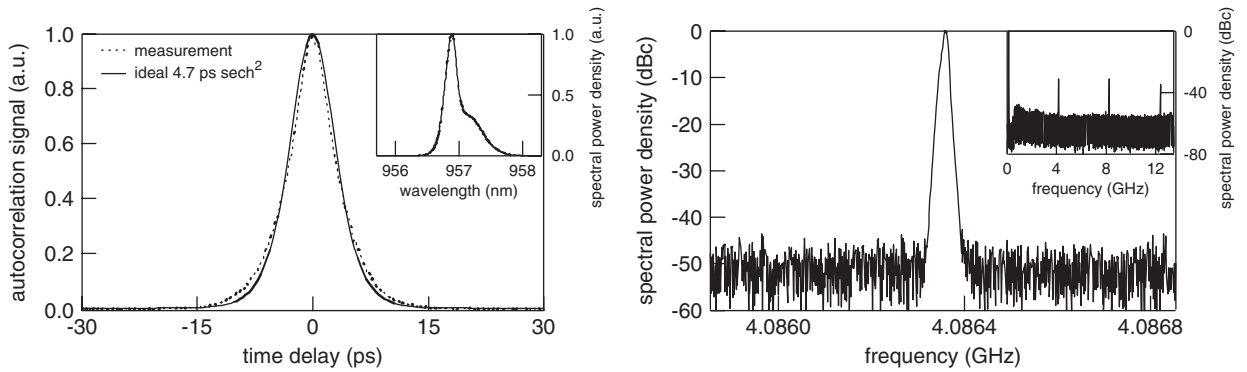


Fig. 26. Modelocking results of laser cavity shown in Fig. 25 at 4 GHz: 2.08-W average output power. Results obtained using the VECSEL gain structure (Fig. 21(b)) and the MOVPE QW-SESAM. Left: autocorrelation of the 4.7-ps pulses and the optical spectrum (inset). Right: RF spectrum of a fast-photodiode signal, taken at a 1-MHz span and 30-kHz resolution bandwidth. The inset shows the RF spectrum on a 13-GHz span.

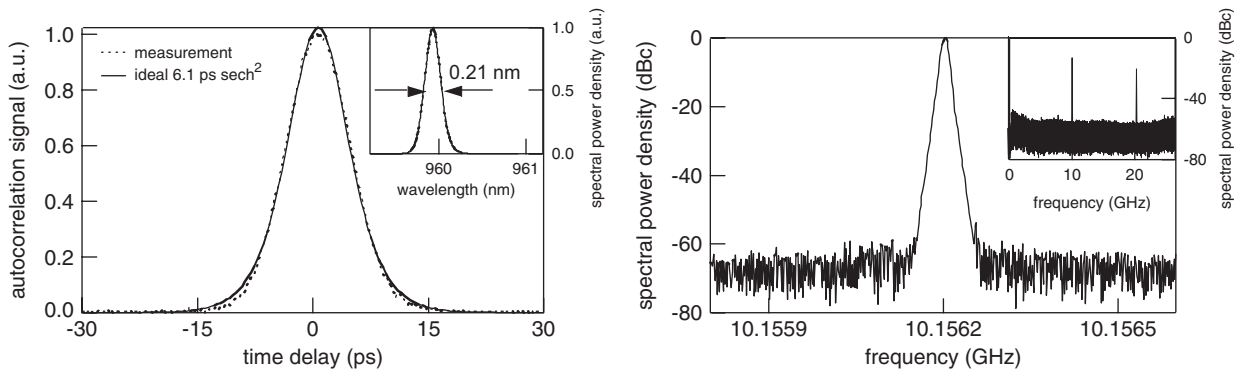


Fig. 27. Modelocking results of laser cavity shown in Fig. 25 at 10 GHz: 1.43-W average output power. Results obtained using the VECSEL gain structure (Fig. 21(b)) and the MOVPE QW-SESAM. Left: autocorrelation of the 6.1-ps pulses and the optical spectrum with a FWHM of 0.21 nm (inset). Right: RF spectrum of a fast-photodiode signal, taken at a 1-MHz span and 30-kHz resolution bandwidth. The inset shows the RF spectrum on a 26-GHz span.

30 μm . The heat sink temperature was held at 5 $^{\circ}\text{C}$. The 20- μm etalon which had been used at 4 GHz was replaced by a 50- μm thick uncoated fused silica etalon, for the simple reason that the 20- μm etalon was mounted in a circular aperture which did not fit into the densely packed folded 15-mm long cavity. The 50- μm etalon was smaller (transverse dimensions 2 mm \times 4 mm, mounted free-standing on the end of a 2-mm wide strip of stainless steel) due to space problems in the cavity. Unfortunately the optical quality of the 50- μm etalon was much worse than that of the 20- μm thick one, because it had been custom-made by a different manufacturer who was not able to meet the surface-quality specifications when polishing such thin devices. However, it was nonetheless possible to find one or two isolated spots on the etalon which introduced only minimal scattering losses into the laser. For the 50- μm thick etalon, the maximum dispersion is higher (7900 fs 2) compared to the 20- μm etalon (1200 fs 2). The smaller free spectral range of 6.4 nm was still enough to confine the optical spectrum within one passband of the etalon. The bulge on the long wavelength side of the spectrum is no longer present at 10 GHz (Fig. 27). The spectrum looks symmetric, and a sech 2 -fit yields a FWHM of 0.21 nm. This is not an effect resulting from the thicker etalon, because the bulge is still present when the 50- μm thick etalon is built in into the 4-GHz cavity. The autocorrelation can be fitted quite accurately to that of an ideal 6.1-ps sech 2 pulse, and the time-bandwidth product of 0.42 corresponds to 1.3 times the transform limit for sech 2 pulses. The data was recorded at 1.43 W average output power, corresponding to a peak power of 21 W. When using the MBE QW-SESAM instead of the MOVPE QW-SESAM, similar pulse characteristics were obtained except

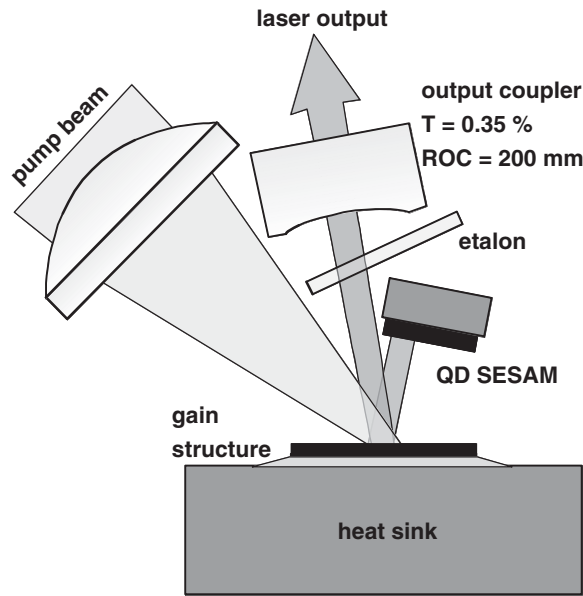


Fig. 28. The “V”-type cavity used for 1:1 modelocking.

that the maximum achievable output power was restricted to a value of 1.01 W compared to the 1.43 W. Both SESAMs showed a power drop or even irreversible damage when we tried to extract more output power. At 10 GHz the damage already sets in at a lower power level because of the smaller spot size on the SESAM.

6.2.2. 1:1 Modelocking

A low saturation fluence QD-SESAM as described in Section 4.5 was used for modelocking at higher pulse repetition rates [13]. A low- $F_{\text{sat,a}}$ SESAMs are the key for maintaining high average powers at high repetition rates with VECSELS due to limitations imposed by thermal issues and cavity-stability problems when employing conventional QW-SESAMs (see Section 4.7). It should be pointed out that these issues are not specific to VECSELS, and therefore other kinds of modelocked lasers can also be expected to experience a noticeable performance boost with low- $F_{\text{sat,a}}$ SESAMs. The QD-SESAM made it possible for the first time to demonstrate the modelocking of VECSELS in a cavity configuration with the same mode areas on gain and absorber (Fig. 28), which is referred to as 1:1 modelocking. This also proves the feasibility of the integrated-absorber VECSEL concept. The fast recovery time of this SESAM allowed us to modelock at 21 and 30 GHz, showing that this absorber material is suitable for very high repetition rates. In fact, the repetition rate was not limited by the absorber characteristics but rather by the mechanical boundary conditions imposed by the dimensions of the cavity components and the optical pumping. The low- $F_{\text{sat,a}}$ QD-SESAM still exhibits a rather large modulation depth as well as fairly high nonsaturable losses and will need further optimization in order to exploit the full potential of VECSELS in terms of output power.

The QD-SESAM as described in Section 4.5 was installed in the cavity setup shown in Fig. 28. The total cavity length was 7.1 mm at a repetition rate of 21 GHz and 5 mm for 30 GHz. An output coupler with a large radius of curvature of 200 mm was used, resulting in a very weakly focused mode that had practically identical mode radii of about $90 \mu\text{m}$ on the gain and the absorber. An output coupler transmission of only 0.35% had to be used (compared to 2.5% as a typical value for our modelocked VECSELS) because the SESAM had high small-signal losses due to the large modulation depth which was higher than desired. The output powers that could be extracted were therefore quite low and are not representative of the high-power capabilities of VECSELS. The pump source was a commercial 808-nm diode module capable of delivering up to 4.2 W in a homogenized beam with the same M^2 of about 13 in both axes, focused down to a nearly circular pump spot with radii of 92 and $85 \mu\text{m}$. A $20\text{-}\mu\text{m}$ uncoated fused-silica etalon was used for tuning the laser wavelength into regions where the total intracavity group delay dispersion (GDD) is expected to be positive, which has been shown to be favorable for obtaining stable modelocking and short pulses [219].

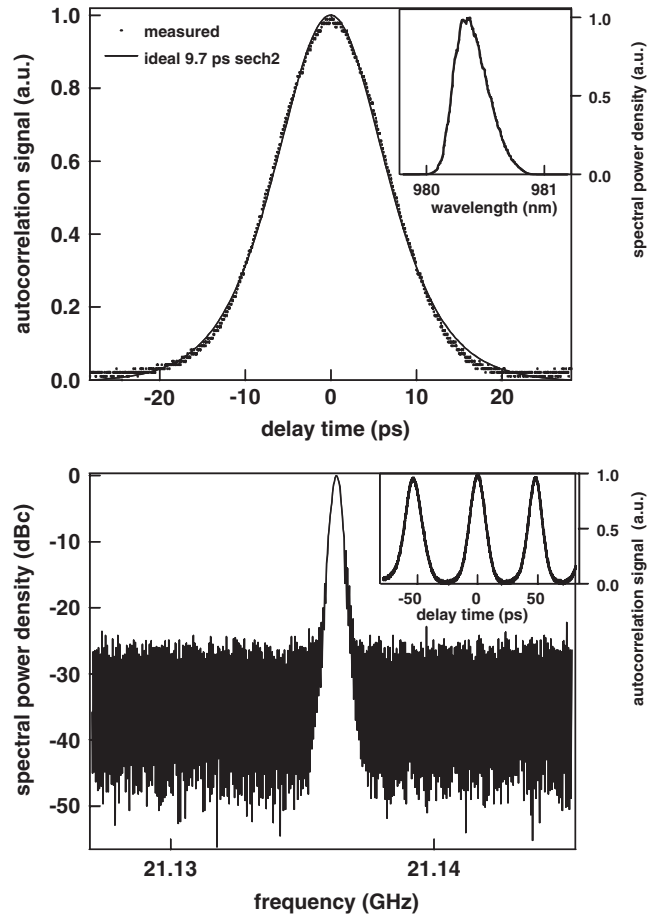


Fig. 29. Modelocking results of laser cavity shown in Fig. 28 at 21 GHz; 55 mW average output power. Results obtained using a slightly modified VECSEL gain structure and the QD-SESAM. Top: autocorrelation of the pulses. The inset shows the optical spectrum. Bottom: RF spectrum on a 20-MHz span and with 300-kHz resolution bandwidth. The inset shows a wide-scan autocorrelation of the pulse train.

Initially a slightly modified VECSEL structure has been used. Apart from a thicker DBR with 42-pairs instead of 36 pairs, the main difference compared to the structure described in Fig. 21(a) is that $\text{Al}_{0.06}\text{Ga}_{0.94}\text{As}$ is used instead of GaAs in the pump-absorption layers. $\text{Al}_{0.06}\text{Ga}_{0.94}\text{As}$ has the same band gap energy as $\text{GaAs}_{0.94}\text{P}_{0.06}$ and therefore the strain-compensation layers do not represent barriers for the absorbed carriers when they diffuse into the QWs. The strain-compensation layers are positioned directly adjacent to the QWs on both sides as shown in Fig. 21(b). This gain structure lases at longer wavelengths around 975–980 nm. It has shown moderate output-power capabilities (about 1.5 W maximum) in high-power modelocking experiments at repetition rates between 1 and 10 GHz. It has also been modelocked at repetition rates up to 21 GHz; but an attempt to mode-lock this structure at 50 GHz was not successful. This slightly modified gain structure was chosen to avoid the high losses in the vicinity of the QD-SESAM resonance at 955 nm. From the post-growth characterization of this gain structure, the GDD was calculated to be positive in the wavelength interval between 958 and 977 nm (with an estimated error of around 2 nm). With the etalon we were able to tune the wavelength from 975 to 981 nm: modelocking was possible over this entire range, with a weak trend towards shorter pulses at shorter wavelengths, although with lower output power because of the proximity to the SESAM resonance. The pulse characterization of our best result is shown in Fig. 29. The incident pump power was 2.5 W and the heatsink of the gain structure was held at 30 °C. The autocorrelation can be fitted well with an ideal sech^2 pulse of 9.7 ps duration. The optical spectrum is centered at 980.3 nm with a FWHM of 0.33 nm. At the time of the experiment only a time-domain optimized photodiode with an approximate 3-dB bandwidth of 17 GHz was available, so the RF spectrum does not have a very good signal to noise ratio. However, the wide-scan autocorrelation shows a stable 21 GHz

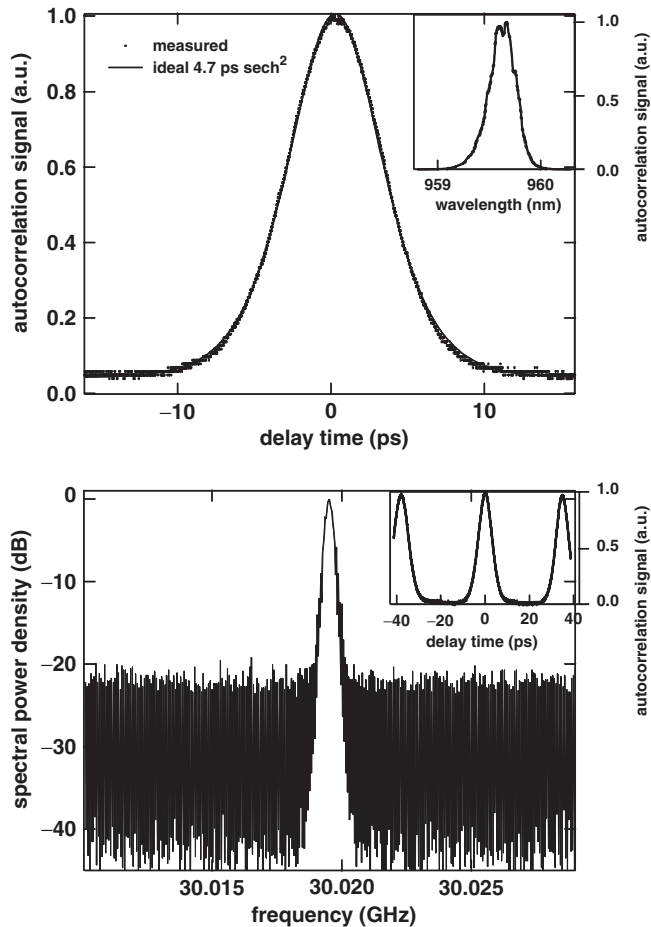


Fig. 30. Modelocking results of laser cavity shown in Fig. 28 at 21 GHz: 25 mW average output power. Results obtained using the VECSEL gain structure (Fig. 21(a)) and the QD-SESAM. Top: autocorrelation of the pulses. The inset shows the optical spectrum. Bottom: RF spectrum on a 20-MHz span and with 300-kHz resolution bandwidth. The inset shows a wide-scan autocorrelation of the pulse train.

pulse train with clearly separated pulses. The time-bandwidth product of 1.0 is 3.2 times above the transform limit, indicating that the pulses are moderately chirped.

The original VECSEL gain structure (Fig. 21(a)) which lases at shorter wavelengths around 955 nm was then installed in the cavity. Even though this is right at the QD-SESAM resonance, it was possible to get the VECSEL to lase and to tune it over the range of 947 to 960 nm. The GDD of this structure was calculated to be positive in the range from 940 to 957 nm (again with an uncertainty of about 2 nm). Mode locking was only observed in the wavelength range 958 to 960 nm. By optimizing the cavity length the repetition rate was increased to 30 GHz. The best result with an average output power of 25 mW is shown in Fig. 30. The incident pump power was 2.9 W and the heatsink of the gain structure was held at 16 °C. The autocorrelation can be fitted well with an ideal sech^2 pulse of 4.7 ps duration. The optical spectrum is centered at 959.6 nm with a FWHM of 0.31 nm. The insufficient bandwidth of the photodiode again limits the signal to noise ratio of the RF spectrum, but the wide-scan autocorrelation shows a clean 30-GHz pulse train with clearly separated pulses. The pulse quality is good with a time-bandwidth product of 0.5, which is only 1.6 times above the transform limit.

6.2.3. Modelocked VECSELs at 50 GHz

The goal of these experiments was to explore the upper repetition-rate limits of the concept of modelocked VECSELs using conventional cavity setups using separate gain and absorber components [14]. A new pump setup had to be built

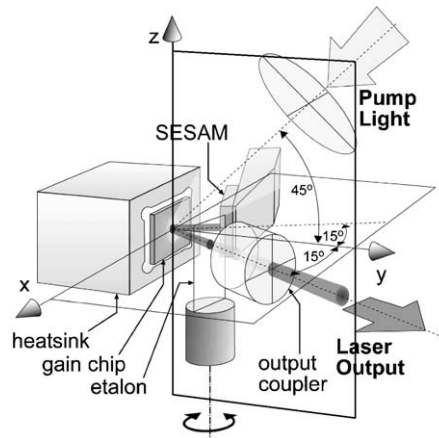


Fig. 31. The cavity setup for the 50-GHz VECSELs. The pump beam is incident from the top at a 45° angle in the vertical plane (yz -plane), whereas the cavity is folded with a half-angle of 15° in the horizontal plane (xy -plane).

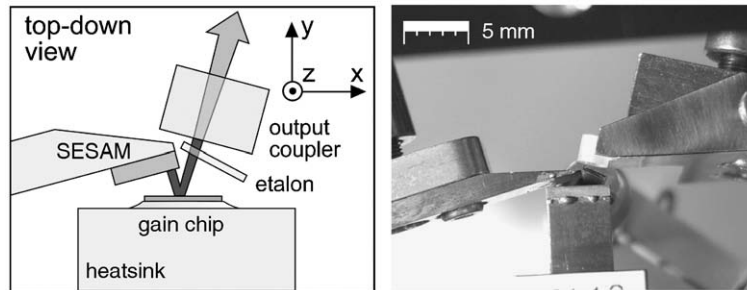


Fig. 32. Left: a schematic of the cavity in a top-down view. Right: top-down photo of the cavity. The output coupler in this picture is the flat output coupler, which has a diameter of 2.5 mm. The miniature stepper motor which is used to turn the etalon is visible underneath the cavity.

which would deliver the pump beam at a 45° angle in the vertical plane, thereby eliminating the problem of obstruction of the pump beam by closely packed cavity components (output coupler, SESAM, etalon) in the horizontal plane (Fig. 31). The best 50 GHz modelocking results were obtained with a dynamically-stable cavity using a flat output coupler as shown in Fig. 32. The mode radii are larger than in the cavity using a curved output coupler, so that a better suppression of higher-order transverse modes is achieved. The mode radius in this cavity diverges as the dioptric power of the thermal lens approaches zero (this is one of the stability limits of the cavity). The laser will only start to lase at a pump power level where the thermal lens is strong enough to confine the mode to a radius comparable to the pump spot radius, since the fundamental mode will experience very high losses if it covers a significant amount of unpumped area in the periphery of the pump spot.

One of the major concerns was the thermal lens of the gain structure. In terms of their sensitivity to the thermal lens, the cavities for modelocking with traditional SESAMs at repetition rates between 1 and 10 GHz (“divergent-beam cavities”) are fundamentally different from the ones that are used for modelocking with QD-SESAMs with a mode area ratio of 1:1 (“collimated-beam cavities”). While the divergent-beam cavities use a strongly curved output coupler with a radius of curvature (ROC) approximately equal to the cavity length, the collimated-beam cavities use only a very weakly curved output coupler with a radius of curvature much larger than the cavity length (e.g. $ROC = 200$ mm for a cavity length of 3 mm). In a divergent-beam cavity, the focusing effect of the output coupler is much stronger than that of the thermal lens. The thermal lens then only has a perturbative influence which will modify the mode radius and introduce phase distortions due to its aberrations. In a collimated-beam cavity, the focusing effect of the thermal lens can be equally strong as, or even stronger than that of the output coupler.

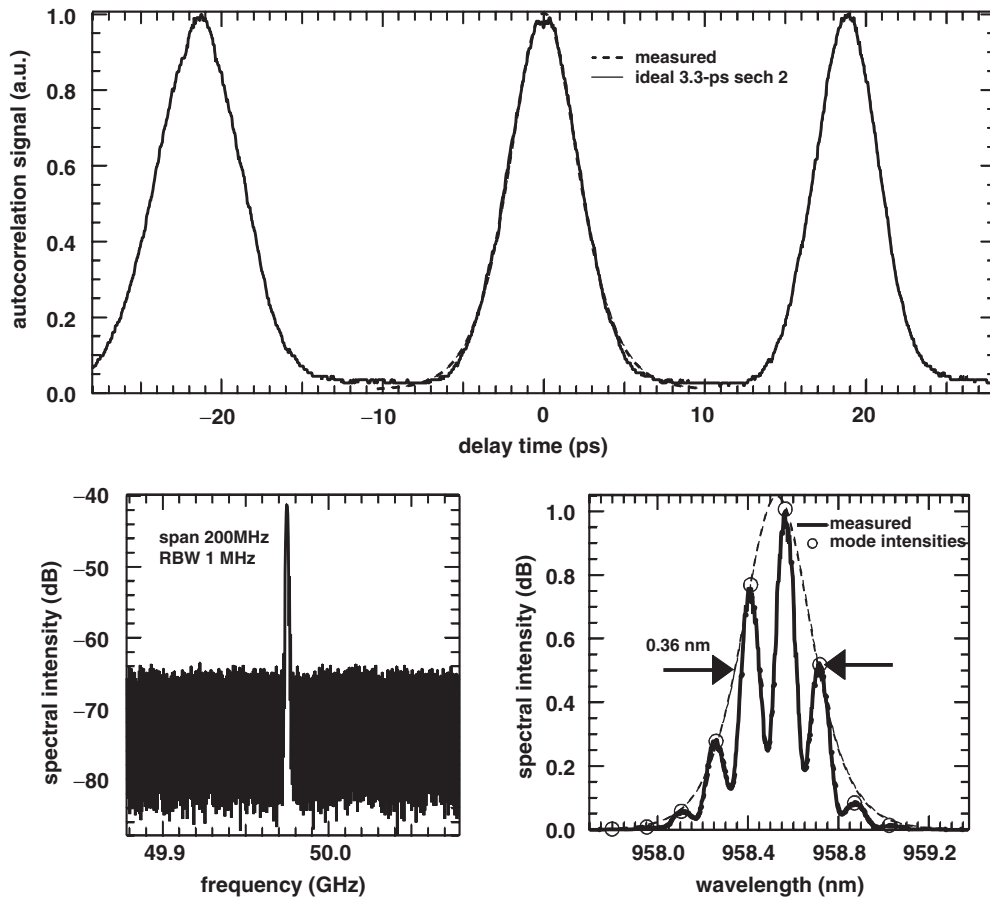


Fig. 33. Modelocking results of laser cavity shown in Figs. 21 and 22 at 50 GHz: 102 mW average output power. Results obtained using the VECSEL gain structure (Fig. 21(a)) and the QD-SESAM. Top: autocorrelation of the pulse train. Bottom left: RF spectrum of the fast-photodiode signal. Bottom right: optical spectrum. The optical bandwidth is given by the FWHM of an ideal sech^2 -envelope which was fitted to the intensities of the individual longitudinal modes.

The best modelocked result with 102 mW of average output power is shown in Fig. 33 using a flat output coupler [14]. The pump power was 3.7 W. The output beam was linearly polarized in the horizontal direction. The gain-structure heatsink temperature was 5 °C. A 25- μm uncoated fused-silica etalon was used to tune the wavelength. The time-bandwidth product of the pulses is 0.39. The mode size on gain and absorber was approximately 62 μm , the resulting intracavity pulse fluence was approximately 1.1 $\mu\text{J}/\text{cm}^2$.

6.3. Modelocking results in the femtosecond regime

A key challenge for the development of modelocked VECSELs is to generate transform-limited pulses in the femtosecond regime, making use of a significant fraction of the fairly broad (> 20 nm) intrinsic bandwidth of the quantum well gain medium. Most of the SESAM-modelocked VECSELs reported to date, however, operate in the few-ps regime, with optical pulse bandwidths of ~ 1 nm or less. These devices operate in the slow saturable absorber regime of modelocking, assisted by the quasi-soliton pulse shaping mechanism [219]. Compared to typical Kerr lens or soliton-modelocked vibronic solid state lasers, the pulse forming mechanism is weaker and the gain bandwidth curvature is stronger. Thus spectral condensation in the modelocking build-up period limits the bandwidth that the pulses reach in a steady state to the low values typically observed.

A sub-picosecond modelocked VECSEL was realized for the first time by Garnache et al. [225] using a specially-designed SESAM operating in the optical Stark effect SAM regime described in Section 3.4. The SESAM was designed

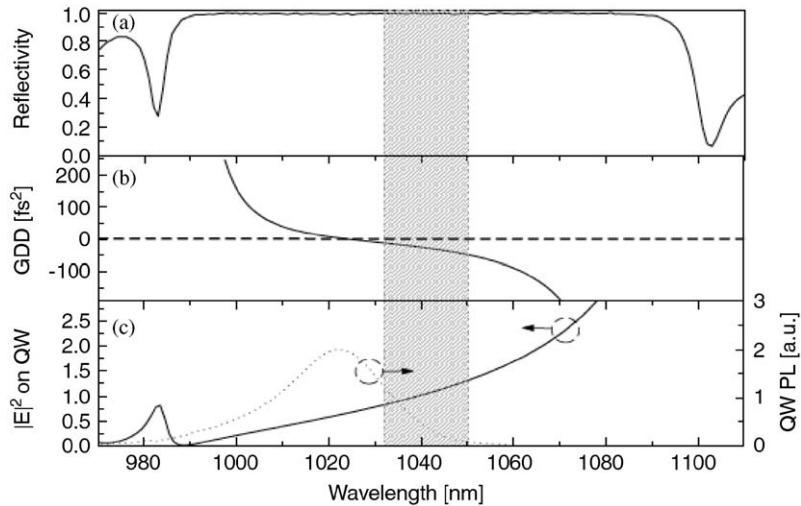


Fig. 34. Spectral characteristics of optical Stark effect SESAM: measured reflectivity spectrum (Fig. 34(a)); calculated GDD (Fig. 34(b)), and calculated longitudinal confinement factor spectrum (Fig. 34(c)) with measured quantum well photoluminescence spectrum (dotted curve). The hatched area defines the spectral window in which the laser is designed to operate.

for use over a 20-nm operating wavelength range about a centre wavelength of 1040 nm. It contained a single 8-nm $\text{In}_{0.23}\text{Ga}_{0.77}\text{As}/\text{GaAs}$ quantum well, with a room-temperature excitonic absorption peak at 1025 nm; thus the detuning of the intracavity photons to the low-energy side of the exciton resonance was designed to vary from $\sim 4\text{--}20$ meV. The quantum well was positioned 2 nm below the air surface of the structure, so that carriers generated by absorption in the wing of the resonance were quenched by surface state recombination on a short timescale; the carrier lifetime was measured to be ~ 21 ps using a streak camera. The advantage of using surface-state recombination here rather than low-temperature growth or ion-implantation to speed absorption recovery was that the entire structure could be grown by standard MOVPE with a correspondingly low insertion loss, estimated to be $< 0.1\%$. The spectral characteristics of the optical Stark SESAM are shown in Fig. 34, in which the shaded area identifies the spectral range in which the VECSEL is constrained to operate. The thickness of the GaAs layer between the air surface and the Bragg reflector was chosen to be $0.68 \times \lambda/4$. Two design considerations determined this choice: firstly the VECSEL operated just to the long wavelength side of the SESAM cavity antiresonance, where the GDD was small and negative (Fig. 34(b)), and secondly the value of E^2 at the well position (Fig. 34(c)) was adjusted in this way to give the desired value of saturable absorption loss, of $\sim 0.75\%$.

The SESAM was used in a Z-cavity in combination with a gain structure containing 6 InGaAs/GaAs quantum wells, pumped at normal incidence by 830-nm radiation from a 1-W fiber-coupled diode laser focused into a 60- μm radius spot on the gain chip. The waist on the SESAM has a spot-size of $\sim 18 \mu\text{m}$, with an area $\sim 13\times$ smaller than that of the waist on the gain chip. The cavity had a fundamental repetition rate of 1.24 GHz.

The design of the gain chip, with a short, near-antiresonant active region, and a broad effective gain spectrum allowed smooth power/temperature tuning of the laser over the design wavelength range. No intracavity etalon was needed to control the operating wavelength. The variation of the longitudinal confinement factor and the GDD of this structure as a function of detuning from the design wavelength are shown in Fig. 35.

The modelocked pulses shortened from 1.15 ps to > 500 fs as the laser wavelength was tuned from 1035–1045 nm. Outside this spectral window the modelocking was either unstable, with the appearance of a pedestal in the pulse intensity autocorrelation traces, or generated long picosecond pulses. At a wavelength of 1040 nm, where the total GDD (SESAM + gain chip) was $\sim + 500 \text{ fs}^2$, the laser generated stable $1.05\times$ transform-limited pulses with a Gaussian profile, a bandwidth of 0.75 THz (2.4 nm) and a FWHM duration of 620 fs (Fig. 36). On further tuning of the laser to 1045 nm, the pulses acquired a sech^2 profile, and shortened to 477 fs (Fig. 37). They also acquired a chirp, with a bandwidth of 1.23 THz, corresponding to $1.85\times$ transform-limited. The round-trip GDD of the cavity at 1045 nm is $\sim + 250 \text{ fs}^2$, about half as large as that experienced by the 620-fs transform-limited pulses. It appears that although the

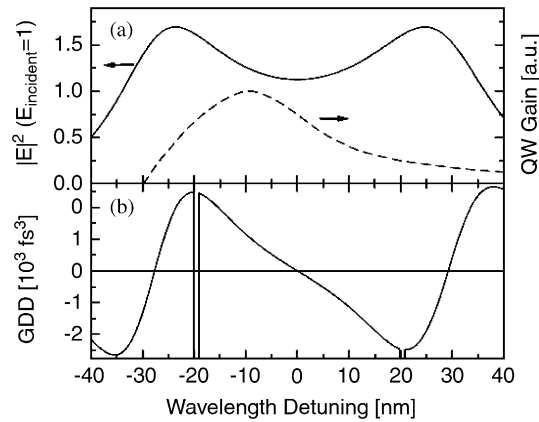


Fig. 35. Spectral characteristics of the femtosecond VECSEL gain structure: calculated longitudinal confinement factor spectrum (a) with typical gain profile (dotted curve); calculated GDD (b).

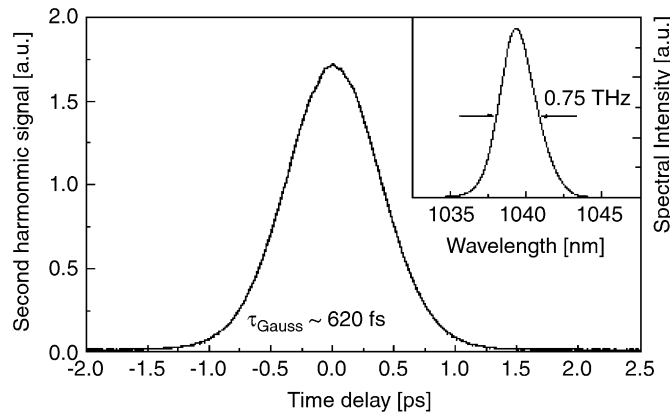


Fig. 36. Measured intensity autocorrelation of transform-limited sub-ps pulses in 1.24-GHz train with average power 40 mW. Dashed curve shows fitted Gaussian profile with FWHM duration 620 fs. Active structure temperatures are 277 K (gain chip) and 295 K (SESAM). Inset shows optical spectrum.

1045-nm wavelength gave the fastest pulse shaping from the SESAM, the positive round-trip GDD phase shift was not large enough at this point to balance the negative phase shift due to SPM.

Hoogland et al. [11] subsequently reported a near-transform-limited sub-500-fs pulse from an optical-Stark-modelocked VECSEL operating at a 10-GHz fundamental repetition rate. This laser used the same SESAM and gain structures as the 1.24 GHz laser reported previously: the lower intracavity pulse energy at the higher repetition rate generated less SPM, achieving a quasi-solitonic balance with the cavity GDD. The laser used a near-hemispherical 15-mm-long cavity, folded at the gain mirror, with cavity mode spot sizes on the gain and SESAM of 60 and 13.6 μm , respectively. Fig. 38 shows the intensity autocorrelation trace of a sech^2 pulse from this laser, FWHM duration 486 fs, operating at an average output power of 30.3 mW and a fundamental repetition frequency of 10.014 GHz. The optical spectrum, shown inset, is slightly modulated by the etalon effect in the substrate of the gain structure; however this appears to have negligible influence on the pulse formation. The optical spectrum width of 2.35 nm corresponds to a time-bandwidth product of 0.32. Fig. 39 shows the pulse characteristics when the output power is increased to 37 mW, with a peak power of $> 7 \text{ W}$. With a pulse duration of 490 fs, the pulse is no longer transform-limited, although its profile is still sech^2 .

It is clear from these results that the quasi-instantaneous SAM response arising from the optical Stark effect has taken modelocked VECSELs from the ps to the fs regime, given precise control of sample growth that allowed the balancing

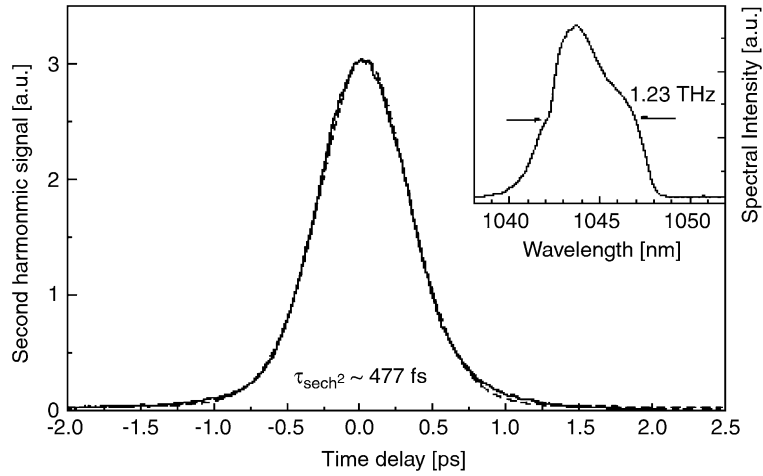


Fig. 37. Measured intensity autocorrelation of sub-500-fs pulses in 1.21-GHz train with average output power 100 mW. Dashed curve shows fitted hyperbolic secant profile with FWHM duration 477 fs. Active structure temperatures are 273 K (gain chip) and 299K (SESAM). Inset shows optical spectrum.

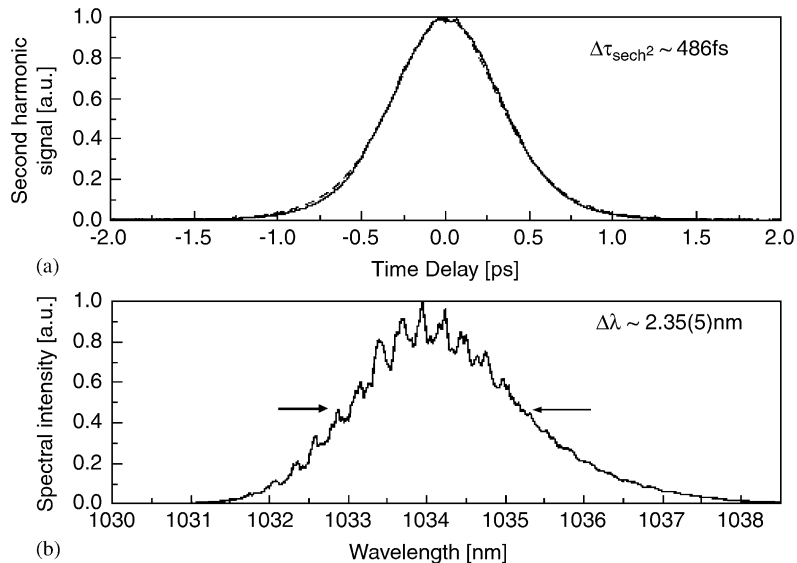


Fig. 38. Measured intensity autocorrelation of near-transform-limited pulses in 10-GHz train with average output power 30.3 mW (a). Dashed curve shows fitted hyperbolic secant profile with FWHM duration 486 fs. Measured optical spectrum of these pulses (b). The modulation of the spectrum is caused by scattering from the back surface of the gain structure substrate.

of dispersive and nonlinear phase shifts within the cavity. To achieve yet shorter pulses, it will be helpful to increase the modulation depth of the fast nonlinearity, so that steady-state modelocking is achieved in fewer roundtrips, with less filtering by the gain medium. The design of these cavities will also be facilitated by better understanding of the nonlinear phase shifts. Furthermore, we do not at present have a good model of optical Stark SAM, and it is therefore not yet clear how large a bandwidth for pulse formation this mechanism offers.

6.4. Modelocking results with electrically pumped VECSELs

The first electrically-pumped VCSEL to be modelocked was a GaAs/AlGaAs structure reported by Jiang et al. [228]. The device was operated quasi-cw at 830 nm in a liquid N₂ cryostat, with an external cavity such that the fundamental

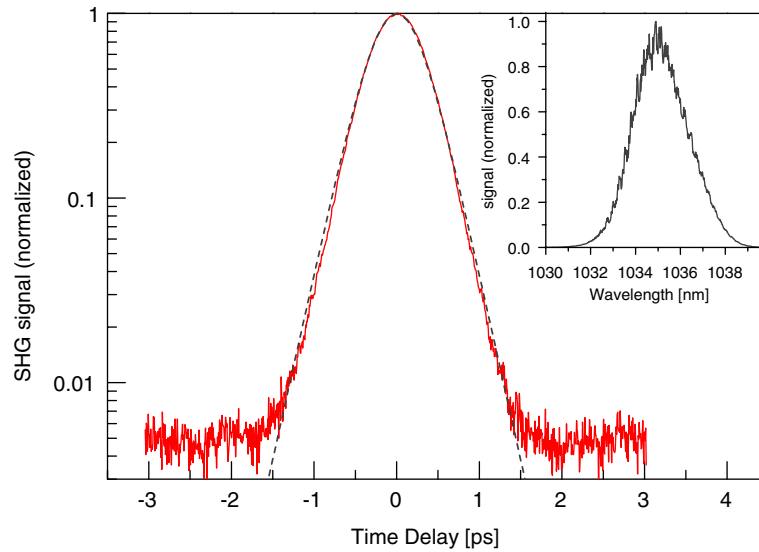


Fig. 39. Measured intensity autocorrelation of sub-500-fs pulses in 10-GHz train with average output power 37.8 mW and peak power 7.7 W. Dashed curve shows fitted hyperbolic secant profile with FWHM duration 490 fs. Inset shows optical spectrum with FWHM of 2.7 nm.

Table 6
Electrically pumped VECSELs: Passively modelocked using different SESAMs

Gain	λ_0 (nm)	τ_p ps	P_{av} (mW)	f_{rep} (GHz)	Ref.
GaAs/AlGaAs	830	81	4	0.960	[228]
InGaAs/GaAs	980	57	40	1.1	[229]
	980	14.8	≈ 10	15	[230,231]
	980	50	30	5.6	[15]
InGaAs/AlGaAs	975.8	22.6	0.72	0.297	[232]-GCSEL

λ_0 : center lasing wavelength. τ_p : measured pulse duration. P_{av} : average output power. f_{rep} : pulse repetition rate.

modelocking frequency was 960 MHz. Modelocking was by active modulation of the quasi-dc current bias; the measured pulse width of 81 ps contains a large instrumental contribution from timing jitter of the unsynchronised dc bias and modulation pulses (Table 6).

More recently Jasim et al. [229] have reported passively modelocked operation of the NECSEL structure described by McInerney et al. [4]. An LT-GaAs SESAM was incorporated into a Z-shaped external cavity with a repetition frequency of 1.1 GHz. The cavity modematched the 150- μm aperture of the NECSEL, and was focused to a spot size of $\sim 20\mu\text{m}$ on the SESAM. The laser exhibited stable modelocked operation, emitting 57-ps hyperbolic secant pulses with an average power of 40 mW. The high-finesse of the active region sub-cavity limited the modelocked bandwidth of this laser. These authors were, however, subsequently able to report 15-ps pulses generated from the same gain structure at repetition rates up to 15 GHz [230]. In this device, the SESAM layer structure was identical to that of the gain chip, only operated in reverse bias. A single microlens was used to couple the gain and absorber structures, and create a stable cavity between the two plane active mirrors. A subsequent investigation of the dynamics of the reverse-biased absorber structure revealed carrier sweep-out times of at least ~ 2 ps in this device [231].

The modelocking of semiconductor optical amplifiers (SOAs) in external cavities currently attracts considerable interest; it is outside the scope of this review, since the power-scaling scheme is fundamentally different, involving extreme pulse chirping, so that the amplifier is re-pumped during the passage of the pulse. Stretching and external recompression of these pulses is accomplished using chirped fiber Bragg gratings, with dispersion > 1600 ps/nm. A MOPA system of this type has recently been reported by the Delfyett group that achieved 590-fs pulses with 1.4 kW of peak power [233].

Closer in concept to the VECSELS described here is work that has been reported on external cavity modelocking of grating-coupled surface-emitting devices. 22-ps pulses at 297-MHz with 70 mW average power have been reported from an actively modelocked external-cavity grating-coupled surface-emitting InGaAs/AlGaAs separate confinement heterostructure—or GCSEL [232]. The holographic surface grating couples the gain chip into an external cavity formed by two lenses and a highly-reflecting mirror. The output beam is coupled through the substrate of the device, and exhibits roughly 4-fold asymmetry.

7. Conclusion and outlook

7.1. Final remarks

In recent years, optically-pumped semiconductor laser research has emerged as a hot current field, with the demonstration of quantum well lasers that emit many Watts, or even tens of Watts, in near-diffraction-limited beams. Much interest therefore currently focusses on the design, fabrication and thermal management of wafers for high power cw devices, which have enabled the development of a new class of visible laser; the intracavity-doubled VECSEL. With the extension of VECSELS to the red part of the spectrum, new practical sources in the UV can be envisaged. The spectral versatility of the VECSEL is likely to suit applications in areas ranging from biophotonics to atom optics to optoelectronics to gas spectroscopy. For example, the dynamic characteristics of the VECSEL are particularly well-suited to sensitive intra-cavity laser absorption spectroscopy (ICLAS) measurements (see e.g. [234]).

Passive modelocking of these lasers creates compact high-power ultrashort pulse sources that begin to rival their conventional solid state counterparts in simplicity and performance. Whereas early studies of these devices used gain chips modelled on half-VCSEL structures, and SESAM designs derived from solid state laser modelocking; better understanding of pulse-shaping mechanisms specific to VECSELS has enabled the development of more appropriate designs that exploit intrinsic quantum well properties more effectively. For those applications in communications and optoelectronics that demand high pulse repetition frequencies, the VECSEL can cover much of the microwave region that was hitherto the preserve of monolithic edge-emitting diodes, without the Q -switching instabilities that make solid state laser operation challenging in this regime, but with transform-limited pulse quality, and high power in a diffraction-limited beam. Recently, a 1054-nm modelocked VECSEL was used as the master oscillator for an ytterbium-doped fiber power amplifier system; an application to which the good stability and clean pulse characteristics of the VECSEL were well suited. The amplifier achieved an average output power of 160 W in a 1-GHz train of 5-ps pulses [235].

One challenge for the future is to exploit faster pulse-shaping nonlinearities in modelocked VECSELS that will allow the generation of shorter pulses. Passively modelocked VECSELS have been configured to generate the shortest transform-limited pulses emitted by any semiconductor laser to date: nevertheless, only a fraction of even the single-well gain bandwidth has so far been recruited for pulse generation. Another challenge is the extension of electrically-pumped devices as highly compact intermediate power sources. The electrically-pumped VECSEL gain chips described in the literature so far are optimised for narrow-band operation, especially as applied to intracavity doubling. There has to date been no corresponding development of injection-pumped gain chips optimised for short pulse generation. Finally, it is clear that work to date has hardly begun to exploit the possibilities for integrating distinct functionalities within a single laser wafer. The next section considers one promising potential development of this type.

7.2. Wafer scale integration

Scaling down VECSELS to the highest possible repetition rates naturally leads one to contemplate some form of monolithic structure in which gain and absorber are integrated into one single semiconductor layer sequence. Such a monolithic device would allow to reduce the cavity to a simple linear geometry requiring only an external output coupler at a distance from the chip which determines the desired repetition rate. Such a cavity could be designed in a fully monolithic geometry [236]. The basic requirement is a suitable absorber material which has a sufficiently low saturation fluence in order to fulfill Eq. (5.1) with equal mode sizes on gain and absorber. The recent development of low- $F_{\text{sat,a}}$ SESAMs based on a quantum-dot absorber material has made it realistic to move towards this goal along the scheme shown in Fig. 40 [13]. As we have explained above, reducing $F_{\text{sat,a}}$ will allow one to gradually move away from cavities that focus the mode very tightly on the absorber. With the successful demonstration of 1:1 modelocking

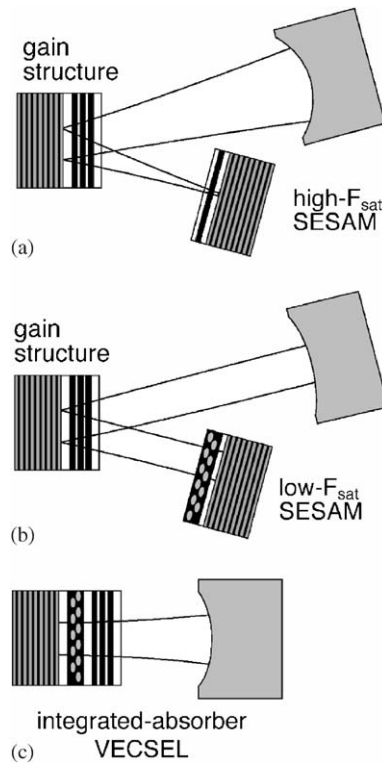


Fig. 40. Schematic illustration of the progression towards the integrated-absorber VECSEL: (a) folded cavity with high- $F_{\text{sat},a}$ SESAM requiring a tight focus on the absorber; (b) folded cavity with low- $F_{\text{sat},a}$ SESAM where mode sizes on gain and absorber can be equal; and (c) simple linear cavity with an integrated-absorber VECSEL.

(Fig. 40(b)) [13] which has the same mode sizes on absorber and gain, one can then take the final step and integrate the absorber into the gain structure in order to arrive at our desired configuration shown Fig. 40(c).

When designing such an integrated device, attention has to be paid to some consequences of having gain and absorber in the same semiconductor structure: both components act as heat sources, which makes good thermal management even more important. Also, the absorber needs to be protected from the pump light incident on the semiconductor chip. Therefore, the absorber should be located beneath the gain structure and separated by a pump-reflecting mirror. This intermediate mirror can simultaneously serve as a means to adjust the amount of optical resonance at the laser wavelength in the gain and absorber sections necessary for stable modelocking. Finally, as the ultimate state of integration, one could envisage a monolithic structure needing no external inputs except an electric power source. Such a device would involve integrating the output coupler onto the semiconductor chip [111] and pumping the gain electrically.

Acknowledgment

U. Keller acknowledges financial support from an Intel-sponsored research agreement and from ETH Zurich. A. Tropper acknowledges financial support from the Engineering and Physical Sciences Research Council, UK, and from the project Active Terahertz Imaging for Security in the EU Preparatory Action on the enhancement of the European industrial potential in the field of security research. Both of them also acknowledge support through the European Network of Excellence on Photonic Integrated Components and Circuits (ePIXnet) in the sixth research and technological development framework programme. This paper reviews work performed over many years during which many postdocs and Ph.D. students have contributed and have performed the actual experiments. At ETH we would like to acknowledge Dr. Heiko Unold, Dr. Rüdiger Paschotta, Dirk Lorensen, Alex Aschwanden, Reto Häring, Deran Maas, and Aude-Reine Bellancourt for their VECSEL work, Dr. Markus Haiml, Dr. Uwe Siegner, Rachel Grange for their SESAM work and Dr. Matthias Golling, Dr. Dirk Ebeling, Dr. Emilio Gini, Dr. Silke Schön, Valeria Liverini and

Andreas Rutz for their MBE and MOVPE growth. At University of Southampton we would like to acknowledge Dr. Sukhminder Dhanjal, Dr. Arnaud Garnache, Dr. Sjoerd Hoogland, Keith Wilcox and Hannah Foreman.

References

- [1] F. Kuznetsov, F. Hakimi, R. Sprague, A. Mooradian, *IEEE Photon Technol. Lett.* 9 (1997) 1063.
- [2] F. Kuznetsov, F. Hakimi, R. Sprague, A. Mooradian, *IEEE J. Sel. Top. Quantum Electron.* 5 (1999) 561.
- [3] J. Chilla, S. Butterworth, A. Zeitschel, J. Charles, A. Caprara, M. Reed, L. Spinelli, in *Photonics West 2004, Solid State Lasers XIII: Technology and Devices*, in Proc. SPIE 5332 (H. J. H. R. Scheps, ed.), 2004, p. 143.
- [4] J.G. McInerney, A. Mooradian, A. Lewis, A.V. Shchegrov, E.M. Strzelecka, D. Lee, J.P. Watson, M. Liebman, G.P. Carey, B.D. Cantos, W.R. Hitchens, D. Heald, *Electron. Lett.* 39 (2003) 523.
- [5] U. Keller, D.A.B. Miller, G.D. Boyd, T.H. Chiu, J.F. Ferguson, M.T. Asom, *Opt. Lett.* 17 (1992) 505.
- [6] U. Keller, *Progress in Optics* 46 (2004) 1.
- [7] U. Keller, K.J. Weingarten, F.X. Kärtner, D. Kopf, B. Braun, I.D. Jung, R. Fluck, C. Hönninger, N. Matuschek, J. Aus der Au, *IEEE J. Sel. Top. Quantum Electron.* 2 (1996) 435.
- [8] U. Keller, *Nature* 424 (2003) 831.
- [9] C. Hönninger, R. Paschotta, F. Morier-Genoud, M. Moser, U. Keller, *J. Opt. Soc. Am. B* 16 (1999) 46.
- [10] S. Hoogland, S. Dhanjal, A.C. Tropper, S.J. Roberts, R. Häring, R. Paschotta, U. Keller, *IEEE Photon Technol. Lett.* 12 (2000) 1135.
- [11] S. Hoogland, A. Garnache, I. Sagnes, J.S. Roberts, A.C. Tropper, *IEEE Photon Technol. Lett.* 17 (2005) 267.
- [12] A. Aschwanden, D. Lorenser, H.J. Unold, R. Paschotta, E. Gini, U. Keller, *Opt. Lett.* 30 (2005) 272.
- [13] D. Lorenser, H.J. Unold, D.J.H.C. Maas, A. Aschwanden, R. Grange, R. Paschotta, D. Ebling, E. Gini, U. Keller, *Appl. Phys. B* 79 (2004) 927.
- [14] D. Lorenser, D.J.H.C. Maas, H.J. Unold, A.-R. Bellancourt, B. Rudin, E. Gini, D. Ebling, U. Keller, *IEEE J. Quant. Electron.* in press (2006).
- [15] Q.A. Zhang, K. Jasim, A.V. Nurmikko, A. Mooradian, G. Carey, W. Ha, E. Ippen, *IEEE Photon Technol. Lett.* 16 (2004) 885.
- [16] H. Taga, M. Suzuki, Y. Namihira, *Electron. Lett.* 34 (1998) 2098.
- [17] L.F. Mollenauer, P.V. Mamyshev, *IEEE J. Quantum Electron.* 34 (1998) 2089.
- [18] S. Bigo, O. Leclerc, E. Desurvire, *IEEE J. Sel. Topics in Quantum Electron.* 3 (1997) 1208.
- [19] D.A.B. Miller, *Opt. Lett.* 14 (1989) 146.
- [20] M.J. Kobrinisky, B.A. Block, J.-F. Zheng, B.C. Barnett, E. Mohammed, M. Reshotko, F. Robertson, S. List, I. Young, K. Cadien, *Intel Technol. J.* 8 (02) (2004) ;
(Online) Available: http://www.intel.com/technology/itj/2004/volume08issue02/art05_on-chip/p01_abstract.htm.) 129.
- [21] K.J. Weingarten, M.J.W. Rodwell, D.M. Bloom, *IEEE J. Quantum Electron.* 24 (1988) 198.
- [22] J.A. Valdmanis, G.A. Mourou, C.W. Gabel, *Appl. Phys. Lett.* 41 (1982) 211.
- [23] T. Udem, R. Holzwarth, T.W. Hänsch, *Nature* 416 (2002) 233.
- [24] H.S. Margolis, C.S. Edwards, G.P. Barwood, P. Gill, in: F. X. Kärtner (Ed.), *Conference Proceedings, 15th Annual Meeting of the IEEE Lasers & Electro-Optics Society, 2002 IEEE/LEOS Annual Meeting*, vol. 1, Glasgow, Scotland, 2002, p. 229.
- [25] A. Hatziefremidis, D.N. Papadopoulos, D. Fraser, H. Avramopoulos, *Nucl. Instrum. Methods A* 431 (1999) 46.
- [26] K. Sato, *IEEE J. Lightwave Technol.* 20 (2002) 2035.
- [27] E. Yoshida, N. Shimizu, M. Nakazawa, *IEEE Photon Technol. Lett.* 11 (1999) 1587.
- [28] J. Leibrich, C. Wree, W. Rosenkranz, *IEEE Photon Technol. Lett.* 14 (2002) 155.
- [29] C. Xu, X. Liu, L.F. Mollenauer, X. Wei, *IEEE Photon Technol. Lett.* 15 (2003) 617.
- [30] G.J. Spühler, K.J. Weingarten, R. Grange, L. Krainer, M. Haiml, V. Liverini, M. Golling, S. Schon, U. Keller, *Appl. Phys. B* 81 (2005) 27.
- [31] L. Krainer, R. Paschotta, J. Aus der Au, C. Hönninger, U. Keller, M. Moser, D. Kopf, K.J. Weingarten, *Appl. Phys. B* 69 (1999) 245.
- [32] L. Krainer, R. Paschotta, M. Moser, U. Keller, *Electron. Lett.* 36 (2000) 1846.
- [33] L. Krainer, R. Paschotta, S. Lecomte, M. Moser, K.J. Weingarten, U. Keller, *IEEE J. Quantum Electron.* 38 (2002) 1331.
- [34] S. Lecomte, R. Paschotta, M. Golling, D. Ebling, U. Keller, *J. Opt. Soc. Am. B* 21 (2004) 844.
- [35] S. Lecomte, L. Krainer, R. Paschotta, M.J.P. Dymott, K.J. Weingarten, U. Keller, *Opt. Lett.* 27 (2002) 1714.
- [36] S. Lecomte, R. Paschotta, S. Pawlik, B. Schmidt, K. Furusawa, A. Malinowski, D.J. Richardson, U. Keller, *IEEE Photon Technol. Lett.* 17 (2005) 483.
- [37] B.C. Collings, K. Bergman, W.H. Knox, *Opt. Lett.* 22 (1997) 1098.
- [38] P. Laporta, S. Longhi, M. Marchesi, S. Taccheo, O. Svelto, *IEEE Photon Technol. Lett.* 7 (1995) 155.
- [39] A. Schlatter, S.C. Zeller, R. Grange, R. Paschotta, U. Keller, *J. Opt. Soc. Am. B* 21 (2004) 1469.
- [40] R. Grange, M. Haiml, R. Paschotta, G.J. Spuhler, L. Krainer, M. Golling, O. Ostinelli, U. Keller, *Appl. Phys. B* 80 (2005) 151.
- [41] G.J. Spühler, P.S. Golding, L. Krainer, I.J. Kilburn, P.A. Crosby, M. Brownell, K.J. Weingarten, R. Paschotta, M. Haiml, R. Grange, U. Keller, *Electron. Lett.* 39 (2003) 778.
- [42] S.C. Zeller, L. Krainer, G.J. Spühler, R. Paschotta, M. Golling, D. Ebling, K.J. Weingarten, U. Keller, *Electron. Lett.* 40 (2004) 875.
- [43] S.C. Zeller, R. Grange, V. Liverini, A. Rutz, S. Schön, M. Haiml, U. Keller, S. Pawlik, B. Schmidt, *Advanced Solid-State Photonics (ASSP '06)* (2006).
- [44] G.J. Spuhler, L. Krainer, V. Liverini, R. Grange, M. Haiml, S. Pawlik, B. Schmidt, S. Schon, U. Keller, *IEEE Photon Technol. Lett.* 17 (2005) 1319.
- [45] A. Schlatter, B. Rudin, S.C. Zeller, R. Paschotta, G.J. Spühler, L. Krainer, N. Haverkamp, H.R. Telle, U. Keller, *Opt. Lett.* 30 (2005) 1536.
- [46] A.J. Kemp, B. Stormont, B. Agate, C.T.A. Brown, U. Keller, W. Sibbett, *Electron. Lett.* 37 (2001) 1457.
- [47] T. Tomaru, *Opt. Lett.* 26 (2001) 1439.

- [48] T. Tomaru, *Opt. Commun.* 225 (2003) 163.
- [49] R. Mellish, S. Chernikov, P. French, J. Taylor, *Electron. Lett.* 34 (1998) 552.
- [50] L. Krainer, R. Paschotta, G.J. Spühler, M. Moser, U. Keller, *Electron. Lett.* 35 (1999) 1160.
- [51] L. Krainer, R. Paschotta, M. Moser, U. Keller, *Appl. Phys. Lett.* 77 (2000) 2104.
- [52] S. Lecomte, M. Kalisch, L. Krainer, G.J. Spühler, R. Paschotta, L. Krainer, M. Golling, D. Ebling, T. Ohgoh, T. Hayakawa, S. Pawlik, B. Schmidt, U. Keller, *IEEE J. Quantum Electron.* 41 (2005) 45.
- [53] J. Kong, D.Y. Tang, S.P. Ng, B. Zhao, L.J. Qin, X.L. Meng, *Appl. Phys. B* 79 (2004) 203.
- [54] L. Krainer, D. Nodop, G.J. Spühler, S. Lecomte, M. Golling, R. Paschotta, D. Ebling, T. Ohgoh, T. Hayakawa, K.J. Weingarten, U. Keller, *Opt. Lett.* 29 (2004) 2629.
- [55] L. Krainer, R. Paschotta, G.J. Spühler, I. Klimov, C.Y. Teisset, K.J. Weingarten, U. Keller, *Electron. Lett.* 38 (2002) 225.
- [56] S.C. Zeller, L. Krainer, G.J. Spühler, K.J. Weingarten, R. Paschotta, U. Keller, *Appl. Phys. B* 76 (2003) 1181.
- [57] C. Erny, G.J. Spühler, L. Krainer, R. Paschotta, K.J. Weingarten, U. Keller, *Electron. Lett.* 40 (2004) 877.
- [58] E.A. Avrutin, J.H. Marsh, E.L. Portnoi, *IEE Proc. Optoelectron.* 47 (2000) 251.
- [59] P.P. Vasilev, A.B. Sergeev, *Electron. Lett.* 25 (1989) 1049.
- [60] T. Shimizu, I. Ogura, H. Yokoyama, *Electron. Lett.* 33 (1997) 1868.
- [61] S. Arahira, Y. Matsui, Y. Ogawa, *IEEE J. Quantum Electron.* 32 (1996) 1211.
- [62] D.A. Yanson, M.W. Street, S.D. McDougall, I.G. Thayne, J.H. Marsh, E.A. Avrutin, *Appl. Phys. Lett.* 78 (2001) 3571.
- [63] K.R. Tamura, K. Sato, *Opt. Lett.* 27 (2002) 1268.
- [64] R. Scollo, H.J. Lobe, J.E. Holzman, E. Robin, H. Jackel, D. Erni, W. Vogt, E. Gini, *Opt. Lett.* 30 (2005) 2808.
- [65] T. Ishibashi, T. Furuta, H. Fushimi, S. Kodama, H. Ito, T. Nagatsuma, N. Shimizu, Y. Miyamoto, *IEICE Trans. Electron.* E83C (2000) 938.
- [66] E.U. Rafailov, M.A. Cataluna, W. Sibbett, N.D. Il'inskaya, Y.M. Zadiranov, A.E. Zhukov, V.M. Ustinov, D.A. Livshits, A.R. Kovsh, N.N. Ledentsov, *Appl. Phys. Lett.* 87 (2005) 081107.
- [67] J.E. Hastie, S. Calvez, M.D. Dawson, T. Leinonen, A. Laakso, J. Lytykainen, M. Pessa, *Opt. Express* 13 (2005) 77.
- [68] U. Keller, *Appl. Phys. B* 58 (1994) 347.
- [69] R. Fluck, G. Zhang, U. Keller, K.J. Weingarten, M. Moser, *Opt. Lett.* 21 (1996) 1378.
- [70] R. Fluck, B. Braun, E. Gini, H. Melchior, U. Keller, *Opt. Lett.* 22 (1997) 991.
- [71] R. Fluck, R. Häring, R. Paschotta, E. Gini, H. Melchior, U. Keller, *Appl. Phys. Lett.* 72 (1998) 3273.
- [72] R. Häring, R. Paschotta, R. Fluck, E. Gini, H. Melchior, U. Keller, *J. Opt. Soc. Am. B* 18 (2001) 1805.
- [73] S. Hoogland, B. Paldus, A. Garnache, K.J. Weingarten, R. Grange, M. Haiml, R. Paschotta, U. Keller, A.C. Tropper, *Electron. Lett.* 39 (2003) 846.
- [74] I. Sagnes, G.L. Roux, C. Meriadec, A. Mereuta, G. Saint-Girons, M. Bensoussan, *Electron. Lett.* 37 (2001) 500.
- [75] C. Symonds, I. Sagnes, A. Garnache, S. Hoogland, G. Saint-Girons, A.C. Tropper, J.L. Oudar, *Appl. Opt.* 42 (2003) 6678.
- [76] M.E. Kurdi, S. Bouchoule, A. Bousseksou, I. Sagnes, A. Plais, M. Strassner, C. Symonds, A. Garnache, J. Jaquet, *Electron. Lett.* 40 (2004) 671.
- [77] J.S. Harris Jr., *Semicond. Sci. Technol.* 17 (2002) 880.
- [78] H. Riechert, A. Ramakrishnan, G. Steinle, *Semicond. Sci. Technol.* 17 (2002) 892.
- [79] J.M. Hopkins, S.A. Smith, C.W. Jeon, H.D. Sun, D. Burns, S. Calvez, M.D. Dawson, T. Jouhti, M. Pessa, *Electron. Lett.* 40 (2004) 30.
- [80] S.A. Smith, J.M. Hopkins, J.E. Hastie, D. Burns, S. Calvez, M.D. Dawson, T. Jouhti, J. Kontinnen, M. Pessa, *Electron. Lett.* 40 (2004) 935.
- [81] A. Rutz, V. Liverini, D.J.A.C. Maas, B. Rudin, A. Bellancourt, S. Schön, U. Keller, *Electron. Lett.* 2006, in preparation.
- [82] M.A. Wistey, S.R. Bank, H.B. Yuen, L.L. Goddard, J.S. Harris, Jr., in: A.A. Sawchuk (Ed.), *Conference on Lasers and Electro Optics (CLEO)*, vol.1 16 21 May 2004 San Francisco, CA, USA, IEEE, Piscataway, NJ, USA, 2004, p. 3500.
- [83] H.D. Sun, G.J. Valentine, R. Macaluso, S. Calvez, D. Burns, M.D. Dawson, T. Jouhti, M. Pessa, *Opt. Lett.* 27 (2002) 2124.
- [84] V. Liverini, S. Schön, R. Grange, M. Haiml, S.C. Zeller, U. Keller, *Appl. Phys. Lett.* 84 (2004) 4002.
- [85] R. Grange, A. Rutz, V. Liverini, M. Haiml, S. Schön, U. Keller, *Appl. Phys. Lett.* 87 (2005) 132103.
- [86] S. Schön, A. Rutz, V. Liverini, R. Grange, M. Haiml, S.C. Zeller, U. Keller, *J. Cryst. Growth* 278 (2004) 239.
- [87] G.J. Spühler, L. Krainer, V. Liverini, S. Schön, R. Grange, M. Haiml, A. Schlatter, S. Pawlik, B. Schmidt, U. Keller, *Photon Technol. Lett.* 17 (2005).
- [88] O.G. Okhotnikov, T. Jouhti, J. Kontinen, S. Karirinne, M. Pessa, *Opt. Lett.* 28 (2003) 364.
- [89] A. Härkönen, T. Jouhti, N.V. Tkachenko, H. Lemmetyinen, B. Ryvkin, O.G. Okhotnikov, T. Sajavaara, J. Keinonen, *Appl. Phys. A* 77 (2003) 861.
- [90] A. Rutz, R. Grange, V. Liverini, M. Haiml, S. Schön, U. Keller, *Electron. Lett.* 41 (2005) 321.
- [91] F. Saadallah, N. Yacoubi, F. Genty, C. Alibert, *J. Appl. Phys.* 94 (2003) 5041.
- [92] O. Ostinelli, G. Almuneau, M. Ebnöther, E. Gini, M. Haiml, W. Bächtold, *Electron. Lett.* 40 (2004) 940.
- [93] S. Adachi, *J. Appl. Phys.* 61 (1987) 4869.
- [94] O. Ostinelli, M. Haiml, R. Grange, G. Almuneau, M. Ebnöther, E. Gini, E. Müller, U. Keller, W. Bächtold, *J. Cryst. Growth* 286 (2006) 247.
- [95] R. Grange, O. Ostinelli, M. Haiml, L. Krainer, G.J. Spühler, S. Schön, M. Ebnöther, E. Gini, U. Keller, *Electron. Lett.* 40 (2004) 1414.
- [96] R. Grange, S.C. Zeller, S. Schön, M. Haiml, O. Ostinelli, M. Ebnöther, E. Gini, U. Keller, *IEEE Photon Technol. Lett.* 18 (2006) 805.
- [97] A. Ouvrard, A. Garnache, L. Cerutti, F. Genty, D. Romanini, *IEEE Photon Technol. Lett.* 17 (2005) 2020.
- [98] J.E. Hastie, J.-M. Hopkins, S. Calvez, C.W. Jeon, D. Burns, R. Abram, E. Riis, A.I. Ferguson, M.D. Dawson, *IEEE Photon Technol. Lett.* 15 (2003) 894.
- [99] R. Häring, R. Paschotta, A. Aschwanden, E. Gini, F. Morier-Genoud, U. Keller, *IEEE J. Quantum Electron.* 38 (2002) 1268.
- [100] S. Lutgen, T. Albrecht, P. Brick, W. Reill, J. Luft, W. Späth, *Appl. Phys. Lett.* 82 (2003) 3620.

- [101] P.S. Zory, *Quantum Well Lasers*, Academic Press, Inc., San Diego, 1993.
- [102] L.A. Coldren, S.W. Corzine, *Diode Lasers and Photonics Integrated Circuits*, Wiley, New York, 1995.
- [103] C. Wilmsen, H. Temkin, L.A. Coldren, *Vertical-Cavity Surface-Emitting Lasers*, Cambridge University Press, Cambridge, 1999.
- [104] A.C. Tropper, S. Hoogland, *Quantum Electron.* 30 (2006) 1.
- [105] A.C. Tropper, H.D. Foreman, A. Garnache, K.G. Wilcox, S.H. Hoogland, *J. Phys. D: Appl. Phys.* 37 (2004) R75.
- [106] A. Garnache, A.A. Kachnov, F. Stoeckel, R. Houdre, *JOSA B* 17 (2000) 1589.
- [107] S.H. Park, J. Kim, H. Jeon, T. Sakong, S.N. Lee, S. Chae, Y. Park, C.H. Jeong, G.Y. Yeom, Y.H. Cho, *Appl. Phys. Lett.* 83 (2003) 2121.
- [108] M. Schmid, S. Benchabane, F. Torabi-Goudarzi, R. Abram, A.I. Ferguson, E. Riis, *Appl. Phys. Lett.* 84 (2004) 4860.
- [109] A. Garnache, C.C. Tropper, V.C. Thierry-Mieg, *CLEO '01 Technical Digest* (2001) p. 198.
- [110] W.J. Alford, T.D. Raymond, A.A. Allerman, *J. Opt. Soc. Am. B* 19 (2002) 663.
- [111] J.E. Hastie, J.-M. Hopkins, C.W. Jeon, S. Calvez, D. Burns, M.D. Dawson, R. Abram, E. Riis, A.I. Ferguson, W.J. Alford, T.D. Raymond, A.A. Allerman, *Electron. Lett.* 39 (2003) 1324.
- [112] L. Fan, J. Hader, M. Schillgalies, M. Fallahi, A.R. Zakharian, J.V. Moloney, R. Bedford, J.T. Murray, S.W. Koch, W. Stolz, *IEEE Photon Technol. Lett.* 17 (2005) 1764.
- [113] C. Symonds, I. Sagnes, J.-L. Oudar, S. Bouchoule, A. Garnache, J. Berggren, M. Strassner, *Opt. Commun.* 230 (2004) 419.
- [114] C. Symonds, J. Dion, I. Sagnes, M. Dainese, M. Strassner, L. Leroy, J.-L. Oudar, *Electron. Lett.* 40 (2004) 734.
- [115] H. Lindberg, A. Larsson, M. Strassner, *Opt. Lett.* 30 (2005) 2260.
- [116] H. Lindberg, M. Strassner, E. Gerster, A. Larsson, *Electron. Lett.* 40 (2004) 601.
- [117] H. Lindberg, M. Strassner, A. Larsson, *IEEE Photon Technol. Lett.* 17 (2005) 1363.
- [118] L. Cerutti, A. Garnache, F. Genty, A. Ouvrard, C. Alibert, *Electron. Lett.* 39 (2003) 290.
- [119] L. Cerutti, *J. Cryst. Growth* 268 (2004) 128.
- [120] J.E. Hastie, L.G. Morton, S. Calvez, M.D. Dawson, T. Leinonen, M. Pessa, G. Gibson, M.J. Padgett, *Opt. Express* 13 (2005) 7209.
- [121] M.A. Holm, D.B.A.I. Ferguson, M.D. Dawson, *IEEE Photon Technol. Lett.* 11 (1999) 1551.
- [122] M.A. Holm, P. Cusumano, D. Burns, A.I. Ferguson, M.D. Dawson, *Conference on Lasers and Electro-Optics, CLEO'99* (1999) paper CTuK63.
- [123] A. Giesen, H. Hügel, A. Voss, K. Wittig, U. Brauch, H. Opower, *Appl. Phys. B* 58 (1994) 365.
- [124] A. Garnache, S. Hoogland, A.C. Tropper, J.M. Gerard, V. Thierry-Mieg, J.S. Roberts, *CLEO/Europe-EQEC* (2001), Postdeadline Paper C.
- [125] H. Lindberg, M. Sadeghi, M. Westlund, S. Wang, A. Larsson, M. Strassner, S. Marcinkevicius, *Opt. Lett.* 30 (2005) 2793.
- [126] H. Lindberg, M. Strassner, J. Bengtsson, A. Larsson, *IEEE Photon Technol. Lett.* 16 (2004) 1233.
- [127] A.J. Kemp, G.J. Valentine, J.M. Hopkins, J.E. Hastie, S.A. Smith, S. Calvez, M.D. Dawson, D. Burns, *IEEE J. Quant. Electron.* 41 (2005) 148.
- [128] Z.L. Liao, *Appl. Phys. Lett.* 77 (2000) 651.
- [129] F.H. Peters, M.G. Peters, D.B. Young, J.W. Scott, B.J. Thibeault, S.W. Corzine, L.A. Coldren, *Electron. Lett.* 29 (1993) 200.
- [130] M. Miller, M. Grabherr, R. Jager, K.J. Ebeling, *IEEE Photon Technol. Lett.* 13 (2001) 173.
- [131] C. Yan, Y. Ning, L. Qin, Y. Liu, L. Zhao, Q. Wang, Z. Jin, Y. Sun, G. Tao, G. Chu, C. Wang, L. Wang, H. Jiang, *Electron. Lett.* 40 (2004) 872.
- [132] C. Yan, Y. Ning, L. Qin, D. Cui, Y. Liu, Y. Sun, Z. Jin, H. Li, G. Tao, C. Wang, L. Wang, H. Jiang, *IEEE Photon Technol. Lett.* 17 (2005) 1599.
- [133] E.U. Rafailov, W. Sibbett, A. Mooradian, J.G. McInerney, H. Karlsson, S. Wang, F. Laurell, *Opt. Lett.* 28 (2003) 2091.
- [134] M.W. Wiemer, R.I. Aldaz, D.A.B. Miller, J.S. Harris, *IEEE Photon Technol. Lett.* 17 (2005) 1366.
- [135] G.A. Keeler, D.K. Serkland, K.M. Geib, G.M. Peake, A. Mar, *IEEE Photon Technol. Lett.* 17 (2005) 522.
- [136] U. Keller, in: E. Garmire, A. Kost (Eds.), *Nonlinear Optics in Semiconductors*, vol. 59, Academic Press, Inc., Boston, 1999, p. 211.
- [137] J. Shah, *Ultrafast Spectroscopy of Semiconductors and Semiconductor Nanostructures*, Springer, Berlin, 1999.
- [138] R.J. Elliot, in: C.G. Kuper, G.D. Whitefield (Eds.), *Polarons and Excitons*, Plenum, New York, 1963.
- [139] E.O. Göbel, in: U. Rössler (Ed.), *Advances in Solid State Physics*, vol. 30, Friedrich Vieweg & Sohn, Braunschweig/Wiesbaden, 1990, p. 269.
- [140] L. Allen, J.H. Eberly, *Optical Resonance and Two-Level Atoms*, Dover, New York, 1975.
- [141] J.L. Oudar, D. Hulin, A. Migus, A. Antonetti, F. Alexandre, *Phys. Rev. Lett.* 55 (1985) 2074.
- [142] W.H. Knox, C. Hirlimann, D.A.B. Miller, J. Shah, D.S. Chemla, C.V. Shank, *Phys. Rev. Lett.* 56 (1986) 1191.
- [143] R.W. Schoenlein, W.Z. Lin, E.P. Ippen, J.G. Fujimoto, *Appl. Phys. Lett.* 51 (1987) 1442.
- [144] G.J. Spühler, R. Paschotta, R. Fluck, B. Braun, M. Moser, G. Zhang, E. Gini, U. Keller, *J. Opt. Soc. Am. B* 16 (1999) 376.
- [145] M. Haiml, R. Grange, U. Keller, *Appl. Phys. B* 79 (2004) 331.
- [146] M. Kondow, T. Kitatani, S. Nakatsuka, M. C. Larson, K. Nakahara, Y. Yazawa, M. Okai, K. Uomi, *IEEE Journal of Selected Topics in Quantum Electronics*. June 3 (1997) 719.
- [147] S.W. Osborne, P. Blood, P.M. Smowton, Y.C. Xin, A. Stintz, D. Huffaker, L.F. Lester, *J. Phys. Condens. Matter* 16 (2004) S3749.
- [148] R. Paschotta, U. Keller, *Appl. Phys. B* 73 (2001) 653.
- [149] R. Takahashi, Y. Kawamura, H. Iwamura, *Appl. Phys. Lett.* 68 (1996) 153.
- [150] H.S. Loka, P.W.E. Smith, *IEEE Photon Technol. Lett.* 10 (1998) 1733.
- [151] J.F. Whitaker, *Mater. Sci. Eng. B* 22 (1993) 61.
- [152] J.F. Ziegler, J.P. Biersack, U. Littmark, *The Stopping and Range of Ions in Solids*, Pergamon, New York, 1989.
- [153] F.W. Smith, A.R. Calawa, C.-L. Chen, M.J. Manfra, L.J. Mahoney, *IEEE Electron. Dev. Lett.* 9 (1988) 77.
- [154] X. Liu, A. Prasad, W.M. Chen, A. Kurpiewski, A. Stoschek, Z. Liliental-Weber, E.R. Weber, *Appl. Phys. Lett.* 65 (1994) 3002.
- [155] X. Liu, A. Prasad, J. Nishio, E.R. Weber, Z. Liliental-Weber, W. Walukiewicz, *Appl. Phys. Lett.* 67 (1995) 279.
- [156] M. Luysberg, H. Sohn, A. Prasad, P. Specht, Z. Liliental-Weber, E.R. Weber, J. Gebauer, R. Krause-Rehberg, *J. Appl. Phys.* 83 (1998) 561.
- [157] Z. Liliental-Weber, J. Ager, D. Look, X.W. Lin, X. Liu, J. Nishio, K. Nichols, W. Schaff, W. Swider, K. Wang, J. Wasburn, E.R. Weber, J. Whitaker, in: M. Godlewski (Ed.), *Eighth Conference on Semi-Insulating III–V Materials*, World Scientific, Singapore, 1994, p. 305.
- [158] M.R. Melloch, N. Otsuka, J.M. Woodall, A.C. Warren, J.L. Freeouf, *Appl. Phys. Lett.* 57 (1990) 1531.

- [159] G.L. Witt, R. Calawa, U. Mishra, E. Weber (Eds.), *Low temperature (LT) GaAs and related materials*, Mater. Res. Soc. Symposium Proceedings, vol. 241, Pittsburgh, 1992.
- [160] G.L. Witt, *Mater. Sci. Eng. B* 22 (1993) 9.
- [161] S. Gupta, M.Y. Frankel, J.A. Valdmanis, J.F. Whitaker, G.A. Mourou, F.W. Smith, A.R. Calawa, *Appl. Phys. Lett.* 59 (1991) 3276.
- [162] S. Gupta, J.F. Whitaker, G.A. Mourou, *IEEE J. Quantum Electron.* 28 (1992) 2464.
- [163] K.A. McIntosh, K.B. Nichols, S. Verghese, E.R. Brown, *Appl. Phys. Lett.* 70 (1997) 354.
- [164] M. Haiml, U. Siegner, F. Morier-Genoud, U. Keller, M. Luysberg, P. Specht, E.R. Weber, *Appl. Phys. Lett.* 74 (1999) 1269.
- [165] E.S. Harmon, M.R. Melloch, J.M. Woodall, D.D. Nolte, N. Otsuka, C.L. Chang, *Appl. Phys. Lett.* 63 (1993) 2248.
- [166] Y. Kostoulas, K.B. Ucer, G.W. Wicks, P.M. Fauchet, *Appl. Phys. Lett.* 67 (1995) 3756.
- [167] Y. Kostoulas, L.J. Waxer, I.A. Walmsley, G.W. Wicks, P.M. Fauchet, *Appl. Phys. Lett.* 66 (1995) 1821.
- [168] U. Siegner, R. Fluck, G. Zhang, U. Keller, *Appl. Phys. Lett.* 69 (1996) 2566.
- [169] A.J. Lochtefeld, M.R. Melloch, J.C.P. Chang, E.S. Harmon, *Appl. Phys. Lett.* 69 (1996) 1465.
- [170] G. Segsneider, T. Dekorsky, H. Kurz, R. Hey, K. Ploog, *Appl. Phys. Lett.* 71 (1997) 2779.
- [171] T.S. Sosnowski, T.B. Norris, H.H. Wang, P. Grenier, J.F. Whitaker, *Appl. Phys. Lett.* 70 (1997) 3245.
- [172] H.S. Loka, S.D. Benjamin, P.W.E. Smith, *IEEE J. Quantum Electron.* 34 (1998) 1426.
- [173] M.B. Johnson, T.C. McGill, N.G. Paulter, *Appl. Phys. Lett.* 54 (1989) 2424.
- [174] M. Lamsdorff, J. Kuhl, J. Rosenzweig, A. Axmann, J. Schneider, *Appl. Phys. Lett.* 58 (1991) 1881.
- [175] A. Krotkus, S. Marcinkevicius, J. Jasinski, M. Kaminska, H.H. Tan, C. Jagadish, *Appl. Phys. Lett.* 66 (1995) 3304.
- [176] F. Ganikhanov, G.-R. Lin, W.-C. Chen, C.-S. Chang, C.-L. Pan, *Appl. Phys. Lett.* 67 (1995) 3465.
- [177] C. Jagadish, H.H. Tan, A. Krotkus, S. Marcinkevicius, K.P. Korona, M. Kaminska, *Appl. Phys. Lett.* 68 (1996) 2225.
- [178] M.J. Lederer, B. Luther-Davies, H.H. Tan, C. Jagadish, M. Haiml, U. Siegner, U. Keller, *Appl. Phys. Lett.* 74 (1999) 1993.
- [179] H.H. Tan, C. Jagadish, M.J. Lederer, B. Luther-Davies, J. Zou, D.J.H. Cockayne, M. Haiml, U. Siegner, U. Keller, *Appl. Phys. Lett.* 75 (1999) 1437.
- [180] M. Haiml, U. Siegner, F. Morier-Genoud, U. Keller, M. Luysberg, R.C. Lutz, P. Specht, E.R. Weber, *Appl. Phys. Lett.* 74 (1999) 3134.
- [181] R. Grange, M. Haiml, R. Paschotta, G.J. Spühler, L. Krainer, O. Ostinelli, M. Golling, U. Keller, *Appl. Phys. B* 80 (2005) 151.
- [182] P. Silverberg, P. Omling, L. Samuelson, *Appl. Phys. Lett.* 52 (1988) 1689.
- [183] P. Omling, P. Silverberg, L. Samuelson, *Phys. Rev. B* 38 (1988) 3606.
- [184] P. Specht, S. Jeong, H. Sohn, M. Luysberg, A. Prasad, J. Gebauer, R. Krause-Rehberg, E.R. Weber, *Mater. Sci. Forum* 258–263 (1997) 951.
- [185] A. Mysyrowicz, D. Hulin, A. Antonetti, A. Migus, *Phys. Rev. Lett.* 56 (1986) 2748.
- [186] A. von Lehmen, D.S. Chemla, J.E. Zucker, J.P. Heritage, *Opt. Lett.* 11 (1986) 609.
- [187] Haug, Koch, *Quantum Theory of Optical and Electronic Properties of Semiconductors*, World Scientific, Singapore, 2004.
- [188] S. Tsuda, W.H. Knox, S.T. Cundiff, W.Y. Jan, J.E. Cunningham, *IEEE J. Sel. Top. Quantum Electron.* 2 (1996) 454.
- [189] J.M. Gérard, B. Sermage, B. Gayral, B. Legrand, E. Costard, V. Thierry-Mieg, *Phys. Rev. Lett.* 81 (1998) 1110.
- [190] H. Shoji, in: *Self-Assembled InGaAs/GaAs Quantum Dots*, vol. 60, Academic Press, San Diego, 1999, p. 241.
- [191] U. Keller, D. Kopf, US Patent No. 6'466'604 (priority date 19 May 1995).
- [192] U. Keller, W.H. Knox, H. Roskos, *Opt. Lett.* 15 (1990) 1377.
- [193] U. Keller, T.K. Woodward, D.L. Sivco, A.Y. Cho, *Opt. Lett.* 16 (1991) 390.
- [194] H.A. Haus, U. Keller, W.H. Knox, *J. Opt. Soc. Am. B* 8 (1991) 1252.
- [195] H.A. Haus, *IEEE J. Quant. Electron.* 12 (1976) 169.
- [196] A.J.D. Maria, D.A. Stetser, H. Heynau, *Appl. Phys. Lett.* 8 (1966) 174.
- [197] L.R. Brovelli, U. Keller, T.H. Chiu, *J. Opt. Soc. Am. B* 12 (1995) 311.
- [198] I.D. Jung, L.R. Brovelli, M. Kamp, U. Keller, M. Moser, *Opt. Lett.* 20 (1995) 1559.
- [199] L.R. Brovelli, I.D. Jung, D. Kopf, M. Kamp, M. Moser, F.X. Kärtner, U. Keller, *Electron. Lett.* 31 (1995) 287.
- [200] S. Tsuda, W.H. Knox, E.A.d. Souza, W.Y. Jan, J.E. Cunningham, *Opt. Lett.* 20 (1995) 1406.
- [201] R. Fluck, I.D. Jung, G. Zhang, F.X. Kärtner, U. Keller, *Opt. Lett.* 21 (1996) 743.
- [202] I.D. Jung, F.X. Kärtner, N. Matuschek, D.H. Sutter, F. Morier-Genoud, Z. Shi, V. Scheuer, M. Tilsch, T. Tschudi, U. Keller, *Appl. Phys. B* (Special Issue on Ultrashort Pulse Generation) 65 (1997) 137.
- [203] S. Schön, M. Haiml, L. Gallmann, U. Keller, *Opt. Lett.* 27 (2002) 1845.
- [204] S. Schön, M. Haiml, U. Keller, *Appl. Phys. Lett.* 77 (2000) 782.
- [205] S.N. Tandon, J.T. Gopinath, H.M. Shen, G.S. Petrich, L.A. Kolodziejski, F.X. Kärtner, E.P. Ippen, *Opt. Lett.* 29 (2004) 2551.
- [206] K. J. Weingarten, G. J. Spühler, U. Keller, L. Krainer, vol. US Patent No. 6,53,296 B1, GigaTera AG, USA, 2003.
- [207] K. J. Weingarten, G. J. Spühler, U. Keller, S. Thomas, vol. US Patent No. 6,826,219 B2, GigaTera AG, USA, 2003.
- [208] B. Braun, F.X. Kärtner, U. Keller, J.-P. Meyn, G. Huber, *Opt. Lett.* 21 (1996) 405.
- [209] R.C. Sharp, D.E. Spock, N. Pan, J. Elliot, *Opt. Lett.* 21 (1996) 881.
- [210] G.J. Spühler, S. Reffert, M. Haiml, M. Moser, U. Keller, *Appl. Phys. Lett.* 78 (2001) 2733.
- [211] R. Paschotta, J. Aus der Au, G.J. Spühler, F. Morier-Genoud, R. Hövel, M. Moser, S. Erhard, M. Karszewski, A. Giesen, U. Keller, *Appl. Phys. B* 70 (2000) S25.
- [212] M. Haiml, A. Aschwanden, U. Keller, *IEEE J. Quant. Electron.* in preparation (2006).
- [213] H.A. Haus, *J. Appl. Phys.* 46 (1975) 3049.
- [214] H.A. Haus, J.G. Fujimoto, E.P. Ippen, *IEEE J. Quantum Electron.* 28 (1992) 2086.
- [215] F.X. Kärtner, U. Keller, *Opt. Lett.* 20 (1995) 16.
- [216] F.X. Kärtner, I.D. Jung, U. Keller, *IEEE J. Sel. Topics Quantum Electron.* 2 (1996) 540.

- [217] G.H.C. New, *Opt. Commun.* 6 (1972) 188.
- [218] G.H.C. New, *IEEE J. Quantum Electron.* 10 (1974) 115.
- [219] R. Paschotta, R. Häring, U. Keller, A. Garnache, S. Hoogland, A.C. Tropper, *Appl. Phys. B* 75 (2002) 445.
- [220] G.P. Agrawal, N.A. Olsson, *IEEE J. Quantum Electron.* 25 (1989) 2297.
- [221] C.H. Henry, *IEEE J. Quantum Electron.* 18 (1982) 259.
- [222] O. Casel, D. Woll, M.A. Tremont, H. Fuchs, R. Wallenstein, E. Gerster, P. Unger, M. Zorn, M. Weyers, *Appl. Phys. B* 81 (2005) 443.
- [223] K.G. Wilcox, H.D. Foreman, J.S. Roberts, A.C. Tropper, *Electron. Lett.* 42 (2006) 159.
- [224] R. Häring, R. Paschotta, E. Gini, F. Morier-Genoud, H. Melchior, D. Martin, U. Keller, *Electron. Lett.* 37 (2001) 766.
- [225] A. Garnache, S. Hoogland, A.C. Tropper, I. Sagnes, G. Saint-Girons, J.S. Roberts, *Appl. Phys. Lett.* 80 (2002) 3892.
- [226] A. Aschwanden, D. Lorensen, H.J. Unold, R. Paschotta, E. Gini, U. Keller, *Appl. Phys. Lett.* 86 (2005) 131102.
- [227] D. Lorensen, *Photon Technol. Lett.* (2006).
- [228] W. Jiang, M. Shimizu, R.P. Mirin, T.E. Reynolds, J.E. Bowers, *Opt. Lett.* 18 (1993) 1937.
- [229] K. Jasim, Q. Zhang, A.V. Nurmikko, A. Mooradian, G. Carey, W. Ha, E. Ippen, *Electron. Lett.* 39 (2003) 373.
- [230] K. Jasim, Q. Zhang, A.V. Nurmikko, E. Ippen, A. Mooradian, G. Carey, W. Ha, *Electron. Lett.* 40 (2004) 34.
- [231] Q. Zhang, K. Jasim, A.V. Nurmikko, E. Ippen, A. Mooradian, G. Carey, W. Ha, *IEEE Photon Technol. Lett.* 17 (2005) 525.
- [232] K. Kim, S. Lee, O. Smolski, J.P.J. Delfyett, *Opt. Lett.* 29 (2004) 1273.
- [233] K. Kim, S. Lee, P.J. Delfyett, *Opt. Express* 13 (2005) 4600.
- [234] N. Picqu, G. Guelachvili, A.A. Kachanov, *Opt. Lett.* 28 (2003) 313.
- [235] H.D. Foreman, K.G. Wilcox, A.C. Tropper, P. Dupriez, A. Malinowski, J.K. Sahu, J. Nilsson, D.J. Richardson, F. Morier-Genoud, U. Keller, J.S. Roberts, *ASSP* (2006).
- [236] R.I. Aldaz, M.W. Wiemer, D.A.B. Miller, J.S. Harris, *Opt. Express* 12 (2004) 3967.
- [237] S.C. Zeller, R. Grange, T. Südmeyer, K.J. Weingarten, U. Keller, *Electron. Lett.*, in preparation (2006).